Evaluation of high quality topographic data for geomorphological and flood impact studies in upland area: North York Moors, UK

Dong, Lu

Evaluation of high quality topographic data for geomorphological and flood impact studies in upland area: North York Moors, UK

by

Lu Dong

A thesis presented for the degree of

Master of Science

University of Durham

Department of Geography

November 2006

Abstract

A flash flood on 19th June 2005 caused more than one hundred landslides in the North-western North York Moors uplands, UK. This project aims to 1) assess digital elevation models (DEMs) in terms of statistical terrain analysis and 2) explore the sensitivity of a 2D FLOWMAP model response to DEMs input data. A variety of topographic data were acquired, generated and processed. These included high resolution aerial photographs, Ordnance Survey (OS) DEMs, topographic maps, InSAR DEMs, LiDAR data and ground survey data. These DEMs of different horizontal and vertical resolutions were analysed through key topographic parameters calculated using three different software packages. Key topographic attributes such as slope, aspect, profile curvature and the Topographic Wetness Index (TWI) were studied. Results demonstrate that DEMs from different sources or at different resolutions provide different representations of topographic parameters especially in areas where large topographic changes take place. Algorithms used in different packages also had an effect. Degradation in the representation of topographic information is larger between 10 m and 50 m DEMs than between 5 m and 10 m DEMs. Finer resolution and smaller filter size have the same type of impact on slope and aspect. In addition, DEMs at finer horizontal resolutions have smaller minimum profile curvatures and larger maximum values and standard deviations in profile curvature. The TWI is more sensitive to the horizontal resolution than DEM data source and finer DEMs calculate smaller minimum and mean TWI and larger maximum TWI and standard deviations. Modelled hydrological responses are sensitive to both DEM resolution and its data source. Model showed different results when using 5 m LiDAR DEM and 5 m InSAR DEM of the same area, which meant DEM source had impacts on modelling These differences reduced with a larger magnitude flooding. Producing a better representative surface model from the LiDAR data has much larger impact on model response than adjusting a constant roughness coefficient.

Key words: topographic representation, terrain analysis, DEM assessment, InSAR, LiDAR, FLOWMAP.

Table of Contents

Page

Abstract I
Table of Contents II
List of Figures V
List of Tables VIII
Declaration X
State of Copyright XI
Acknowledgements XII

1. Introduction 1
   1.1. Flood Risk 1
   1.2. Flood Event in the North York Moors, UK 3
   1.3. Current Research 5
   1.4. Theoretical Frameworks 6
   1.5. Aims and Objectives 8

2. Datasets and Methodology 10
   2.1. Aims and Structure 10
   2.2. General Datasets for Topography-based Geomorphological and Hydrological Research 10
      2.2.1. Topographic Data 10
      2.2.2. Imagery 11
      2.2.3. Field Data 12
   2.3. Available Datasets in this Study 12
   2.4. Study Areas 15
   2.5. Topographic Data 16
      2.5.1. The Ordnance Survey Maps 16
      2.5.2. The OS MasterMap™ 19
      2.5.3. DEMs 23
   2.6. Imagery 36
      2.6.1. ATM 36
      2.6.2. Aerial Photographs 38
      2.6.3. Pre-event Aerial Photographs 43
   2.7. Field Data 44
      2.7.1. Ground Control Points 44
      2.7.2. Transects 46
      2.7.3. GPS RTK 47
      2.7.4. Laser Scanning 48
   2.8. Other Datasets 50
   2.9. Summary 52

3. DEM Assessment 54
   3.1. Introduction 54
   3.2. Research Issues 54
   3.3. Topographic Parameters 56

3.3.1. Surface Definition 56
3.3.1.1. D8 (Deterministic Eight-Node) Method 56
3.3.1.2. Evans Full Quadratic Surface 57
3.3.1.3. Partial Quadric 59
3.3.2. Software Packages 60
3.3.3. Slope 61
3.3.4. Aspect 62
3.3.5. Profile Curvature 63
3.3.6. Plan Curvature 64
3.3.7. Topographic Wetness Index 64
3.4. Calculation 66
3.5. Results 68
3.5.1. DEMs 68
3.5.1.1. Elevation Distribution 68
3.5.1.2. Cumulative Probability 76
3.5.1.3. Histograms 78
3.5.2. Slope 80
3.5.2.1. Statistical Analysis 80
3.5.2.2. Slope Difference Comparison 85
3.5.2.3. Algorithm Comparison 92
3.5.3. Aspect 94
3.5.3.1. Statistical Analysis 94
3.5.3.2. Aspect Visualisation 100
3.5.3.3. Aspect Difference Comparison 104
3.5.3.4. Algorithm Comparison 104
3.5.4. Profile Curvature 108
3.5.4.1. Statistical Analysis 109
3.5.4.2. Profile Curvature Difference Comparison 113
3.5.4.3. Algorithm Comparison 119
3.5.5. Topographic Wetness Index 122
3.5.5.1. Statistical Analysis 122
3.5.5.2. TWI Visualisation 131
3.5.5.3. TWI Difference Comparison 131
3.6. Applications 133
3.7. Discussion 135
DEM 135
3.7.1.1. Resolution 135
3.7.1.2. Data Source 136
Slope 137
3.7.2.1. Resolution 137
3.7.2.2. Data Source 139
3.7.2.3. Algorithm 139
3.7.3. Aspect 140
3.7.3.1. Resolution 140
3.7.3.2. Data Source 141
3.7.3.3. Algorithm 141
3.7.4. Profile Curvature 141
3.7.5. Topographic Wetness Index 142
3.8. Summary and Conclusion 143

4. Flood Inundation Modelling 146
4.1. Introduction 146

4.2. Research Issues 146
4.3. Topographic Data Comparison for Flood Inundation Modelling 148
4.3.1. Model Description 148
4.4. Model Operation 154
4.4.1. Model Set-up 154
4.4.1.1. Model Operation Environment 154
4.4.1.2. Data Requirements 154
4.4.1.3. Input Data 155
4.4.2. Model Results 163
4.4.2.1. Data Source/Resolution Impact 164
4.4.2.2. Filter Algorithm and Manning's n Effect 169
4.4.2.3. Inundation Visualisation 171
4.4.3. Model Validation 173
4.5. Summary and Conclusions 175

5. Discussion, Summary and Conclusion 178
5.1. Discussion 178
5.1.1. DEM Quality Assessment 178
5.1.2. Algorithms for Topographic Attribute Calculation 179
5.1.3. DEM Data Source 180
5.1.3.1. Ordnance Survey DEMs 180
5.1.3.2. Photogrammetrically Derived DEMs 180
5.1.3.3. InSAR DEMs 181
5.1.3.4. LiDAR DEMs 181
5.1.4. DEM Resolution 184
5.1.5. Flood Modelling 184
5.1.6. Other Issues 186
5.2. Summary and Conclusions 186
5.2.1. Summary 186
5.2.2. Core Conclusions 188

References 190

List of Figures

Page

Figure 1.1 the Environment Agency flood zones map (http://www.environment-agency.gov.uk/commondata/acrobat/floodmapeng_1368736.pdf) combined with the Helmsley area in map of England and Wales 2
Figure 1.2 Two photos taken by Dr. Jeff Warburton on 21st June 2005 in the flooding area 4
Figure 1.3 EA model result of flood inundation area of the River Rye 5
Figure 2.1 Study area draft 16
Figure 2.2 British National Grid Reference System grid key (from the OS website) 17
Figure 2.3 An OS digital topographic map at 1:10 000 scale of the Head House area 19
Figure 2.4 the OS MasterMap™ of the model test area 22
Figure 2.5 Optech ALTM 3033 (http://arsf.nerc.ac.uk/instruments/altm.asp) 26
Figure 2.6 ARSF Dornier 228-101 Research Aircraft (http://arsf.nerc.ac.uk) 28
Figure 2.7 LiDAR operation principle illustration 29
Figure 2.8 DEMs of the Head House area 31
Figure 2.9 DEMs of the whole study area 32
Figure 2.10 an processed ATM image 37
Figure 2.11 Rolleiflex 6008 (NERC) 38
Figure 2.12 the aerial photo of the first over-flight (on 23/06/2005) of the Head House area 39
Figure 2.13 NERC Aircraft 40
Figure 2.14 ATM and digital camera 41
Figure 2.15 the 1:6 000 aerial photograph of the second over-flight (on 26th August 2005) of the Head House area 41
Figure 2.16 Zeiss RMK TOP 15 with a calibrated focal length of 153.971 mm 43
Figure 2.17 the pre-event aerial photographs of the Head House area 44
Figure 2.18 Setting a white plastic panel on a GCP and recording the location on a draft map 45
Figure 2.19 Dr. Jeff Warburton stands on a recognisable stone Using DGPS 46
Figure 2.20 Transect draft 47
Figure 2.21 Site photograph in the Head House peat slide channel on 27th September 2005 taken by Dr. Nikolaos Galiatstos 48
Figure 2.22 GPS base station on heather field taken on 27th September 2005 48
Figure 2.23 MDL LaserAce® Scanner 49
Figure 2.24 Gauging Station Map (from the EA website) 50
Figure 2.25 Stage data at the Broadway Foot station on the River Rye 51
Figure 2.26 Broadway Foot gauging station (from the EA website, 2006) 52
Figure 3.1 3×3 Subgrid for a gridded DEM (formatted from the figure in Wilson and Gallant, 2000) 56
Figure 3.2 3×3 Elevation sub-matrix (Zeverbergen and Thorne, 1987) 58
Figure 3.3 Multiple Flow Direction (Quinn et al., 1991) 65
Figure 3.4 Elevation Distribution of DEMs of the Head House Area 68
Figure 3.5 DEM elevation distribution comparison by different resolutions (1) 69
Figure 3.6 DEM elevation distribution comparison with different data source (1) ... 71

Figure 3.7 DEMs elevation distribution of the whole study area 73
Figure 3.8 DEM elevation distribution comparisons with different resolutions (2) .. 74
Figure 3.9 DEM elevation distribution comparison with different sources (2) 75
Figure 3.10 Cumulative probability in DEMs of the Head House Area (a) and the Whole study area (b) 77
Figure 3.11 DEM histograms of the Head House area 79
Figure 3.12 Slope distribution comparisons from different data sources of the whole study area 82
Figure 3.13 Cumulative probability of slope of the whole study area (a) and the Head House area (b) 84
Figure 3.14 Difference maps in slope from OS DEMs and SAR DEMs 86
Figure 3.15 Scatter plots of the slope calculated from 10 m OS DEM and 5 m, 10 m, and 50 m resolution SAR DEMs of the whole study area 87
Figure 3.16 Slope difference in outcrops of resistant strata 89
Figure 3.17 Slope differences from OS DEM and SAR DEMs 90
Figure 3.18 Kernel size impact on slope difference 91
Figure 3.19 Aspect distribution of DEMs of the whole study area 96
Figure 3.20 Cumulative probability of aspect of the Head House area (a) and the whole study area (b) 98
Figure 3.21Aspect image of the original 5 m LiDAR DEM 100
Figure 3.22 Aspect visulisation 101
Figure 3.23 Difference maps of aspect from OS DEMs and InSAR DEMs 102
Figure 3.24 Aspect 2D scatter plots 103
Figure 3.25 Aspect Differences in OS DEM and SAR DEM 105
Figure 3.26 Kernel size impact on aspect 106
Figure 3.27 Profile curvature distribution of 10 m resolution (a) and 50 m resolution (b) DEMs of the whole study area 110
Figure 3.28 112
Cumulative probability of profile curvature of the (a) whole study area and (b) the Head House area 112
Figure 3.29 114
Profile curvature maps of a 400 m ×400 m area 114
Figure 3.30 Profile curvature differences maps from the 10m resolution OS DEM and SAR DEMs 115
Figure 3.31 Same stream in different images (The left hand one is a colour aerial photograph at 1:15 000 scale, the middle image is a DEM profile curvature map from 10 m resolution OS DEM and the right hand one is from 5 m resolution SAR DEM profile curvature map) 117
Figure 3.32 Kernel size impact on profile curvature difference 118
Figure 3.33 123
TWI statistics of (a) the Head House area and (b) the model test area 123
Figure 3.34 125
Topographic Wetness Index distribution of 10 m DEMs and 50 m DEMs of the whole study area 125
Figure 3.35 127
Cumulative probability of the TWI in all DEMs of both study areas 127
Figure 3.36 128
TWI histogram and cumulative probability of the model test area 128
Figure 3.37 Topographic Wetness Index maps of the Head House area 130
Figure 3.38 132

TWI Differences Maps of the Head House Area 132
Figure 3.39 Elevation difference between the 5 m SAR DEM and the 5 m LiDAR DEM of the Head House area with the post-event 1:15 000 NERC aerial photographs as background. Differences were scaled to five categories and the colour of difference from -1 to 1 was set to transparent. 133
Figure 3.40 Slope difference maps from 5 m SAR DEM and 5 m LiDAR DEM (plot (a)) and 0.5 m NERC APs DEM and 5 m LiDAR DEM (plot (b)) of the Head House area with NERC 1:15 000 aerial photographs as background 134
Figure 4.1 Regular grid cells 150
Figure 4.2 Stage data at the Broadway Foot gauging station on the River Rye through time 158
Figure 4.3 Model test area DEMs and aerial photograph from left to right ((a) Filtered 5 m LiDAR DEM; (b) Unfiltered 5 m LiDAR DEM; (c) 10 m OS DEM; (d) 5 m SAR DEM; (e) 10 m SAR DEM; (f) Aerial photograph) 159
Figure 4.4 Elevation difference between the unfiltered LiDAR DEM and the filtered LiDAR DEM of the model test area 161
Figure 4.5 Filtered LiDAR measurements distribution in the model test area 162
Figure 4.6 5 m interval contour map derived from the filtered 5 m LiDAR DEM (a) and the unfiltered 5 m LiDAR DEM (b) in the flood model test area 163
Figure 4.7 Model results of flood inundation area from (a) the original stage data, (b) the artificial stage dataset 1, (c) the artificial stage dataset 2 and (d) the artificial stage dataset 3 165
Figure 4.8 Differences in flood inundation area simulation from both LiDAR DEMs 170
Figure 4.9 Inundation visualisation from the unfiltered 5 m LiDAR DEM based on the artificial stage dataset 1 172
Figure 4.10 Inundation visualisation from the filtered 5 m LiDAR DEM based on the artificial stage dataset 1 172
Figure 4.11 Inundation visualisation from the 10 m OS DEM based on the artificial stage dataset 1 172
Figure 4.12 Inundation visualisation from the 5 m SAR DEM based on the artificial stage dataset 1 172
Figure 4.13 Inundation visualisation from the 10 m SAR DEM based on the artificial stage dataset 1 172
Figure 4.14 Maximum inundation area derived from the NERC digital photographs and visualisations of model simulation for 10 hours using the original gauging station stage data with the unfiltered 5 m LiDAR DEM as the background 174

List of Tables

Page
Table 2.1Available datasets in this study 14
Table 2.2 Study areas summary including their locations in Britain Grid Coordinate System, sizes and purposes in this study 15
Table 2.3 Ordnance Survey topographic maps 18
Table 2.4 ALTM Paramaters 27
Table 2.5 Strips and data redundancy 29
Table 2.6 Statistics of DEMs of the Head House area 34
Table 2.7 Statistics of DEMs of the Whole Study Area 35
Table 2.8 ATM spectral range 36
Table 2.9 Parameters of ATM 1 37
Table 2.10 Parameters of ATM 2 38
Table 2.11 parameter of Rolleiflex 6008 39
Table 2.12 Parameters of Aerial Photographs 40
Table 3.1 5% Percentile and 95% Percentile of Elevations for the Head House Area (1 digit precision) 78
Table 3.2 5% Percentile and 95% Percentile of Elevations for the Whole Study Area (1 digit precision) 78
Table 3.3 Slope statistics in degrees 80
Table 3.4 Mean slope difference in degrees from SAR series DEMs 88
Table 3.5 Comparison of ENVI 4.1, Arc/GIS, and SAGA slope results in the Head House Area 93
Table 3.6 Aspect statistics in degrees 94
Table 3.7 5% Percentile and 95% Percentile of the Aspects in the Head House Area 99
Table 3.8 5% Percentile and 95% Percentile of the Aspects in the Whole Study Area 99
Table 3.9 Comparisons of the ENVI 4.1, Arc/GIS, and SAGA aspect result for the Head House area 107
Table 3.10 Profile curvature in radius per metre statistics for the whole study area 109
Table 3.11 Comparison profile curvature calculation result from ENVI 4.1, Arc/GIS and SAGA packages in the Head House area 120
Table 3.12 Summary of slope, aspect and profile curvature in the whole study area 121
Table 3.13 Summary of slope, aspect and profile curvature in the Head House area 121
Table 3.14 Topographic Wetness Index of the Head House area 122
Table 3.15 Topographic Wetness Index of the flood inundation model test area 123
Table 4.1 Stage data in 15 min spacing from 16.15 to 17.30 GMT on 19th June 2005 157
Table 4.2 Model test area statistics in British National Grid 160
Table 4.3 Maximum inundation area in square metres from four DEMs based in all flooding events 167

Table 4.4 Flood inundation area statistics from the original stage data and three artificial datasets (scenarios) 168
Table 4.5 Maximum inundation area summary from the NERC aerial photographs and the model simulations 175

Declaration

The work contained in this thesis is entirely that of the author. Material from the published works of others, which is referred to within this thesis, is credited to the author in question in the text. No part of this work has been submitted for any other degree in this or any other university.

The main body of text (excluding References) is approximately 36,000 words in length.

State of Copyright

Acknowledgements

Firstly I would like to thank to my both supervisors, Dr. Daniel Donoghue and Prof. Stuart Lane. I will not be able to finish the study and dissertation without your precious comments and suggestions. In addition, I want to give my special thanks to some colleagues in our department. I cannot imagine what is my dissertation would be without the help from Dr. Dapeng Yu with his flood model. I also thank to the care and kind assistance for my living here from Dr. Cheng Zong and Dapeng. I would appreciate the guidance in manual approach for flood inundation observation on aerial photographs and tracing flood map data from Dr. Jeff Warburton. I would also thank to Dr. Nikolaos Galiatsatos and David Milledge, who have helped me with remote sensing photogrammetry in particular and the Topographic Wetness Index calculating through the ArcGIS and SAGA, respectively. I would also thank to my three other Chinese colleagues, Miss Fengling Yu (Melissa), Miss Kit Ng (Angel) and Dr. Jingyi Li, my GIS lab partner PhD candidate Stephen Opoku-Duah for their reliance in the whole year. Last but not least, I would thank to my family in China who supports my expense for the one year study and friends living in lots of countries who always support me in difficulties, and all other unlisted friendly colleagues and staffs in our department and university who make my living here colourful and easier. I really enjoy the whole year study and life here in Durham, in the UK.

The whole year research taught me a lot from being independent in living to doing research scientifically. I can still remember on the third day after the arriving this country, I went with Danny, Jeff and Niko to the North York Moors National Park, the first time I gave a presentation in English in the Research Design course and also the happiness for the lively football World Cup in Germany. I cannot list all the happiness moments here and neither the tough periods but I would cherish the memory no matter what I am going to do or where I am going after graduation. I would like also share my thinking with you all that difficulties in doing research could happen in probably two cases: First, you have no idea to solve a problem. You may search online or in the library, or ask others for help and there will be someone

is able to help you; secondly, you have too many choices as possibilities. To explore the optimum solution and investigate the instinct reason would be helpful for the similar study in the future.

Thank you all very much indeed!

1. Introduction

1.1. Flood Risk

The flood is recognised as one of the most harmful natural disasters in term of the numbers of deaths that resulted from, all over the world. According to the United Nations, during the decade of 1986-1995, 367,000 people were killed by floods, which made up of 55% deaths in all natural disasters during that period of time (UNDHA, 1997). A Foresight Future Flooding report about flood risk in the UK was released on 22nd April 2004 by the Department of Trade and Industry (DTI) and the Environment Agency. The report stated that both populations in flood risk and damage costs from floods are likely increasing greatly in the future. This is particular the case for the upland area in the UK, where numerous floods with large impacts have happened in the recent decades (Johnson and Warburton, 2002). On the other hand, the Environment Agency used a new method named 'Risk Assessment for Strategic Planning' (RASP) for the National Flood Risk Assessment (NaFRA) to calculate flood risk areas in three categories, including the low risk (1:200 chance or less of flood) area, moderate risk (1:75 to 1:200 chance of flood) and the significant flood risk (1:75 chance or more of flood) area in the England and Wales for the insurance industry. In addition to the flood risk assessment, floodplain maps, flood defences maps and maps of areas benefiting from flood defences were produced from topographic data and information on flows for the citizens in flood risk areas by the Environment Agency. Since flooding is unpredictable, it is important to follow-up flood events and to assess their impacts through model predictions. In this case, quality of model prediction that how accurate flood inundation models match reality to produce a better flood map for the government and local citizens is highly concerned. A recent flood event in the North York Moors provided a good case for this study.

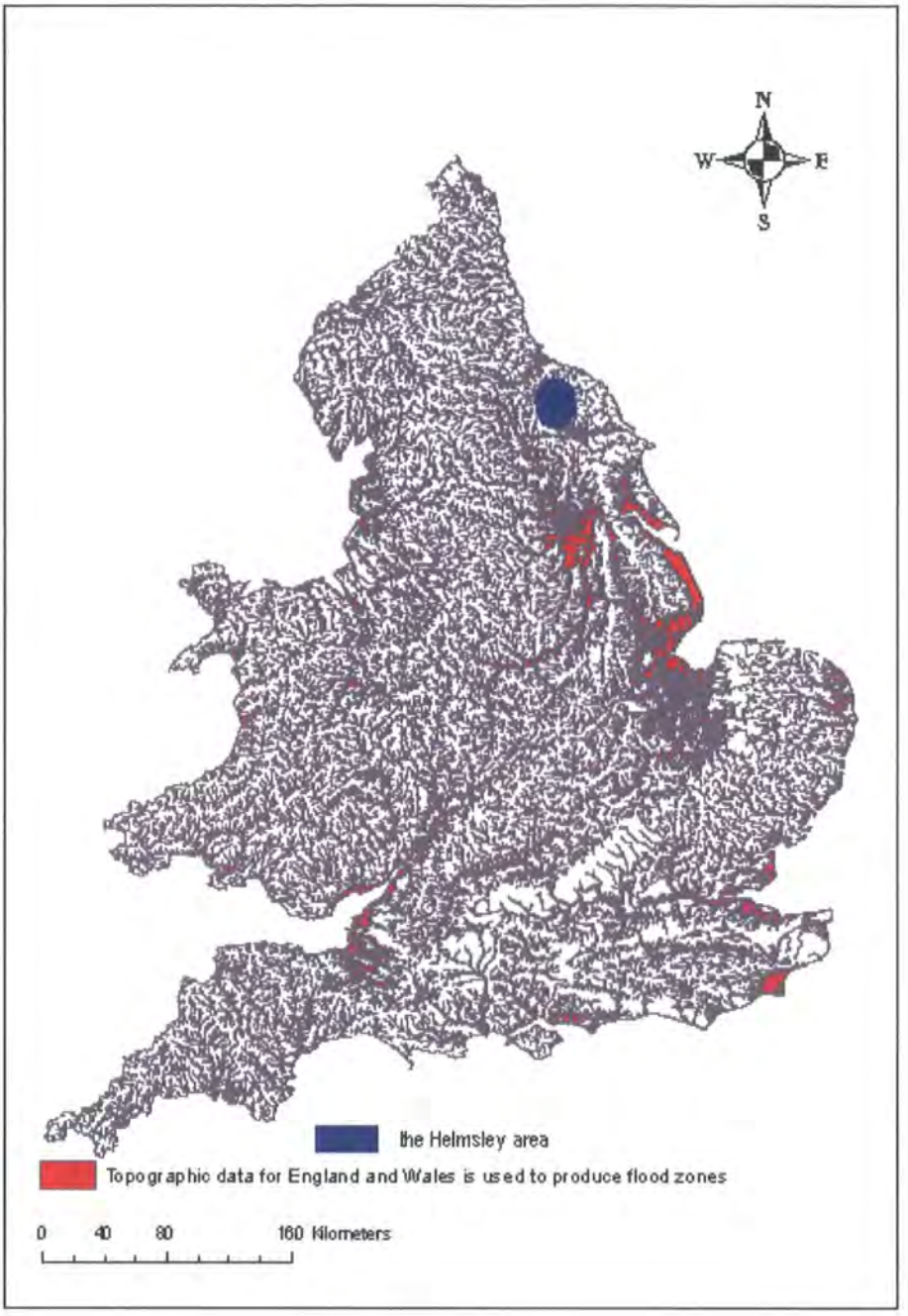

Figure 1.1 the Environment Agency flood zones map (http://www.environment-agency.gov.uk/commondata/acrobat/floodmapeng_1368736.pdf) combined with the Helmsley area in map of England and Wales

Fig. 1.1 illustrates the floodplain map of the England and Wales for a 1:100 chance of flood risk areas produced by the Environment Agency. The red areas on the map are the areas modelled, as an alternative source of topographic data, based on topographic data

from a digital terrain model (DTM) and/or Light Detection And Ranging (LiDAR) mapping. Other areas on the map contain detailed survey data.

1.2. Flood Event in the North York Moors, UK

An intense thunderstorm brought flash flood through the Helmsley area (Fig.1.1) in the North York Moors during the afternoon of 19th June 2005, when over 50 mm rainfall fell within a thirty-minute time period according to the Environment Agency. The flood triggered more than a hundred landslides/peat slides locally, which included a possibly the largest peat slide in the England in the Head House area. This hazard had a severe effect on roads, bridges (Fig. 1.2), channel slopes, land cover and more importantly the local livestock and citizens' lives in farms and especially in the town Helmsley (Fig. 1.3). Hence, the UK parliament held an urgent debate on the severe damage and demanding construction on 29th June 2005.

The North York Moors National Park is the major affected area. It comprises a high plateau bounded on the north by the Plain of Cleveland and on the south by the vales of Pickering and York. It was designated a National Park on 28th November 1952 and the area covers 1, 436 km^2 (c. 554 $mile^2$) with central coordinates of 1° 15' West, 54° 19' North, and altitude ranging from 30 m and 394 m, stretching from Saltburn in the north to Helmsley in the south, and from the Cleveland Hills in the west to the north-east coast of England. This National Park contains the largest continuous expanse of heather moor-land in the England.

(a) Damaged bridge in Hawnby

(b) Valley deposit in Upper Ryedale

Figure 1.2 Two photos taken by Dr. Jeff Warburton on 21st June 2005 in the flooding area

Fig. 1.2 shows severe flood damage and the flood effects on the bridges and river banks.

1.3. Current Research

The Environment Agency operated a flood inundation model based on topographic information from the Interferometric Synthetic Aperture Radar (InSAR) imagery. This information can be modified and refined using local flood history data and can be used to predict a different flood risk scenario/map on floodplains. It is important to assess the validity of such model and investigate the relationships between topographic representation and floods.

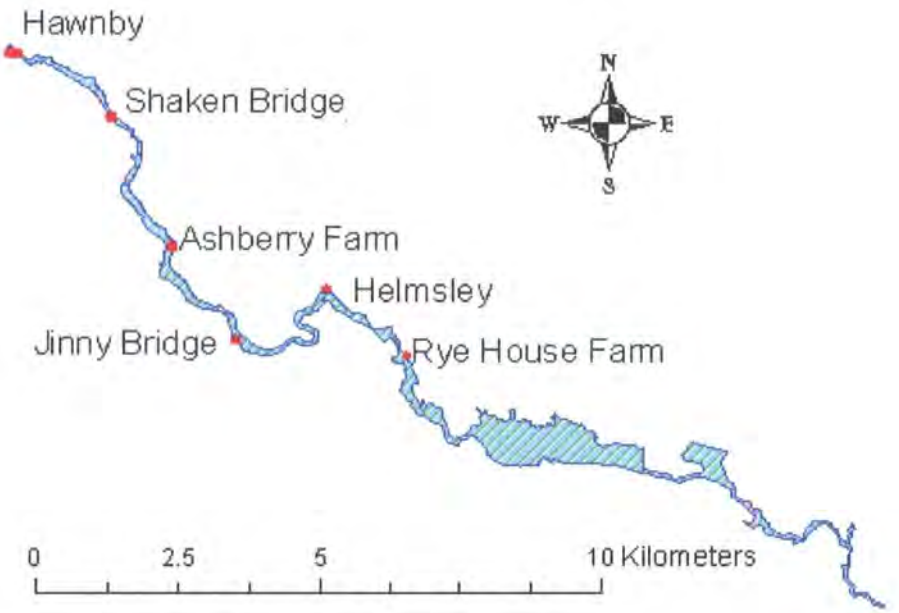

Figure 1.3 EA model result of flood inundation area of the River Rye

Fig. 1.3 shows the flood inundation (blue) area result from the EA model on the River Rye in the event of the flood on 19th June 2005.

1.4. Theoretical Frameworks

A flash flood is an extreme hydrological response to intense rainfall. The routing of the runoff is directly relative to the local topography (Lane et al., 1998) and poses a potential hazard to local residents and their properties. It is therefore important to assess the impact of this hazard and understand the flood risk in terms of hydrological response to the local topography.

Flood impact in a specific event, can be assessed in terms of its maximum inundation extent on the floodplain. A floodplain is renowned as an area which is dry in normal conditions and could be inundated during a flood event. To obtain the inundation extent, at least three approaches can be used: First, field measurements can be conducted in the inundation area. Second, inundation extent estimation can be taken on aerial photographs/radar imagery after event (Lane et al., 2003). Third, estimated maximum inundation extent through numerical modelling has become more frequently approach (e.g. Bates and De Roo, 2000; Bates, 2004; Bradbrook et al., 2004; Yu and Lane, 2006a and 2006b). The first approach is problematic with high cost, time consuming especially at a considerable catchment scale, though it can result in a high accuracy to a sub metre magnitude. The other two approaches would be more helpful for larger scale mapping.

Hydrological processes are sensitive to local topography (Yu and Lane, 2006a) and therefore topography can be used as a tool to better understand the processes. Based on this philosophy, different topography would lead to a different hydrological response in terms of the impact on the environment. Since various topographic data of either different sources or resolutions, represent different topography, it is necessary to investigate the effect of topographic data quality on hydrological processes through flood inundation extent calculation or measurement. Excluding the costly ground survey, topographic information is traditional obtained from topographic maps with contours. However such data have limitations. As there are no elevation values in the area between each pair of

contours, the majority area on the topographic map has to be digitised and interpolated from neighbouring pair of contours for local elevation. The interpolation introduces large uncertainty in elevation and hence the topography characteristic especially on large spacing contour maps. Currently highly developed remote sensing techniques have been introduced to this area, and so increasingly topographic data have become available for the study in a much larger area. These techniques involve aerial photogrammetry, RADAR and most recently the LiDAR (e.g. Bates etc., 2003; Bates etc., 2006; Cobby etc., 2003; Horritt etc., 2006). High resolution DEMs can be generated using these techniques in a much wider range of weather conditions (day and night for RADAR and LiDAR) for a much larger area especially for the areas people are not able to access, within a relatively short time in both acquisition and post-processing.

High resolution topographic data especially high resolution digital elevation models (DEMs) have been studied intensively for geomorphological and hydrological applications over the past twenty-five years or so and have been treated as an important topographic data source. For this study, therefore the topographic data assessment subjected to DEM assessment. The whole geomorphological and hydrological research experienced a great improvement in computational power either in hardware or software and a focus on wider range of topographic parameters and further, best representative topographic parameters for various applications. Beven and Kirkby (1979) first presented a hydrological forecasting model using the Topographic Wetness Index. Heerdegen and Beran (1982) described a technique of map analysis for source area (known as the localities responsible for quick-response flood runoff) from contour maps and emphasised that an 'uniform matrix of spot heights' would be a substitution for the contour maps in terms of accuracy. O'Callaghan and Mark (1984) and Mark (1984) showed that it took a long time to design a program and for a computer to detect drainage network from DEMs automatically. Burt and Butcher (1986) studied soil water condition on a 1-ha hill slope plot and found plan curvature the most successful indices for a range of soil condition. Jenson and Domingue (1988) developed a software tool to extract topographic structure from DEMs and found a generally close agreement comparing with manual results.

Jenson (1991) kept on developing a new computer program for delineating depressions, overland flow path and watershed boundaries and concluded that slope quality was function of both horizontal and vertical resolutions of DEMs. Quinn et al. (1991) kept focus on grid resolution impact on hydrological response and found that routing algorithm and flow path algorithm may have impact on model prediction for water table change and soil moisture status over time. With further understanding of topographic parameters, improvement in both DEM resolution and accuracy and development of topographic parameter derivation algorithms, there is an increasing need for assessment of high-quality topographic data in terms of data source, resolution, algorithms for topographic parameters estimation for various environmental applications.

Above all, research questions were raised as: 1) What DEM/DEMs in terms of resolution and data source is/are the optimum representative to the local topography for the hydrological applications? 2) Is there any optimum algorithm for the topographic parameters derivation? 3) What is the relationship between the key topographic derivatives and hydrological response?

1.5. Aims and Objectives

To address the research questions posed above, this study aims to assess the importance of topographic data on the sensitivity of flood extent prediction in upland moor-land environments. The study has the following specific objectives:

To

1) Acquire all available topographic data from various sources, such as production from digitised contour maps and InSAR images, generation from aerial photographs photogrammetrically and derivation from airborne laser scanning data;

2) Undertake a statistical analysis through comparisons or contrasts of the available DEM data to test sensitivity of key topographic attributes such as slope, aspect, profile curvature and the Topographic Wetness Index as coded in the widely used software packages, ArcGIS, ENVI and SAGA.
3) Investigate the impact of DEM data on flood inundation estimates from a 2D numerical model-FLOWMAP by simulating several flood events using all available DEMs as well as four stage datasets (including the actual event and three other scenarios) and comparing their inundation areas and patterns.

2. Datasets and Methodology

2.1. Aims and Structure

This chapter aims to generalise the data for topography-based geomorphological and hydrological research and specify to the available data for this study. In each part of the data description, the methodology used to incorporate the data into this study is explained.

2.2. General Datasets for Topography-based Geomorphological and Hydrological Research

Topographic data, imagery and field data are the normally three categories of data used for topography-based geomorphological and hydrological research. In particular, topographic data provides the topographic information for the research area at different time scales or spatial scales, imagery, as a direct visualisation tool and are also a source of topographic information and field data, such as ground control points, flow and stage are used as the reality for application input or validation. More details of these three categories of data are given below.

2.2.1. Topographic Data

The topographic data for an area describe the shape of earth surface, including one or more themes such as drainage information (i.e. location of a river or other water bodies), land cover statistics (e.g. density of vegetation), culture (e.g. location of road and rail network) and ground elevations etc. These data can be included in various formats, such as topographic maps and digital elevation data. Traditionally, topographic maps are produced based on paper while digital topographic maps have become available in recent

couple of decades. Current topographic maps are able to cover a nationwide area and hence can provide frameworks for specific research. Since maps have the nature in generalisation of reality, this kind of topographic data source were not frequently used and studied after digital elevation data was developed. Most current digital elevation data are produced from stereoscopic interpretation of aerial photographs or satellite imagery and more available digital elevation data are from digitising the contour lines, the use of GPS and airborne or space-borne remote sensing technologies, such as airborne Light Detection And Ranging (LiDAR), Interferometric Synthetic Aperture Radar (InSAR) from satellites or aircrafts. Digital elevation data are normally treated in three structures: regular grids known as gridded DEM, triangulated irregular networks (TIN) and digital contour lines. Though with at least three minor disadvantages in data storage, as computational efficiency, flat area representation and relatively inaccurate calculation of specific catchment areas, gridded DEMs are still most widely used digital elevation data, for their structural simplicity and capability in computer implementation (Wilson and Gallant, 2000). With the development of remote sensing techniques, DEMs are able to be acquired from a wider range of sources and at much finer resolution than before (from magnitude of kilometre to metre or even centimetre). Their quality directly leads the topographic information extraction and interpretation. Therefore, it is necessary to investigate the characteristics and abilities in topographic information representation in DEMs, gridded DEMs in this case, from different sources and at different resolutions. In this case, gridded DEMs (short as DEMs in later parts of this thesis) were chosen to be the studied topographic data.

2.2.2. Imagery

Imagery includes aerial photographs and satellite images ranging from airborne/space-borne metric/digital photographs, laser images to spectral images (including single, multi or full spectral bands as spectral resolution) at different spatial resolutions. Imagery contain massive amount of information and can be extracted using different approaches for different purposes. In this case, aerial photographs and laser images were mainly

treated as sources for DEM generation, as they contained up-to-date topographic information especially for rapid assessment. Visualised LiDAR points are able to provide more accurate and precise topography in a short period of both measurement and processing. However, remote sensing data have their defects. The remote sensing data (LiDAR and aerial photographs in this study) were acquired strictly due to schedules and in most cases they were not obtained particularly for a certain project, an event or an area, so that presumably the data can hardly meet the requirement for the research, such as image resolution, covering area and obtaining time etc. Furthermore, the post processing of data was normally not operated by researchers themselves. Therefore, the quality of data was not controllable and would possibly bring problems into a scheduled study.

2.2.3. Field Data

Field data composes of ground control points (GCPs), GPS RTK data, Electronic Distance Measurement (EDM or total station), recognisable feature maps, site photos, draft maps and ground-based laser scanning. The main feature of field data is its mobility and the reliability in data quality. Compared to remote sensing techniques, conducting a ground survey is more accessible for small area and high quality information in detail. However, as a traditional surveying method, though with most up-to-date computer programs, field work is still a time-consuming and cost-ineffective approach to obtain surface data over large areas for research.

2.3. Available Datasets in this Study

For the area of the North York Moors and the specific flood event on 19th June 2005 various sorts of datasets were available including raw data. Raw data included a location map, DEMs from the Ordnance Survey (OS) at two resolutions (10 m and 50 m) and scales (1:10 000 and 1:50 000), topographic maps at three scales from the OS (1:10 000, 1:25 000, 1:50 000), aerial photographs captured in two over-flights after the flood event

(in digital and metric formats respectively), LiDAR data and Airborne Thematic Mapper (ATM) data from the Natural Environment Research Council (NERC), pre-event photographs from the InfoTerra, an InSAR DEM (at 1:5 000 scale and at 5 m grid size resolution) from the NextMap, GCPs, checkpoints, EDM data, map of landslide distribution, GPS rover data and laser scanning data from intensive ground survey, rainfall, flow and stage data and flood extend prediction from the Environment Agency (EA). The large volume of data made it more important to organise the data and make full use of them properly and efficiently. The available datasets are summarised in Table 2.1.

Table 2.1Available datasets in this study

Type \ Source	Ordnance Survey	Natural Environment Research Council	University of Durham, UK	NextMap	InfoTerra	Environment Agency
Topographic Data	Digital topographic maps (1:10 000, 1:25 000 and 1:50 000); MasterMap™; OS DEMs; GCP Map	LiDAR DEM; a photogrammetrically derived DEM		InSAR DEM (1:5 000)	One DEM derived from pre-event aerial photographs	
Imagery		Post-event aerial photographs (1:6 000 taken on 23rd Jun. 2005; both 1:6 000 and 1:15 000 taken on 26th Aug. 2005);ATM imagery			Pre-event aerial photographs (taken on 30th Jul. 2001)	
Ground Survey			GCPs; site photos; GPS rover data; EDM results; notes; ground-based laser scanning; map of landslide scars			
Others						Stage data; flood inundation model prediction

2.4. Study Areas

Three rectangular areas in the North York Moors were chosen for this study and their locations, sizes and purpose for the study are summarised in Table 2.2.

Table 2.2 Study areas summary including their locations in Britain Grid Coordinate System, sizes and purposes in this study

Study Area	ULX/ULY	LRX/LRY	Area	Purpose
Whole study area	448975/500025	469025/486975	261.6 km^2	General assessment of DEMs
Head House area	452752/497942	454152/496232	2.4 km^2	Detailed assessment of DEMs
Model test area	455852/488518	456146/488084	128000 m^2	Test the flood model

Note: ULX, ULY, LRX and LRY mean the upper left x, upper left y, lower right x and lower right y values in an area.

Three areas were chosen with specific purposes. The Head House area, with the largest landslide in the area was selected for detailed investigation of the impacts from such geomorphological change; The whole study area, in contrast, contained the fewest geomorphological changes in percentage of area for validation of geomorphological impacts on topographic representation; The boundary of model test area was restricted by stage data to suit the hydrological model. River Rye, River Seph, River Riccal, River Hodge Beck and River Dove are the five main rivers in the whole study area flowing from north to south. River Seph joins in River Rye at Seph Mouth c. 500 m north to the Broadway Foot stage station, which is roughly in the middle reach of the River Rye in the flood model test area. The Head House area and the model test area are both parts of the River Rye catchments.

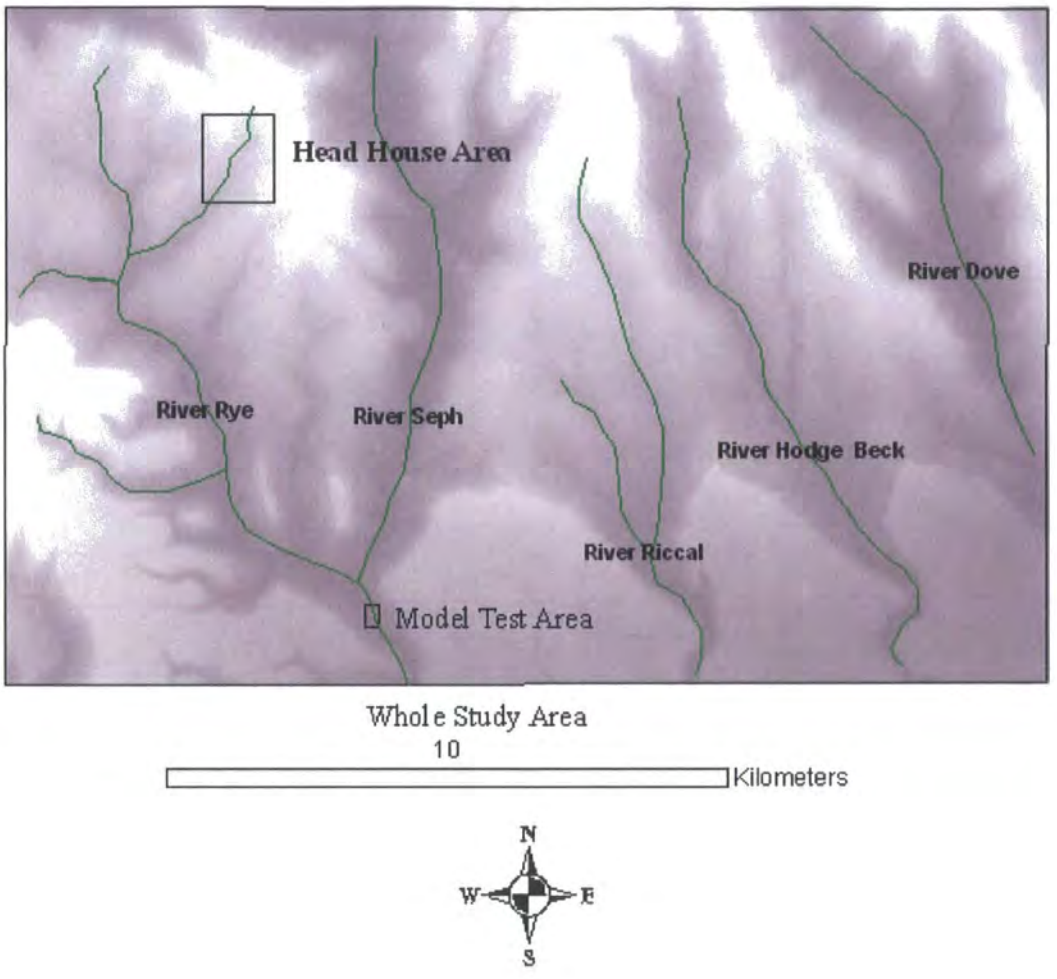

Figure 2.1 Study area draft

Fig. 2.1 shows the draft of topological relationship among the three study areas with the 50 m resolution SAR DEM and a river distribution map as background. Green lines show the five main rivers in the whole study area. Black boxes show the study area boundaries.

2.5. Topographic Data

2.5.1. The Ordnance Survey Maps

EDINA, based at the Edinburgh University Data Library, provides various online maps and other data to members of UK tertiary education institutions for academic

uses free of charge. The OS map, as one of its products, is fixed in the British National Grid Reference System (Fig. 2.2) in raster format.

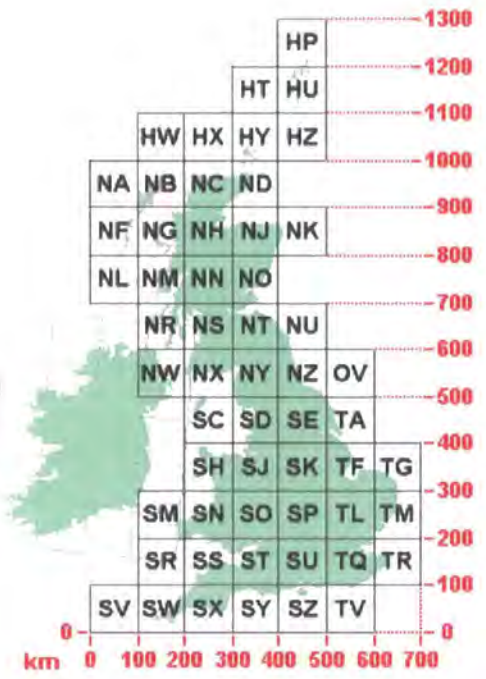

Figure 2.2 British National Grid Reference System grid key (from the OS website)

In the British National Grid Reference System, grids are formatted into 500 km by 500 km squares (prefixed by H, N, O, S and T). Each 500 km by 500 km square is divided into 25 squares of 100 km by100 km size with the second code letter from A in the north-west corner to Z in the south-east corner excluding 'I'. Within the code of each of these 100 km by 100 km squares, numbers are given to eastings and northings from the south west corner of each square. The maps are available in black and white and full colour, and contain all of the detail depicted on their paper equivalent, Landplan® plots, other than contours, contour values, air heights, and open sea stipple. All features are fully edge matched across each tile (The OS website, 2006).

Three different scales of OS Maps are available for this study. They are 1:10 000, 1:25 000, 1: 50 000. Their key parameters are summarised in Table 2.3.

Table 2.3 Ordnance Survey topographic maps

Parameter / Scale	Tile Size	Resolution (dots/inch)	Data Structure	Transfer Format
1:10 000	5 km by 5 km	400	Raster	TIFF 8 bit uncompressed
1: 25 000	10km by 10km	254	Raster	TIFF 8 bit LZW compressed
1: 50 000	20km by 20km	254	Raster	TIFF Palette 8 bit (256 colours) with LZW compression

In this study, the OS Maps were used for all geographical registration such as for the NERC aerial photographs. Generalisation of features is inevitable during the production of a map and the smaller scale the map is at, the more features are possibly generalised. For instance, a 1:50 000 OS map is expected to contain fewer features than 1:25 000 and 1:10 000 maps for the same area. Therefore, it is more difficult to identify small features on a smaller scale map and the mis-identification of some useful features, such as narrow road would normally degrade the quality of registration. For the reasons above, the 1:10 000 maps were chosen as the framework for this study. In this case, the research location is covered by twelve tiles: SE59SW, SE59SE, SE59NW, SE59NE, SE58NW, SE58NE, SE68NW and SE69NE and the Head House area is on tile SE59NW. The NERC 1:6 000 and 1:15 000 aerial photographs were registered to the mosaiced tiles of SE59SW, SE59SE, SE59NW, SE59NE, SE58NW and SE58NE. An example is shown in Fig. 2.3.

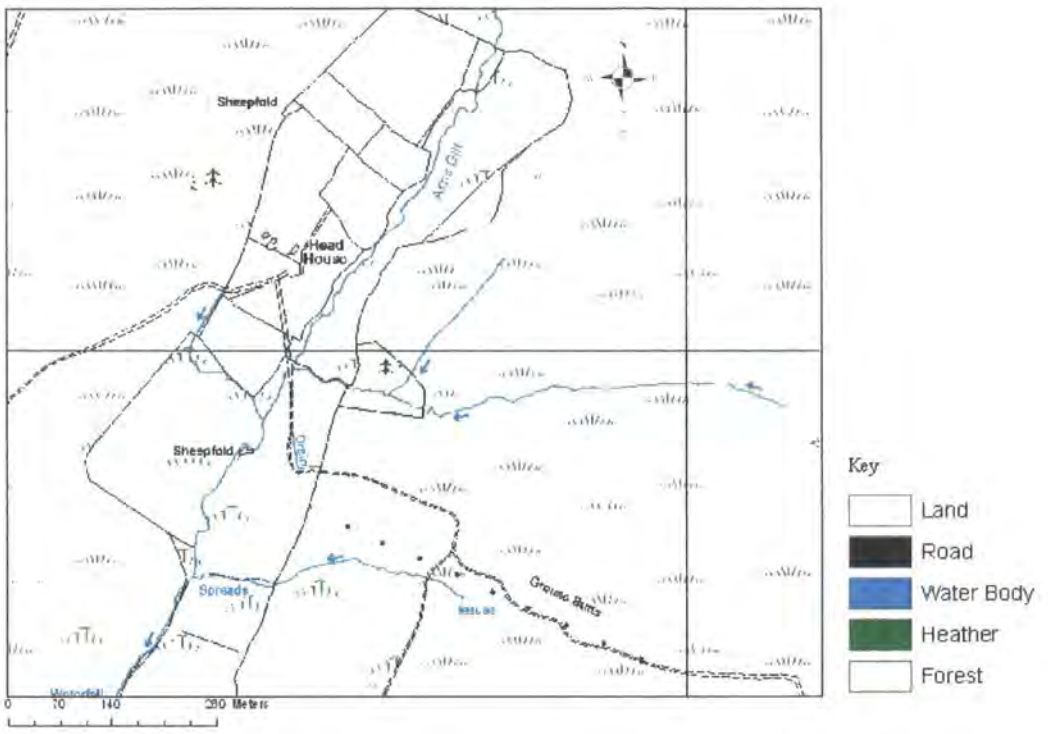

Figure 2.3 An OS digital topographic map at 1:10 000 scale of the Head House area

Fig. 2.3 shows the Head House area which contains a huge peat slide (possibly the largest in the England so far) on the 1:10 000 OS map of tile SE59NW. Blue lines represent water body, such as channels and streams. Double dash blue lines represent road systems, which vehicles can follow to. Light green polygons with symbols of a tree represent forests. Text notes are helpful to locate and identify specific research places, such as the Head House.

2.5.2. The OS MasterMap™

The OS MasterMap™, based on the 1:10 000 OS Map, is a large-scale, polygonised and seamless topographic database product in shape file format and contains several files and layers including an Imagery Layer, an Address Layer, an Integrated Transport Network™ Layer and a Topography Layer. The Topography Layer is continually revised to incorporate changes to both the urban and rural landscape (the OS website). Features such as roads and buildings on the Topography Layer are

given TOID® (TOpography ID) so that all other layers containing these IDs can be linked to the Topography Layer. The imagery layer contains highly accurate pictures of the nature. The Address Layer can be used to organise a transport and distribution plan.

In this study, the Topography Layer which contains the topographic information was used as a framework for creating new layers.

Details of its files including file name and the themes that are contained are given as followed:

1) Area_Centroid_Point;
2) Area_Centroid_Polyline;
3) Area_Mosaic_Polyline;
4) Carto_Symbol_Polyline;

Theme: Administrative Boundaries; Heritage and Antiquities; Terrain and Height; Water;

5) Carto_Area;

Theme: Land;

6) Carto_Text;

Theme: Administrative Boundaries; Buildings; Heritage and Antiquities; Land; Roads Tracks and Paths; Structures; Terrain and Height; Water;

7) Gazetteer;
8) Bndy_Line;

Theme: Administrative Boundaries;

9) Text_Centreline_Polyline;

Theme: Administrative Boundaries; Buildings; Heritage and Antiquities; Land; Roads Tracks and Paths; Structures; Terrain and Height; Water;

10) Topo_Point;

Theme: Administrative Boundaries; Land; Roads Tracks and Paths; Structures; Terrain and Height; Water;

11) Topo_Line;

Theme: Buildings; Land; Roads Tracks and Paths; Heritage and Antiquities; Structures; Water;

12) Topo_Point_Polyline;

Theme: Land; Structures; Terrain and Height; Water;

13) Topo_Area.

Theme: Building; Heritage and Antiquities; Roads Tracks and Paths; Land; Water; Structure.

Theoretically, boundaries of the river Rye can be illustrated by both polylines contained in the Topo_Line file and polygons contained in the Topo_Area file. However, some problems were derived during the data process such as the Topo_Line file misses a river bank so that it cannot fully describe the river boundary. In addition, Topo_Area describes the reach in the model test area by three polygons in the model test area. Therefore, a new layer as river shape file was created based on the Topo_Line, Topo_Area and the 1:10 000 topographic map.

(a) Topo_Area **(b) Topo_Line**

Figure 2.4 the OS MasterMap™ of the model test area

Fig. 2.4 shows the (a) Topo_Area and (b) Topo_Line file by screen shots of the OS MasterMap™ for the flood model test area. Light blue lines describe the river boundary in this area and the red line means the missing part in the Topo_Line file.

The new river layer was created based on the Top_Area layer and extracted to a new polygon shape file afterwards. The file was transformed to a grid raster at grid sizes of DEMs and then ASCII files for flood modelling. Therefore, an ASCII file for the river elevations contained two values: zero for river channels and -9999 for the floodplain as 'no data'. Uncertainty turned out when a vector shape file was transformed to a raster file for the river channel, which was also affected by the uncertainty in the OS MasterMap™ including river location and channel change.

These uncertainties may accumulate and contribute to the final result of hydrological model in Chapter 4.

2.5.3. DEMs

In this study, a DEM is used as a gridded digital terrain model (DTM), which shows only the underlying terrain without the information of vegetation, buildings or other artificial features in a rural environment. A DEM contains topographic information like elevations and horizontal locations. While a digital surface model (DSM) is defined as a digital model which measures the actual surface including any vegetation, buildings, or even vehicles, livestock and people during the acquisition. A DSM is usually the raw data obtained by a certain technique and above-ground information needs to be removed to create a DTM. In a DEM, X and Y coordinates determine the horizontal location of features. Added elevation information allows for a better representation of reality. For better understanding surface characteristics from this topographic information, various derivatives as indices of the topographic information can be derived from the composition of vertical and horizontal values. These surface derivatives have been used on many aspects for description and better understanding of reality. As derivatives' calculations involve different algorithms and different algorithms lead different estimations, to select a better algorithm for a certain derivative or even for certain characteristics of an area is also needed to be considered. Also, although using the same algorithm, different DEMs may produce different values of derivatives and hence contain different geomorphological and hydrological information. Therefore, DEMs varying in resolution and data source and also calculated using different algorithms are described in Chapter Three.

Two OS DEMs at 10 m and 50 m spatial resolution, which were derived from 1:10 000 and 1:50 000 topographic contour maps respectively, were acquired from EDINA in National Transfer Format (NTF) format and converted into ASCII files for gridded DEM and shape format using MapManager 6.2. Then the shape files

were transformed by the ENVI 4.1 package to image format for future processes using the Erdas IMAGINE™, ESRI package and other applicable packages.

In addition, a 1:5 000 scale InSAR DEM with the post horizontal spacing of 5 m and the vertical Root Mean Square Error (RMSE) of 0.7 m was generated from InSAR imagery by the NextMap of Intermap Technologies. The 5 m resolution DEM was sampled with two coarser spacing (10 m and 50 m) as followed. First, choose resample function in Data Management Tools module in the ArcGIS ArcToolbox. Then select the 5 m SAR DEM, set the output cell size (10 m and 50 m) and the re-sampling technique (bilinear interpolation in this case). Three re-sampling techniques are available as the nearest neighbour assignment, the bilinear interpolation and the cubic convolution. The nearest neighbour assignment is more suitable for categories data as this technique does not change the values of any input cells. Instead, it adjusts the value of a cell according to its nearest cell values. This means any values in the output file can definitely be found in the input file. Although this technique decreases the degree of generalisation, the output file cannot represent the details of real surface in a small area. The second method uses values of the four nearest input cell centres to determine the value in the output raster file so that this method smoothes the original DEM than using the nearest neighbour assignment. Similarly, cubic convolution calculates value from much more nearest input cells (16) so that it tends to sharpen the edges of the original data. The sharpest result would come from cubic convolution and this is unacceptable for the continuous surface. Therefore, comparing these three methods, bilinear interpolation was chosen as the re-sampling technique for the 5 m InSAR DEM.

Two additional DEMs derived from aerial photographs were available for the Head House area. They were a 3 m resolution DEM derived from the InfoTerra pre-event aerial photographs and a 0.5 m resolution DEM derived from the NERC post-event 1:6 000 aerial photographs using Leica LPS (Leica Photogrammetry Suite) module of Erdas IMAGINE™.

Large volume (4.55 GB) of high accuracy and precision LiDAR data were captured with Optech Airborne Laser Terrain Mapper (ALTM) 3033 (Fig. 2.5) mounted on Dornier 228-101 research aircraft (Fig. 2.6) for the Bilsdale area from 11 am to 1 pm on 3rd May 2006 by Airborne Research and Survey Facility (ARSF, formerly Airborne Remote Sensing Facility) of the NERC. Post processing was carried out by Unit for Landscape Modelling (ULM) at Cambridge University, the United Kingdom. The GPS data was processed on 21st July 2006 using the Applanix PosPac 4.2 package in the Universal Transverse Mercator Grid (UTM) in the World Geodetic System 1984 (WGS84). The laser data was processed on 2nd August 2006 using the Optech Realm 3.5 package. The output LiDAR data contained last pulse, first pulse and intensity in eleven strips (in the sequence of 1, 3, 5, 7, 9, 10, 11, 2, 4, 6 and 8 from west to east) fixed in the British National Grid in ASCII format. The four corner coordinates in the British National Grid of the whole coverage are listed below:

Corner 1 (Easting, Northing): 448459,498927

Corner 2 (Easting, Northing): 455389,501029

Corner 3 (Easting, Northing): 460195,487360

Corner 4 (Easting, Northing): 453065,485262

Figure 2.5 Optech ALTM 3033 (http://arsf.nerc.ac.uk/instruments/altm.asp)

Fig. 2.5 shows the Optech ALTM 3033 and its key parameters and the specific survey parameters are summarised in Table 2.4.

Table 2.4 ALTM Paramaters

	Scanning Rate (Pulse per Second)	Swath Width (m)	Average Density per Hectare (Points)	Scan Width (semi-angle in °)	Vertical Accuracy at 1200m Flight Altitude (cm)	Vertical Accuracy at 3000m Flight Altitude (cm)	Positional Accuracy	Average Flying Height (m)
Equipment Parameter	33000	870 to 2180	2000 to more than 10000	0 to 20	±15	±35	Better than 1/2 000×altitude	
Survey Parameter	33333			20				1100

Figure 2.6 ARSF Dornier 228-101 Research Aircraft (http://arsf.nerc.ac.uk)

A 5 m resolution LiDAR DEM was created using the TerraScan and TerraModel modules in the Bentley MicroStation® 8.1 package. In addition, a classification approach was used to remove the measurements on vegetations for the Head House area and model test area. Both unfiltered and filtered DEMs were used in the model test area to testify the classification algorithm. In this algorithm, an initial model was built with pre-set parameters by users. The lowest point on the selected maximum building size of surface were chosen as vertices of triangles and other measurements on the surface were used to calculate the angle and distance to the vertices. If the measurements exist within the distance to a vertex, as well as with a larger angle than the pre-set iteration angle to the vertex, they will be removed; if they have a smaller angle than the pre-set iteration angle, they will be added for creation more triangles to represent the surface (TerraScan User's Guide).

Since the mapper scanned the surface while plane flied, measurements on the surface were formed in a Zig-Zag way (Fig. 2.7). This pattern of measurements cause different density in points on the surface and therefore LiDAR data are renowned as point clouds. Surface point's distribution from LiDAR varies in locations. Higher density samples lie in the areas where scanning lines meet and this is the advantage for LiDAR to be able to represent more detailed surface in some area. For the same reason, LiDAR raw data contain data redundancy when gridded to a DEM since the maximum points distance was chosen as the finest DEM grid spacing.

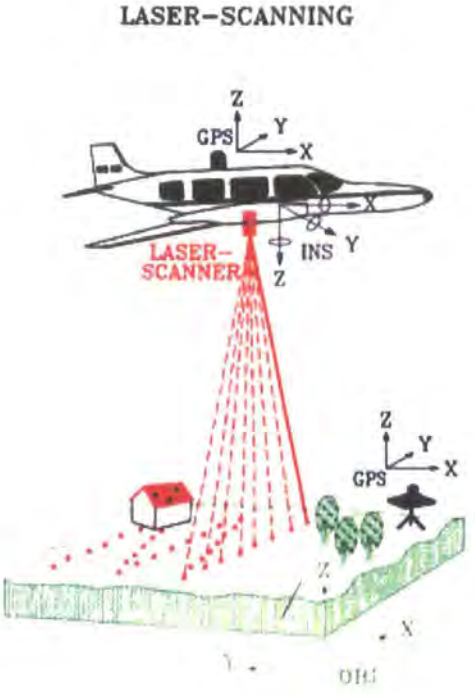

Figure 2.7 LiDAR operation principle illustration

Table 2.5 lists the strip number from west to east in this datasets, the points amount in both DEMs and raw data and their ratios.

Table 2.5 Strips and data redundancy

Strip Number	Points in the DEM	Points in Raw Data	Proportion (%)
1	2130744	5220547	40.8
3	3059731	6268653	48.8
5	3017512	6204998	48.6
7	3027024	6226539	48.6
9	2884416	5948605	48.5
10	2928872	5887257	49.7
11	3002366	6186907	48.5
2	2847651	6069954	46.9
4	2892610	5660441	51.1
6	2851002	5637887	50.6
8	2868616	5894319	48.7
Total	31510544	65206107	48.3

Due to computational limitation, these 11 strips have to be utilised to create DEMs separately.

Around 65 million points overall were obtained during the survey in all 11 strips and about 32 million which is 48.3% of the total points were generated into 11 separate DEMs of each strip coverage, which means two points' values in average in the raw data were assigned to one node in the DEM production. After mosaiced to one DEM, points with elevation decreased extremely to 3.6 million which was only 5.5% of total raw points and 11.4% of the whole points in DEMs of the 11 strips.

The LiDAR DEM of the Head House area (originally in strip 11, 2 and 4) shows small areas of missing data, which took place due to the inadequate overlap between strip 11 and strip 2 especially. In order to decrease the effect to the least degree, a consequence processes were done to revalue the grids in gaps:

Step one: transform the IMG format 5 m SAR DEM to an Arc/Info grid using the Arc/GIS workstation;
Step two: assign the grids in gaps in the 5 m LiDAR DEM with the values of the corresponding grids in the 5 m SAR DEM.

This treatment was conducted based on the assumption that high agreement between both 5 m DEMs in data gap areas and the visualisation showed no artificial feature was created (Fig. 2.8).

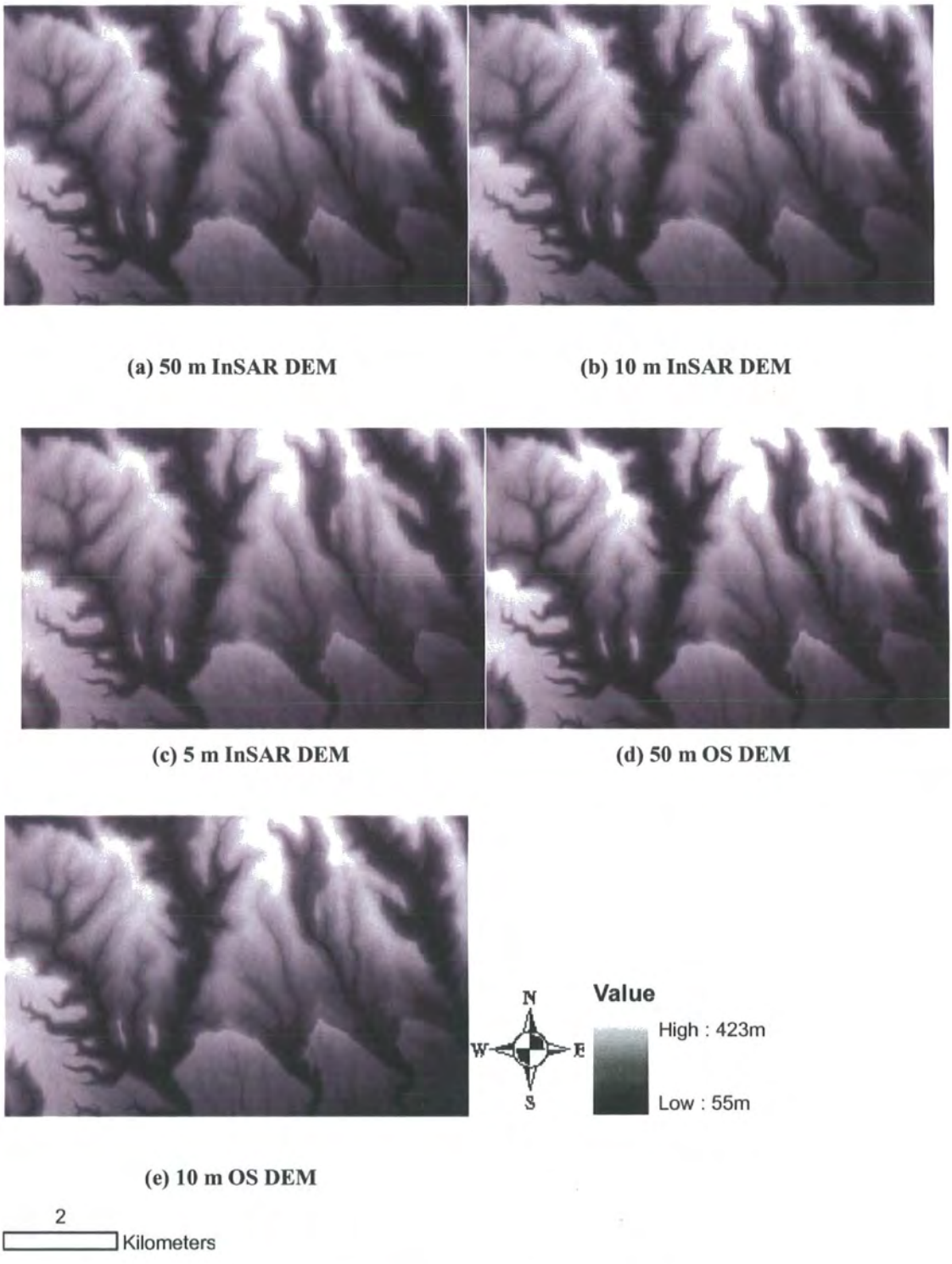

(a) 50 m InSAR DEM **(b) 10 m InSAR DEM**

(c) 5 m InSAR DEM **(d) 50 m OS DEM**

(e) 10 m OS DEM

Figure 2.9 DEMs of the whole study area

Fig. 2.9 shows the five DEMs (5 m, 10 m and 50 m grid size InSAR DEMs and 10 m and 50 m grid size OS DEMs) of the whole study area and the elevation scale is rescaled to 55 m to 423 m.

The statistics of all DEMs of the Head House area and the whole study area are briefly described in Table 2.6 and Table 2.7, respectively.

Each DEM was divided into two parts, river channel and floodplains. Both parts were transformed to ASCII format files. The pixel values of river channels were set to zero while those values of floodplains remained the same for the hydrological modelling. .

Table 2.6 Statistics of DEMs of the Head House area

DEM source	OS 1:10 000 contour maps	OS 1:50 000 contour maps	InSAR 1:5 000 imagery			InfoTerra APs	NERC APs	LiDAR measurements
Width/Height (pixel)	140/171	29/35	278/341	140/171	29/35	463/568	2773/3403	278/341
Block Width/Height (pixel)	64/64	29/35	64/64	64/64	29/35	64/64	64/64	64/64
Min (m)	247.9	248.0	247.2	248.6	249.8	249.3	242.8	245.0
Max (m)	383.2	383.0	384.4	384.6	386.1	385.0	383.7	384.4
Mean (m)	332.3	332.5	333.1	333.3	334.4	334.5	331.8	333.1
Median (m)	336.1	335.5	336.7	337.3	338.2	336.8	333.6	337.0
Mode (m)	320.8	320.8	321.7	353.8	359.5	320.9	347.3	352.8
Std. Dev. (m)	25.5	26.0	25.8	25.8	26.5	26.8	25.4	25.9
ULX/ULY	452757/497937	452757/497937	452757/497937	452757/497937	452757/497937	452757/497937	452757/497937	452757/497937
LRX/LRY	454143/496236	454143/496236	454143/496236	454143/496236	454143/496236	454143/496236	454143/496236	454143/496236
Pixel Size (m)	10.0	50.0	5.0	10.0	50.0	3.0	0.5	5.0

Table 2.7 Statistics of DEMs of the Whole Study Area

DEM source	OS1:10 000 contour maps	OS 1:50 000 contour maps	InSAR 1:5 000 imagery		
Width/Height (pixel)	2001/1301	401/261	4001/2601	2001/1301	401/261
Block Width/Height (pixel)	64/64	64/64	64/64	64/64	64/64
Min (m)	57.80	55.00	61.70	61.48	62.22
Max (m)	422.50	423.00	421.99	421.94	421.41
Mean (m)	246.62	245.40	246.97	246.94	246.67
Median (m)	240.15	241.88	243.25	243.12	241.81
Mode (m)	240.15	198.75	240.44	236.08	236.20
Std. Dev (m)	76.85	76.90	76.15	76.15	76.25
ULX/ULY	449000/500000	449000/500000	449000/500000	449000/500000	449000/500000
LRX/LRY	469000/487000	469000/487000	469000/487000	469000/487000	469000/487000
Pixel Size (m)	10.0	50.0	5.0	10.0	50.0

2.6. Imagery

2.6.1. ATM

ATM data were obtained and processed by the Airborne Research and Survey Facility (ARSF) of the NERC during the second over-light along with metric camera mapping on 26th August 2005 after the flash flood event. The ATM covered 12 bands as listed in Table 2.8.

Table 2.8 ATM spectral range

ATM Band	Spectral range (mm)
1	0.42 - 0.45
2	0.45 - 0.52
3	0.52 - 0.60
4	0.605 - 0.625
5	0.63 - 0.69
6	0.695 - 0.75
7	0.76 - 0.90
8	0.91 - 1.05
9	1.55 - 1.75
10	2.08 - 2.35
11	8.5 - 13.00
12	Spare thermal channel

The ATM data was in Hierarchical Data Format (HDF) from the AZ-16 mapper which contain GPS attitude and position data corrected for yaw, pitch and roll using an azimuth systems "azgcorr" (standing for azimuth geo-correction) in a UNIX system. Then, the data were transformed to TIFF files and imported to Erdas IMAGINE™ for the production of IMG files.

Figure 2.10 an processed ATM image

Fig. 2.10 shows one strip of ATM imagery with light blue as fields. Parameters of the ATM imagery are summarised in Table 2.9 and Table 2.10 below.

Table 2.9 Parameters of ATM 1

Date	Pixel Size	Camera	Number of Images
26/08/2005	1.5 m	ArgonST 1268	5
26/08/2005	5.0 m	ArgonST 1268	6

Table 2.10 Parameters of ATM 2

Instantaneous Field of View	2.5 mrad
Pixel swath	938
Digitised Field of View	90°
Scan Rate	12.5 , 25, and 50 Hz
Radiometric Resolution	16 bit
Temperature Reference	Two black-bodies for calibration of thermal channel

ATM imagery was also registered to the OS Maps for the production of land cover map containing land categories and interpretation of surface features.

2.6.2. Aerial Photographs

The NERC aerial photos were obtained on two stages in two categories as digital and metric photographs, respectively. They were prepared for DEM generation, validation for local geomorphological and hydrological information and flood extends recognition.

The digital photographs were obtained during the first flight on 23rd June 2005 (just four days after the flood) using a Rolleiflex 6008 single-lens reflex auto-focus camera, whose focal length was 50 mm and pixel size was 0.009 mm (36.9mm/4080). The field of view of the camera was 40.5°.

Figure 2.11 Rolleiflex 6008 (NERC)

Fig. 2.11 shows the camera. Table 2.11 summarises key camera parameters.

Table 2.11 parameter of Rolleiflex 6008

Capture rate	2s
CCD size	36.9 mm x 36.9 mm
CCD resolution	4080 x 4080
Bits per colour	16 bit
Output image size	96 MB
Image capacity	1000 images

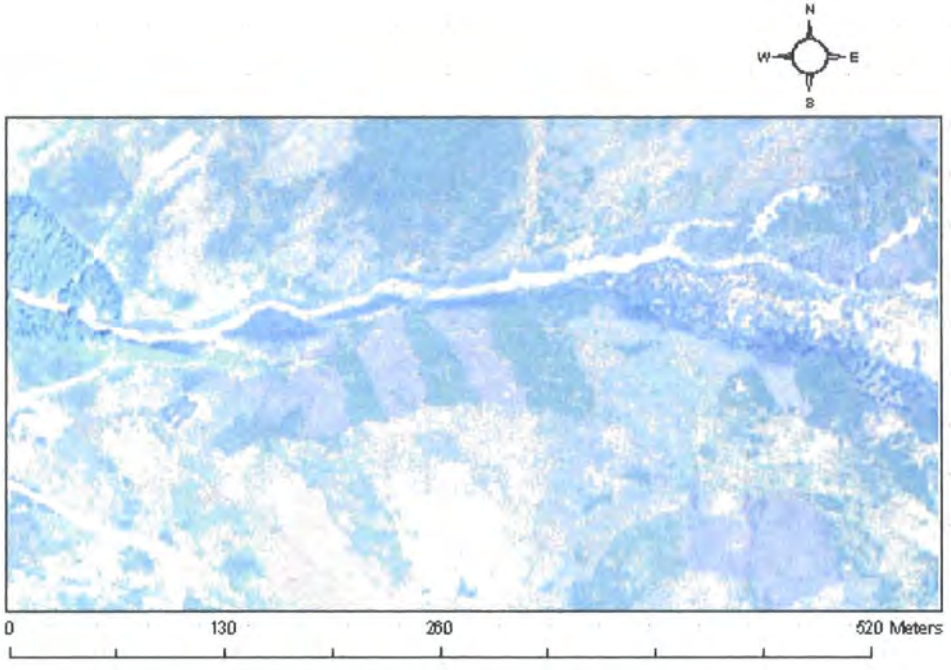

Figure 2.12 the aerial photo of the first over-flight (on 23/06/2005) of the Head House area

Fig. 2.12 illustrates the area of the Head House peat slide four days later the flood event. The aerial photographs were acquired using the Rolleiflex 6008 digital camera. The upper right corner shows the large peat slide and the white line downwards to the left shows the channel with flood water.

The metric photographs were obtained during the second flight arranged by the ARSF on 26th August 2005. Two different scales of images were obtained from different heights. The 1:6 000 scale sets were scanned by the BKS Surveys Ltd. and contained 44 photos while the 1:15 000 scale ones consisted of only 8 photographs for the same area. Amongst them, the aerial photographs of the Head House area

were scanned by the BKS Survey Ltd. and the others were scanned by the Design and Imaging Unit of Department of Geography at University of Durham. Parameters are summarised in Table 2.12 below.

Table 2.12 Parameters of Aerial Photographs

Data	Date	Pixel size	Camera	Number of photos	Scale
Aerial Photographs	26th Aug. 2005	8.7 cm	Zeiss RC-10	44	1:6 000
		22 cm	Zeiss RC-10	8	1:15 000

Figure 2.13 NERC Aircraft

Fig. 2.13 shows the NERC aircraft landing in an airport before the second flight was taken in the early morning of 26th August 2005.

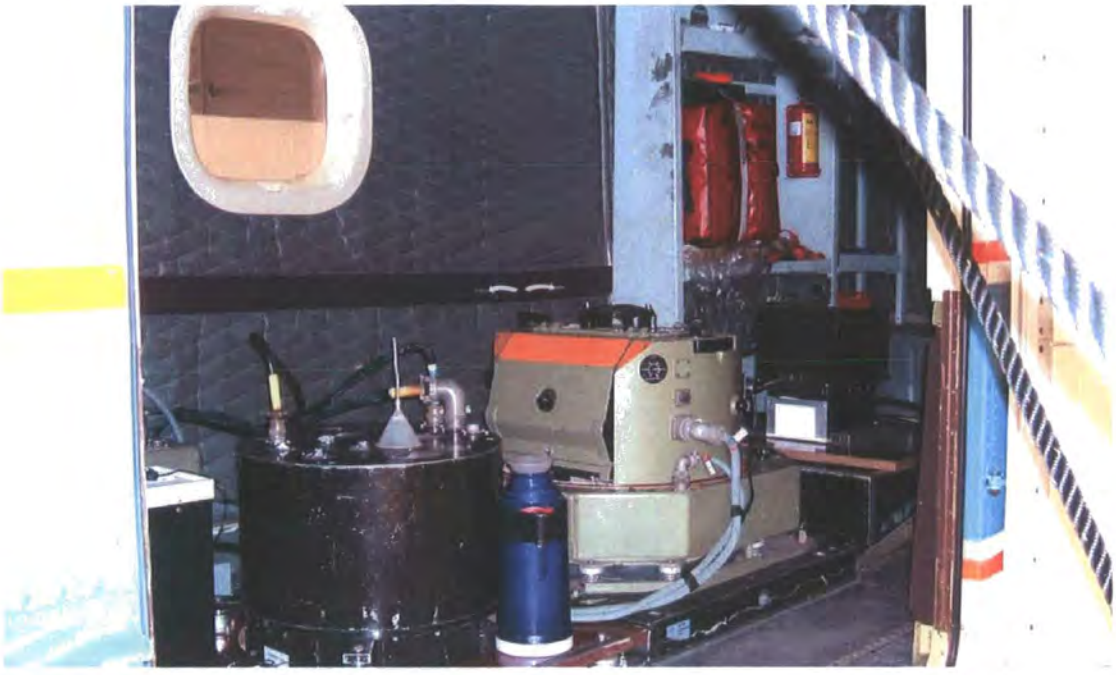

Figure 2.14 ATM and digital camera

Fig. 2.14 shows the mounting of the ATM and the metric camera Zeiss RC-10 inside the aircraft. The middle black one is the ATM sensor and the middle light green one is the digital camera.

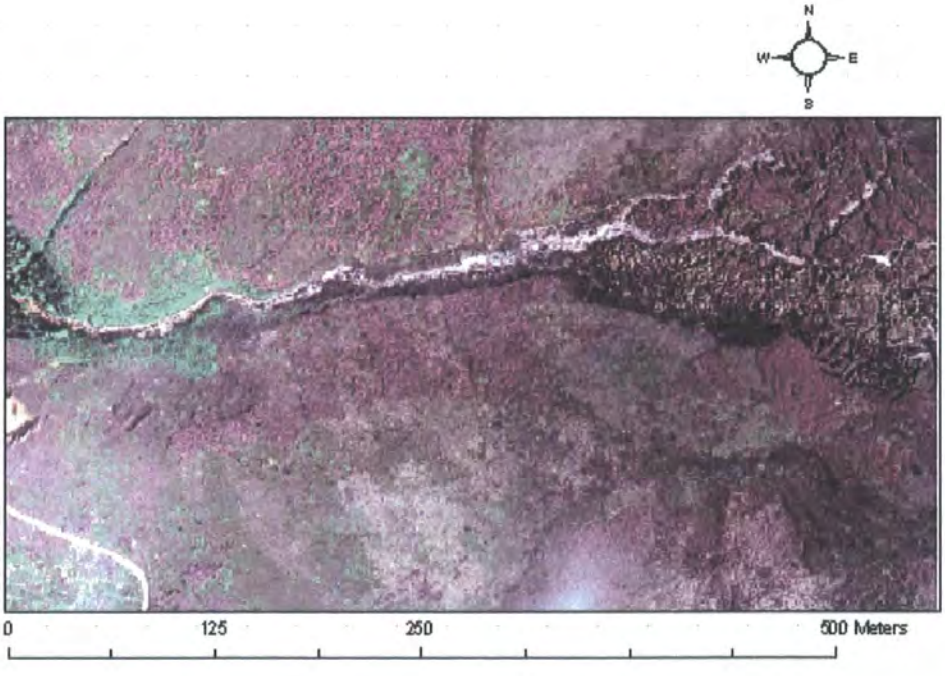

Figure 2.15 the 1:6 000 aerial photograph of the second over-flight (on 26th August 2005) of the Head House area

Fig. 2.15 is a screen shot of 1:6000 scale aerial photos of the same Head House area as Fig. 2.12 taken on 26th August 2005.

Aerial photographs were rectified using the Erdas IMAGINE™. In case there would be great distortion on edges of each photograph, both polynomial and rubber sheeting were chosen as geometric correction models for a test. The 1:10 000 OS topographic map with the tile key of SE59NE was chosen as reference dataset.

Leica Photogrammetry Suite Project Manager, the main component of the LPS was utilised for aerial triangulations. Pyramid layers including all images were set before processing and a registration model as Rolleiflex 6008 single-lens reflex auto-focus camera with parameters, as shown in Table 2.7, for the interior orientation. Image pyramid aims for faster processing by displaying sub-sampled original image. This option created reduced sub-sampled raster layers. There are several different re-sampling methods available for generating an image pyramid. Theoretical and practical investigations show that the re-sampling methods based on the Gaussian filter, which are approximated by a binomial filter, have superior properties concerning preserving the image contents and reducing the computation time (Wang, 1994).

The polynomial order was set to 2 in the polynomial model properties setting. This was due to that, a first order polynomial is generally used in case of transformation between two near recti-linear map systems. The second order polynomials are suitable for more different mapping systems, which were a film coordinate system and the British National Grid Coordinate System in this study. In addition, it is not necessary to choose the polynomial order larger than 2 considering the computation time. (Erdas Imagine 8.7 On-Line Help, 2006)

In the rubber sheeting model properties setting, linear method was selected and the nearest neighbour assignment was chosen as the re-sampling approach.

2.6.3. Pre-event Aerial Photographs

Pre-event aerial photographs coupled nine photos obtained from the InfoTerra and were acquired using a Zeiss RMK TOP 15 Aerial Camera (Fig. 2.16) on 30th July 2001 for the research location with total image unit-weight RMSE of c. 7.4 pixels. Photographs were scanned from the Kodak Panatomic X 3412 film at a resolution of 21 microns to achieve the ground resolution at 25 cm in TIFF format. Nine photos were geo-referenced to the Great Britain National Grid System and then mosaiced to produce an ortho-rectified photo in the Leica LPS module of the Erdas IMAGINE™. This image was prepared mainly for pre-event DEM extraction from aerial photographs.

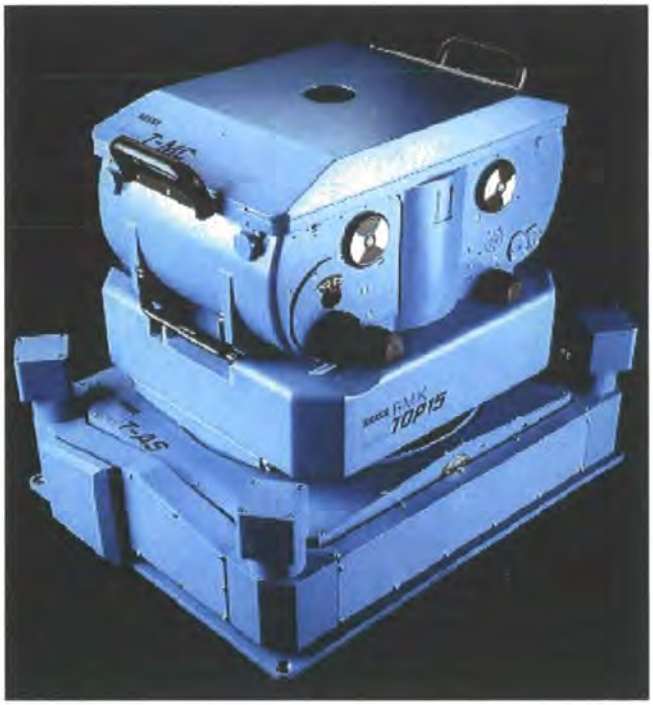

Figure 2.16 Zeiss RMK TOP 15 with a calibrated focal length of 153.971 mm (www.dammaps.com)

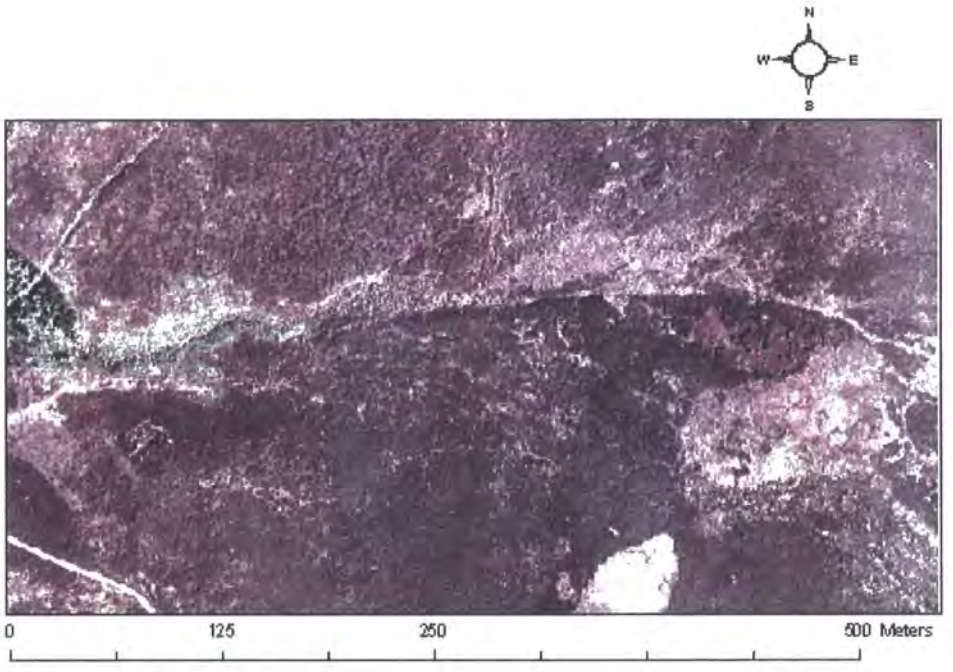

Figure 2.17 the pre-event aerial photographs of the Head House area

Fig. 2.17 provides a screen shot of the pre-event aerial photographs for the Head House area.

2.7. Field Data

Two ground surveys were conducted on 27th September 2005 and 15th February 2006, respectively. During the first survey, ground control points (GCPs) were set in the Head House area, and seven transects were measured along the Head House peat slide. During the latter survey, GPS rover and ground-based laser scanning were conducted in both Head House peat slide and Prodhills peat slide area. Five transects measurements were made in the latter peat slide area on the same day.

2.7.1. Ground Control Points

After setting the GPS ground base-station in an open and relatively high area, a differential global positioning system (DGPS) was used to measure every GCP. The control points were applied for three purposes: (x, y) position for aerial photo rectification; z value for DEM extraction; (x, y, and z) all coordinates as check points of DEM quality. With the high quality data generated from the DGPS, GCP location

information is able to provide more realistic value of natural field site than the remotely sensed data. Parts of these points were settled before transects. 1m by 1m square white plastic panels were laid over every GCP with the help of GCPs map and a draft map (Fig. 2.20). The white panels were chosen as symbols of GCPs for further survey, as they were easily identified in the field. Then wood pegs with red paint (also for identification) on the top were stocked to the ground accurately on the GCPs. The location on GCPs (on the top of pegs) and of points next to the GCPs on the ground were measured with DGPS. Their locations were carefully recorded on the draft map.

Figure 2.18 Setting a white plastic panel on a GCP and recording the location on a draft map

Figure 2.19 Dr. Jeff Warburton stands on a recognisable stone Using DGPS

2.7.2. Transects

Six and five transect measurements were conducted along the Head House peat slide and the Prodhills peat slide respectively using a Leica Total Station. The key parameters of the equipment are described below. Transects were set across the channel connecting pair of opposite GCPs. For a better accuracy, peg top and peg bottom were both measured for each GCP. Point spacing in each transect varied from approximately 10 cm to 1 m based on change rate of the local topography. For example, intensive points were set on slope, while fewer points were measured on the flat channel. Transects were specifically designed for assessment of flood impact as different type of area, such as side slope, flood edge, peat deposit, and channel were carefully recorded during the survey in each transect (Fig. 2.20).

Details of the equipment feature are given:

Angle accuracy: 5" ;

Measuring time: 1.5 seconds (with reflector, standard mode); 3-6 seconds (reflectorless, depending on distance and conditions);

Prism Range (1 prism, light haze, moderate sunlight, slight heat shimmer)

3000 m (circular prism)

1500 m (360 degree prism)

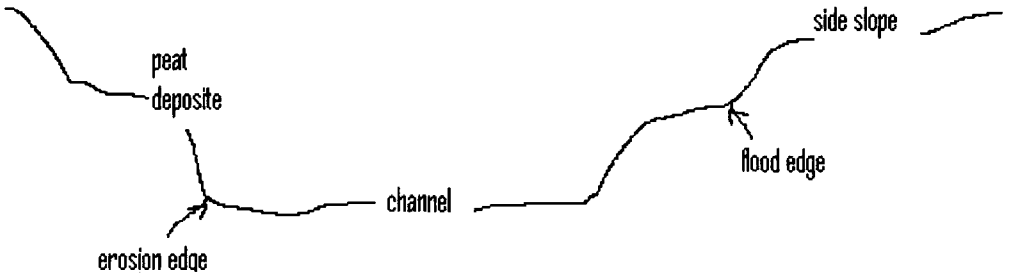

Figure 2.20 Transect draft

Fig. 2.20 illustrates each part of transect.

The flood extent was recorded as flood edge, where the maximum extent flood reached. The side slope was measured for potential analysis on geomorphology characteristics in the flood area. The erosion edges were mapped for estimation of erosion volume, which was done by Dr. Nikolaos Galiatstos.

2.7.3. GPS RTK

GPS Real Time Kinematic (RTK) was conducted in each peat slide area for landslide mapping by a Differential GPS (DGPS). DGPS is an enhancement to GPS that uses a network of fixed ground based reference stations to broadcast the difference between the positions indicated by the satellite systems and the known fixed positions. These stations broadcast the difference between the measured satellite pseudo-ranges and actual (internally computed) pseudo-ranges and receiver stations may correct their pseudo-ranges by the same amount. The RTK uses a single reference station (Fig. 2.22) to provide the real-time corrections of even to a centimetre level of accuracy. The reference station re-broadcasts the phase of the carrier (Fig. 2.21) that it measured, and the mobile units compare their own phase measurements with the ones received from the reference station.

Figure 2.21 Site photograph in the Head House peat slide channel on 27th September 2005 taken by Dr. Nikolaos Galiatstos

Figure 2.22 GPS base station on heather field taken on 27th September 2005

2.7.4. Laser Scanning

Laser scanning provides high resolution three dimensional (3-D) description of slide area directly. This result can be used to validate DEM quality and also as an alternative to those DEMs derived from remote sensing data, in small area.

Figure 2.23 MDL LaserAce® Scanner

Its features covers Eye safe laser range finder; 2300 ft/700 m Reflectorless Range; Accuracy 5 cm/2 inch, 0.1 ft /1cm resolution; 250 points per second; 3 million point onboard flash card data storage; Lighter weight at only 8.1Kgs/ 17.86Ibs and DC Power. Using it also has benefits like Surveying dangerous and inaccessible areas; Reducing Survey Costs; Saving time and money; Minimal operator training; Export data directly to CAD Systems and No need for external Computers or loggers. The instrument facilitates a numeric keyboard, which allows for a very flexible coding system when surveying individual features. Observations can be made manually, at a given separation or as a point cloud. Areas to be observed can be selected by rectangle or other polygons, and all observations were assigned to separate layers in the post-processing software.

Abbreviated technical specifications are described below:

Laser Module:

- Class 1 Eye Safe FDA/ IEC
- Type: Semiconductor, 905 nm
- Accuracy: Typically 2 inch/ 5 cm
- Range: Up to 2300 ft/700 m
- Prism Reflector: 5.0 km

Physical Data Construction:

- Machined Aluminium/ Polycarbonate
- Temperature Range: -20 °C to +45°C
- Water & Dust Resistant: IP66
- Weight: 8.1Kgs/ 17.86Ibs
- Size: 410 mm H x 239 mm W x 177 mm D

2.8. Other Datasets

Stage data was acquired from the Environment Agency as input raw data for the flood model operation.

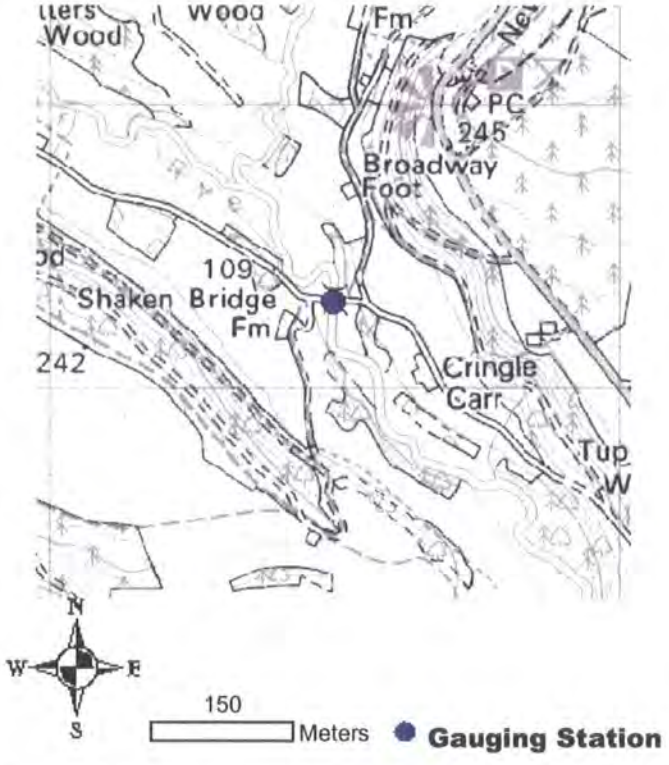

Figure 2.24 Gauging Station Map (from the EA website)

Fig. 2.24 shows the Broadway Foot gauging station on a 1:15 000 topographic map. The blue point in the centre of the map is the Broadway Foot gauging station on the River Rye.

Broadway Foot station was constructed on 1st September 1974 and the water stage data became applicable around three years later. Its bankful stage is 2.3 m and stage was measured every 15 minutes. The Broadway Foot station is the only stage station

in the study area and was destroyed by the flood in late afternoon of 19th June 2005 just after recent refurbishment and calibration.

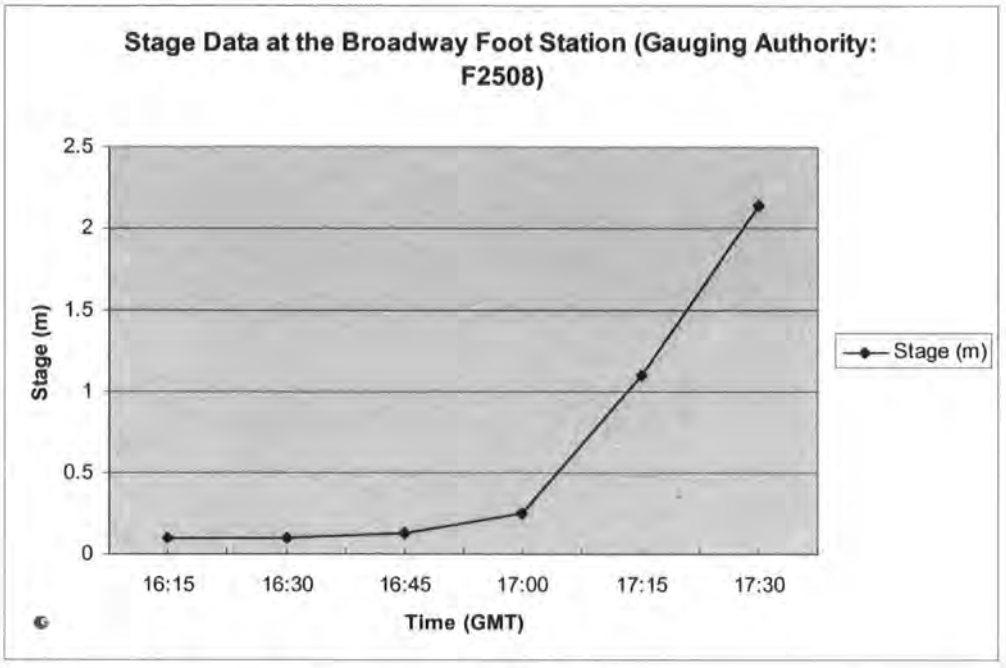

Figure 2.25 Stage data at the Broadway Foot station on the River Rye

Fig. 2.25 illustrates the unchecked stage data at the Broadway Foot station from the EA

The local stage data increased from 16.30 quickly especially after 17.00 and lasted for one hour until the station was destroyed by flood flow on 19th June 2005. The station elevation was extracted from the 10 m OS DEM, 5 m LiDAR DEM and 5 m SAR DEM, which were used for the hydrological model, as 96.100 m, 94.120 m and 94.085 m. The location of the station was based on the OS 1:10 000 topographic map using the ArcGIS package. Since no weight can be given to any of these values, mean value of the three elevations was set as the station elevation for the modelling, which was 94.768 m. Therefore the input stage elevation would be 92.468 m and the input stage would be the value plus the raw stage value so the stage elevation at each time point would be 92.568 m, 92.572 m, 92.598 m, 92.716 m, 93.573 m and 94.607 m with spacing of 15 minutes from 16.15 to 17.30 on 19th June 2005.

Figure 2.26 Broadway Foot gauging station (from the EA website, 2006)

Fig. 2.26 shows the weir where the gauge station was constructed.

2.9. Summary

Three sizes of study area were chosen for different purposes in this study in the North York Moors. Massive volumes of data in four categories were available for this study for the flood and landslide event on 19th June 2005, including topographic data, imagery and field data etc.

The topographic data varied in source and resolution. They included the Ordnance Survey topographic maps at three different scales (1:10 000, 1:25 000 and 1:50 000), the Ordnance Survey MasterMap™, the Ordnance Survey DEMs at 10 m and 50 m spatial resolution derived from 1:10 000 and 1:50 000 contour maps of the whole study area, 5 m, 10 m and 50 m resolution SAR DEMs of the whole study area, two DEMs at 0.5 m and 3 m resolution derived from post-event and pre-event aerial photographs of the Head House area from the NERC and the InfoTerra respectively and one 5 m resolution DEM generated from LiDAR points cloud of part of the River Rye catchment using a classification algorithm. The imagery varied in resolution and included the ATM image from NERC on 26th August 2005, digital aerial photographs and metric 1:6 000 and 1:15 000 aerial photographs taken by NERC on 23rd June 2005 and 26th August 2005 respectively and pre-event aerial

photographs taken on 31st July 2001 from the InfoTerra. Field data included GCPs, transects, GPS RTK and ground-based Laser scanning etc. In addition, stage data at the Broadway Foot Station on River Rye and the flood extent prediction from the model operation of the Environment Agency were acquired for flood modelling.

3. DEM Assessment

3.1. Introduction

DEMs are a major source of data for topography-based geomorphological and hydrological research and therefore their quality in terms of uncertainty in topographic representation is always of interest. Lane (2000) gave special attention to data quality assessment in photogrammetrically-derived DEMs for river channel morphology measurement through parameter reliability, automated detection and correction of surface errors. Since a reliable surface is one that is independent of variation in the parameters used to derive it, parameters of understanding the sensitivity of a surface to resolution and data source is concerned. Therefore, this chapter aims to analyse key terrain parameters derived from DEMs in relation to their sensitivity to horizontal resolution and derivation source of DEMs. Definitions of algorithms and parameters are introduced briefly before a quantitative comparison of DEMs is presented. Discussions and conclusions are given in the end of this chapter.

3.2. Research Issues

Geomorphology is being studied in two major ways: specific geomorphometry and general geomorphometry. The former focuses on precise operational definitions and the latter focuses on analysing the geomorphology as a continuous surface through attributes of sampling points on a surface. Many studies have shown the effects surface morphology has on catchment hydrology and other surface attributes, such as slope and aspect (e.g. Moore et al. 1988). Such attributes can be calculated from horizontal and vertical values of sampling points on a surface (Evans, 1981; Moore et al., 1991). DEMs as one digital elevation dataset, representing terrain, are one source of topographic information and have a wide range of applications in geomorphology (e.g. Jensen, 1991) and hydrology (e.g. Walker and Willgoose, 1999). All attributes are used to describe the nature of terrain surface, and an understanding of the nature of terrain improves the understanding of natural processes. Terrain shape governs flow routing and hydrologic response and hence affects the hydrological processes which in turn

have impacts on geomorphologic processes. In the NCGIA (National Centre for Geographic Information and Analysis, University of California, Santa Barbara, the United States, 1996), five scales were defined for various biophysical processes hierarchically: global-scale; meso-scale; topo-scale; micro-scale; and nano-scale; with topography governing the environmental processes in the topo-scale. The parameters derived from terrain data (DEMs in this case) are studied and shown to be of impact on environmental processes. For example, slope controls water flow direction. Profile curvature and plan curvature control the acceleration/deceleration and convergence/divergence of near-surface water flows (Heerdegen and Beran, 1982; Burt and Butcher, 1986). In addition, various horizontal resolutions (ranging from 0.5 m to 50 m in grid size) and sources (e.g. DEMs derived from Ordnance Survey digital topographic maps, InSAR imagery, aerial photographs and LiDAR measurements) of DEMs are available for this study and they provide an excellent opportunity to compare and contrast the derived topographic parameters.

Overall, two important research issues need to be clarified through the topographic parameter calculation:

1) Topographic parameters can be calculated using different algorithms (e.g. Heerdegen and Beran, 1982; Zevenbergen and Thorne, 1987). It is important to show the effect of algorithms on the results observed (e.g. Zhang and Montgomery, 1994). Whether or not an optimum algorithm exists for hydrological applications needs to be discussed.
2) With various DEM sources available, their ability to represent local topography needs to be investigated. In this study, DEMs derived from topographic contour maps, radar images, aerial photographs and airborne laser scanning (LiDAR) point clouds are considered.

Therefore, this chapter incorporates all available DEMs for this study area and assesses them quantitatively in terms of impacts of resolution, data source and topographic parameter calculation algorithm.

3.3. *Topographic Parameters*

3.3.1. Surface Definition

The primary topographic attributes are slope, curvature, and catchment area, etc. They are the derivatives of the surface topography. These derivatives measure the rate of elevation (z) change in response to changes in location (x and y). Their calculations depend on the definition of the topographic surface, and three methods are given below.

3.3.1.1. D8 (Deterministic Eight-Node) Method

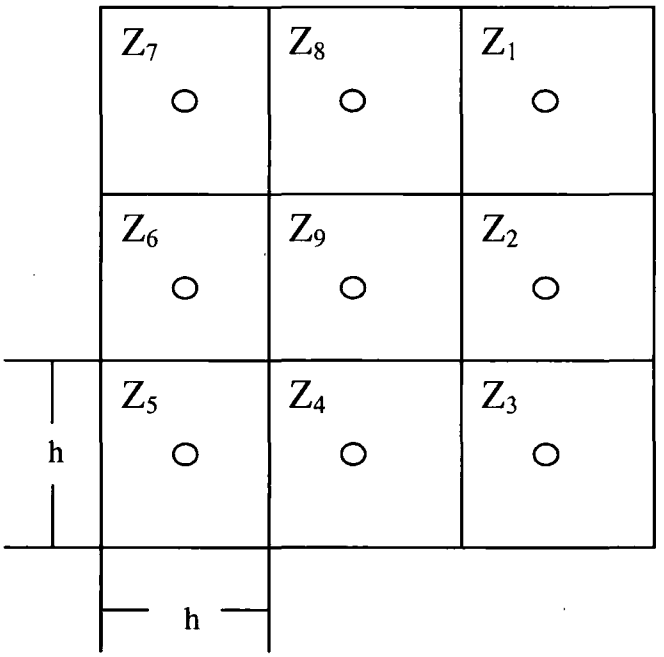

Figure 3.1 3×3 Subgrid for a gridded DEM (formatted from the figure in Wilson and Gallant, 2000)

Fig. 3.1 shows the arrangement and numbering of the nine grid points that enter into the finite-difference equations, and h is the grid spacing of the DEM. The y-axis, which points to north, is up in Fig. 3.1. (Wilson and Gallant, 2000)

$$z_X = \frac{\partial z}{\partial x} \approx \frac{z_2 - z_6}{2h} \qquad \textbf{Equation 3.1}$$

$$z_y = \frac{\partial z}{\partial y} \approx \frac{z_8 - z_4}{2h} \quad \textbf{Equation 3.2}$$

$$z_{xx} = \frac{\partial^2 z}{\partial x^2} \approx \frac{z_2 - 2z_9 + z_6}{h^2} \quad \textbf{Equation 3.3}$$

$$z_{yy} = \frac{\partial^2 z}{\partial y^2} \approx \frac{z_8 - 2z_9 + z_4}{h^2} \quad \textbf{Equation 3.4}$$

$$z_{xy} = \frac{\partial^2 z}{\partial x\, \partial y} \approx \frac{-z_7 + z_1 + z_5 - z_3}{4h^2} \quad \textbf{Equation 3.5}$$

$$p = z_x^2 + z_y^2 \quad \textbf{Equation 3.6}$$

$$q = p + 1 \quad \textbf{Equation 3.7}$$

Equations 3.1 and 3.2 are the first order derivatives that describe the rate of changes in elevations with distance along the x and y-axes, or the slope in those directions. Their values can be either positive or negative. Equations 3.3 and 3.4 are the second order derivatives that describe the rate of changes in the first derivatives in the x and y directions, or the curvature in those directions. Equation 3.5 is a mixed second derivative that describes the rate of changes of the x derivative in the y direction, or the twisting of the surface. Equations 3.6 and 3.7 are combination of terms that are used in several places in subsequent equations.

As these surface attributes are acquired by sampling the local area (i.e. a 3×3 cells square) around a specific point, generalisation of information is inevitable. The generalisation in this process may affect the surface attributes determined, so that two different window sizes were chosen for contrast.

3.3.1.2. Evans Full Quadratic Surface

Evans (1979) introduced a full quadratic surface using a 3×3 sub-matrix of elevation values (Fig.3.2), which is described mathematically by Equation 3.8.

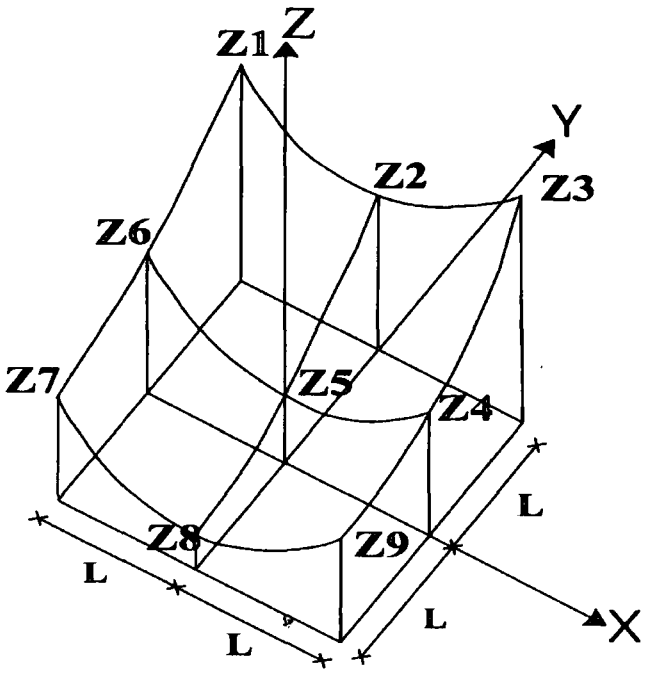

Figure 3.2 3×3 Elevation sub-matrix (Zeverbergen and Thorne, 1987)

Fig 3.2 shows the 3×3 elevation sub-matrix used in both Evans (1979) and Zeverbergen and Thorne (1987), where Z_1 to Z_9 represent the elevation values of nine points in this sub-matrix, and L in the same unit as Z, is the distance between neighbouring points in row or column directions (Zeverbergen and Thorne, 1987).

$$Z = ax^2 + by^2 + cxy + dx + ey + f \qquad \textbf{Equation 3.8}$$

Evans (1979) used Equation 3.8 as the full quadratic to represent the surface, where (x, y) is the point coordinate and x=y=0 in the central point. The nine elevations of the 3×3 sub-matrix are used to derive the coefficients, a to f as

$$a = \frac{Z_1 + Z_3 + Z_4 + Z_6 + Z_7 + Z_9}{6L^2} - \frac{Z_2 + Z_5 + Z_8}{3L^2} \qquad \textbf{Equation 3.9}$$

$$b = \frac{Z_1 + Z_2 + Z_3 + Z_7 + Z_8 + Z_9}{6L^2} - \frac{Z_4 + Z_5 + Z_6}{3L^2} \qquad \textbf{Equation 3.10}$$

$$c = \frac{Z_3 + Z_7 - Z_1 - Z_9}{4L^2} \qquad \textbf{Equation 3.11}$$

$$d = \frac{Z_3 + Z_6 + Z_9 - Z_1 - Z_4 - Z_7}{6L} \qquad \textbf{Equation 3.12}$$

$$e = \frac{Z_1 + Z_2 + Z_3 - Z_7 - Z_8 - Z_9}{6L} \qquad \textbf{Equation 3.13}$$

$$f = Z_5 \qquad \textbf{Equation 3.14}$$

Coefficients like a, b and c have specific significance on geomorphological representation as,

if $c^2 - 4ab < 0$, section is elliptic
if $c^2 - 4ab = 0$, section is parabolic
if $c^2 - 4ab > 0$, section is hyperbolic

3.3.1.3. Partial Quadric

Zeverbergen and Thorne (1987) modified Equation 3.8 to give Equation 3.15, a more general surface description that meets the needs of application for the Topographic Wetness Index (TWI) to the prediction of flow and sediment transport. It is suggested that the appropriate grid resolution, L, should be chosen to more fully replicate the real surface.

$$Z = ax^2y^2 + bx^2y + cxy^2 + dx^2 + ey^2 + fxy + gx + hy + i \qquad \textbf{Equation 3.15}$$

Following Equation 3.8, the coefficients in Equation 3.15 are also derived from the nine elevation values and the grid size as

$$a = \frac{\frac{Z_1 + Z_3 + Z_7 + Z_9}{4} - \frac{Z_2 + Z_4 + Z_6 + Z_8}{2} + Z_5}{L^4} \qquad \textbf{Equation 3.16}$$

$$b = \frac{\frac{Z_1 + Z_3 - Z_7 - Z_9}{4} - \frac{Z_2 - Z_8}{2}}{L^3} \qquad \textbf{Equation 3.17}$$

$$c = \frac{\frac{-Z_1 + Z_3 - Z_7 + Z_9}{4} + \frac{Z_4 - Z_6}{2}}{L^3} \qquad \textbf{Equation 3.18}$$

$$d = \frac{\frac{Z_4 + Z_6}{2} - Z_5}{L^2} \qquad \textbf{Equation 3.19}$$

$$e = \frac{\frac{Z_2 + Z_8}{2} - Z_5}{L^2} \qquad \textbf{Equation 3.20}$$

$$f = \frac{-Z_1 + Z_3 + Z_7 - Z_9}{4L^2} \qquad \textbf{Equation 3.21}$$

$$g = \frac{-Z_4 + Z_6}{2L}$$ **Equation 3.22**

$$h = \frac{Z_2 - Z_8}{2L}$$ **Equation 3.23**

$$i = Z_5$$ **Equation 3.24**

Similar to Evans (1979), the values of the coefficients a, b and h have significances in geomorphological representation (Stephenson, 1973, p.463) :

ab - h2 > 0 elliptic
if, ab - h2 = 0 conic is parabolic
ab - h2 < 0 hyperbolic

The following subsections introduce a number of software packages that have been used in this study, several topographic derivatives with their definitions, their potential function in geomorphological and hydrological research, as well as the different algorithms used in this study based on the three different definitions of the surface above.

3.3.2. Software Packages

Four software packages were introduced for topographic attributes derivation in this study: the Erdas Imagine™ 8.7 from Leica Geosystems; the ENVI 4.1/4.2 from RSI (Research Systems, Inc.); the ArcGIS from ESRI (Environmental Systems Research Institute); and the SAGA 2.0 (System for Automated Geoscientific Analyses) recently developed by the SAGA user group association of the University of Goettingen, Germany (the software is available at http://www.saga-gis.uni-goettingen.de). The first three packages are commercial software packages specially designed for GIS and remote sensing applications, acting with high price for every license. SAGA is an open resource programme written in C++, covering various environmental applications including hydrology and geomorphology.

ENVI, Arc/Map and SAGA were used to calculate the topographic parameters and each one employed a different algorithm. The ENVI used the full quadratic surface in Evans (1979) (Equation 3.8), the Arc/GIS used the D8 method (Equation 3.1 to

Equation 3.7), and the SAGA used the modified quadratic surface in Zeverbergen and Thorne (1987) (Equation 3.15).

Before all derivatives were calculated, pits or depressions in the DEM should be filled (Planchon and Darboux, 2002). In filling the pits and depressions, the elevation of pit/depression was adjusted to the value of the surrounding point, which had the lowest elevation value. Pits or depressions may come from errors in DEM generation or the real surface and they were recognised as the area with higher elevation points all around (Jenson and Domingue, 1988). However, depression filling may cause direction and flow mass change. This is because flow routing is directly governed by gravity. Assuming water only move to one of the eight neighbouring cells in a 3 by 3 cells window, it always goes into a neighbouring cell with the lowest elevation. According to its definition, a depression has the lowest elevation amongst all cells including the depression boundary, so that depressions or pits must be filled to ensure the correct flow routing. When calculating the primary flow direction before sinks or depressions are filled, none of the surrounding cells may have a lower elevation value than the node. In this case, the node is regarded as a flat area or a sink. Various algorithms have been developed for depression filling; however, the depression filling algorithm was not tested as an issue and only one method was used for computing in this chapter.

3.3.3. Slope

As a first order function of elevation, slope S is defined as a measure of how steep the landscape is. It is usually expressed in degrees or as a percentage. Using all the three software packages, slope is measured in degrees from a horizontal plane commencing from 0 degree. Slope is very crucial in geomorphology and hydrology, as gravity leads flow of water, soil and other materials by slope (Wilson and Gallant, 2000). Many researchers have used their own slope calculations to achieve while different software packages may use different algorithms.

The ArcGIS employs the D8 method (Equation 3.25), where slope is the maximum rate of change in elevation over each cell as well as its eight neighbours. This

method, suggested by O'Callaghan and Mark (1984), assumes that flow from a cell only accumulate into one of the eight nearest neighbours with primary flow direction.

$$S_{D8} = \max_{i=1,8} \frac{z_9 - z_i}{h\phi(i)} \qquad \textbf{Equation 3.25}$$

where $\Phi(i) = 1$ for cardinal (north, south, east, and west) neighbours (when i= 2, 4, 6, and 8) and $\Phi(i) = \sqrt{2}$ for diagonal neighbours to account for the extra distances to those cells (Fig.3.1), while the latter one depends on one of the eight nearest neighbours. The D8 method gives slightly smaller average slopes than the finite difference method (Wilson and Gallant, 2000). It is used when the slope of channels is required, due to the fact the finite difference estimate of channel cell slope may be affected by steep slopes adjacent to the channel.

The ENVI 4.1 uses the definition of

$$S = \arctan(d^2 + e^2)^{\frac{1}{2}} \qquad \textbf{Equation 3.26}$$

based on Equation 3.8.

For the SAGA, the slope S is calculated based on the partial quadric surface description Equation 3.15 as

$$S = \sqrt{(g^2 + h^2)} \qquad \textbf{Equation 3.27}$$

3.3.4. Aspect

As another first order function of elevation, the aspect Ψ generally refers to the direction to which a slope faces. The aspect angle is measured with the convention of 0 degree to the north (up) with angles increasing clockwise. An aspect image at a well-chosen colour scale can represent a good landscape visualisation (Kimerling and Moellering, 1989). A more important use of aspect is to calculate the primary flow direction. It should be noted that, as aspect reflects the direction of a slope, it could be meaningless in areas with very small slopes.

For the ArcGIS, the aspect is calculated with the D8 method, approximately,

$$\Psi_{D8} = 45j \qquad \textbf{Equation 3.28}$$

where j is the i that gives the largest slope value and hence is the direction of steepest descent, so that there could only be eight kinds of value in aspect and eight primary flow directions using the D8 method.

For the ENVI 4.1, the algorithm is based on Equation 3.8,

$$\Psi = \arctan(\frac{e}{d}) \qquad \textbf{Equation 3.29}$$

For the SAGA, the aspect Ψ is calculated as

$$\Psi = \arctan\frac{h}{g} \qquad \textbf{Equation 3.30}$$

3.3.5. Profile Curvature

As a second order function of elevation, the profile curvature (intersecting with the plane of the z-axis and aspect direction) measures the rate of change of the slope along the profile in radians per metre. The profile curvature measures the maximum gravity effects in the direction orthogonally, so it is important for characterising changes in flow velocity and sediment transport processes.

The ArcGIS calculates only curvature instead of separating into two directions as profile curvature and plan curvature.

For the ENVI 4.1, the profile curvature is calculated based on Evans (1979),

$$\Pr C = \frac{-200(ad^2 + be^2 + cde)}{(e^2 + d^2)(1 + e^2 + d^2)^{1.5}} \qquad \textbf{Equation 3.31}$$

Using this equation for calculation, the profile curvature is negative for slope increasing downhill (as convex) and positive for slope decreasing downhill (as concave).

The SAGA calculates the profile curvature as

$$\Pr C = \frac{-2(dg^2 + eh^2 + fgh)}{g^2 + h^2} \qquad \textbf{Equation 3.32}$$

3.3.6. Plan Curvature

As another second order function of elevation, the plan curvature (intersecting with the XY plane) measures the rate of change of the aspect along the plan. It measures the minimum gravity effects in the direction orthogonally. In other words, plan curvature measures the convergence and divergence in surface so that it reflects the trend water flow converges or diverges.

For the ENVI 4.1, plan curvature is calculated as

$$\mathrm{P}lC = \frac{200(bd^2 + ae^2 + cde)}{(e^2 + d^2)^{1.5}} \qquad \textbf{Equation 3.33}$$

Using this equation for calculation, plan curvature is negative for diverging flow (e.g. ridges) and positive for converging flow (e.g. valleys).

The SAGA calculates the plan curvature as

$$PlC = \frac{2(dh^2 + eg^2 - fgh)}{g^2 + h^2} \qquad \textbf{Equation 3.34}$$

3.3.7. Topographic Wetness Index

As an important secondary topographic attribute for hydrological research, the Topographic Wetness Index is also concerned in this study. In literature, the TWI is defined in three ways, i.e. in Barling (1992)

$$TWI = \ln(\frac{A_e}{\tan\beta}) \qquad \textbf{Equation 3.35}$$

where A_e represents effective upslope contributing area (m^2/m) and β is local slope angle (in degrees). The TWI may also be named as wetness index, topographic index, compound topographic index, and is assumed to control the soil wetness

pattern for topography (Wilson and Gallant, 2000). The upslope contributing area stands for the area of a catchment, which has contributed to the upslope rainfall-runoff per length of contour.

This equation is based on several assumptions: water flow is even and every calculation unit gets contribution from its entire upslope contributing area; there are no special sinks in the catchment; local surface slope value can be taken as the subsurface slope to calculate the direction of subsurface flow; and there is no downhill drainage from downhill. If these assumptions are met, the TWI will reflect the likely distribution of variable source areas within a catchment and can be used for saturation excess overland flow and subsurface flows (Quinn et al., 1995).

The algorithm for local slope angle has been summarised in section 3.3.3. A further factor in calculating the TWI is the upslope contribution area A_e. In literature, several methods have been described to calculate the upslope contribution area, e.g. the single flow direction algorithm in O'Callaghan and Mark (1984) and a multiple flow direction algorithm in Quinn et al. (1991).

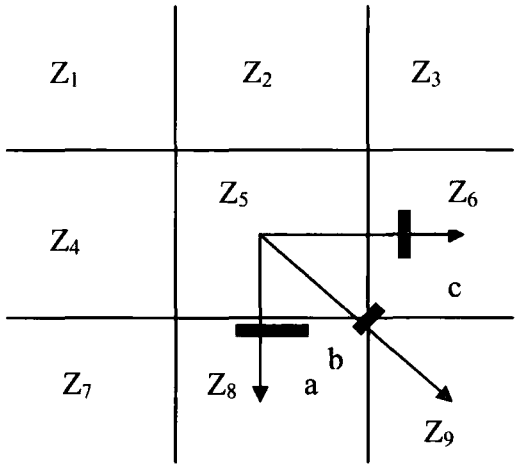

Figure 3.3 Multiple Flow Direction (Quinn et al., 1991)

Fig. 3.3 illustrates an example for the multiple flow direction method described in Quinn et al. (1991) in a 3×3 subsection of a DEM, where Z_5 is larger than Z_8, Z_9, and Z_6. In this case, outflow from the central cell has multiple directions to the latter three cells. The outflow proportions a, b, and c are defined as

$$a = 0.5\frac{\tan(Z_5 - Z_8)}{L} \quad \textbf{Equation 3.36}$$

$$b = 0.354\frac{Z_5 - Z_9}{\sqrt{2}L} \quad \textbf{Equation 3.37}$$

$$c = 0.5\frac{\tan(Z_5 - Z_6)}{L} \quad \textbf{Equation 3.38}$$

where L is the grid size of the DEM.

O'Callaghan and Mark (1984) described the single flow direction of the D8 method, which allows outflow from the central cell only going to one neighbouring cell with the steepest positive slope. Due to its simplicity, the D8 method is widely used for determination of the upslope contribution area. However, Wilson and Gallant (2000) summarised two drawbacks in this method: 1) this method cannot model flow divergence in ridge area, and 2) the flow direction is generalised to only one of the eight directions which may not fully represent the reality.

3.4. Calculation

The calculation procedure is described.

Firstly, DEMs were reviewed and checked based on elevation features such as peak, ridge and channel edges etc. The Swipe function of the Erdas IMAGINE™ 8.7 was used to help identify any offset between different DEMs. No obvious planmetric offset was detected.

After sinks in the DEMs were filled using the Arc/GIS (mentioned in Section 3.3.2), DEMs were processed using the topographic modules in the ENVI 4.1. Topographic modelling was used to generate shaded surfaces and to extract parameters for slope, aspect, and profile curvature (Equations 3.1-3.7). All these derivatives were computed using a quadratic surface. In this process, the topographic kernel size was set to 3×3 and 5×5 for calculating slope, aspect and profile curvature respectively. Afterwards, these parameters were transformed into ESRI grid file format for further analysis using the Arc/GIS.

For the primary topographic attributes, all these parameter images as well as the ortho-rectified aerial photographs were implemented in a new ArcGIS project. By using the Minus function in the Spatial Analyst Tools, image differences between each pair of DEM for every parameter were extracted. For the analysis in the ENVI 4.1, calculation results were compared in terms of histograms and 2D scatter plots.

For the Topographic Wetness Index, this experiment employed a powerful open source software package named SAGA (System for Automated Geoscientific Analyses) developed by O. Conrad and his group of University of Goettingen in Germany. This package took less than 10 megabytes space in hard drive with all available modules. Users can customise the modules they would need to load on each machine. Its functions cover terrain analysis, geostatistics, and simulation. Furthermore, researchers are able to develop a customised module and integrate this into the whole package.

Operations are done step by step in the SAGA:

1) First, export a dem.img to dem.grd (surfer grid) file;
2) Then import the surfer grid file in the import/export grids module;
3) Then fill sinks of original DEM with the Fill Sinks function (Planchon and Darboux, 2002) in the Terrain analysis- pre-processing module;
4) Then derive terrain attributes: slope, aspect and profile curvature with the method of Fit2. Degree Polynom (Zevenbergen and Thorne, 1987) in the terrain analysis morphometry module with the local morphometry function;
5) Then calculate the catchment area with multiple flow direction method (Moore et al., 1993d) in the terrain analysis hydrology module with the parallel processing function;
6) Then derive the TWI in the terrain analysis index module;
7) Then export ESRI Arc/Info to save the file to an ASCII file in the export grid module; and
8) Finally convert the ASCII file to a raster with the Arc/GIS conversion tools in type of float for further analysis in the Arc/GIS.

3.5. Results

Results are described by DEMs and topographic attributes including slope, aspect, profile curvature and the Topographic Wetness Index. In each part, quantitative and statistical analyses are given.

3.5.1. DEMs

3.5.1.1. Elevation Distribution

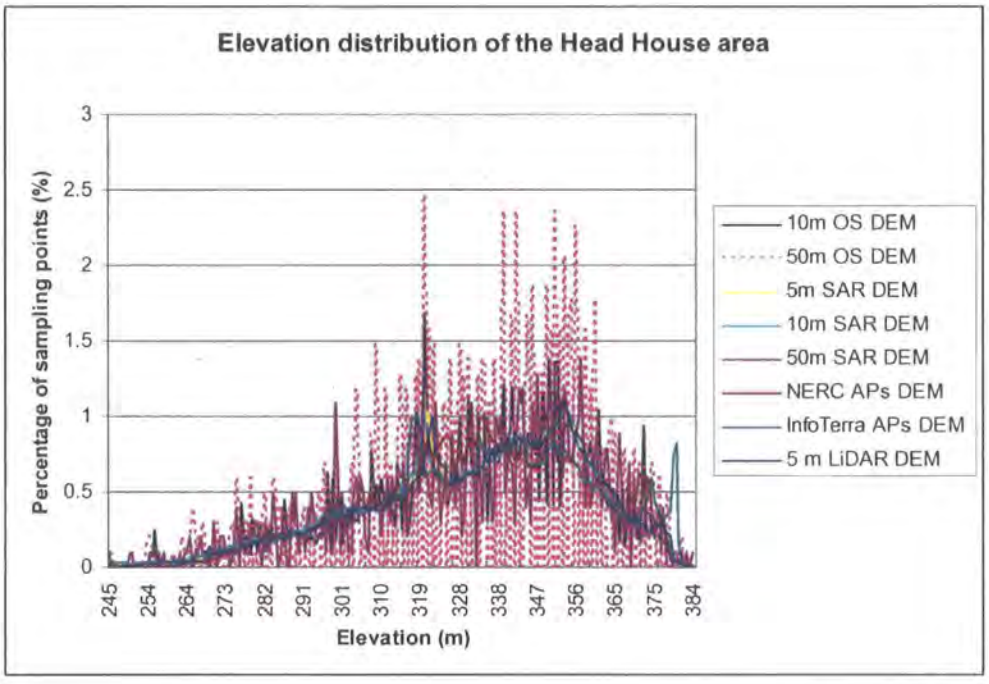

Figure 3.4 Elevation Distribution of DEMs of the Head House Area

Fig. 3.4 shows the elevation distribution of the eight available DEMs for the Head House area with elevation value on x axis and points proportion of all sampling points at each elevation on y axis.

Although all curves show a similar general pattern in trend of change and elevation range, differences exist, especially between those with different data sources. For example, both Ordnance Survey (OS) DEMs show a large variation in elevation distribution. For detailed analysis, elevation distribution was compared sorting by different resolutions and data sources.

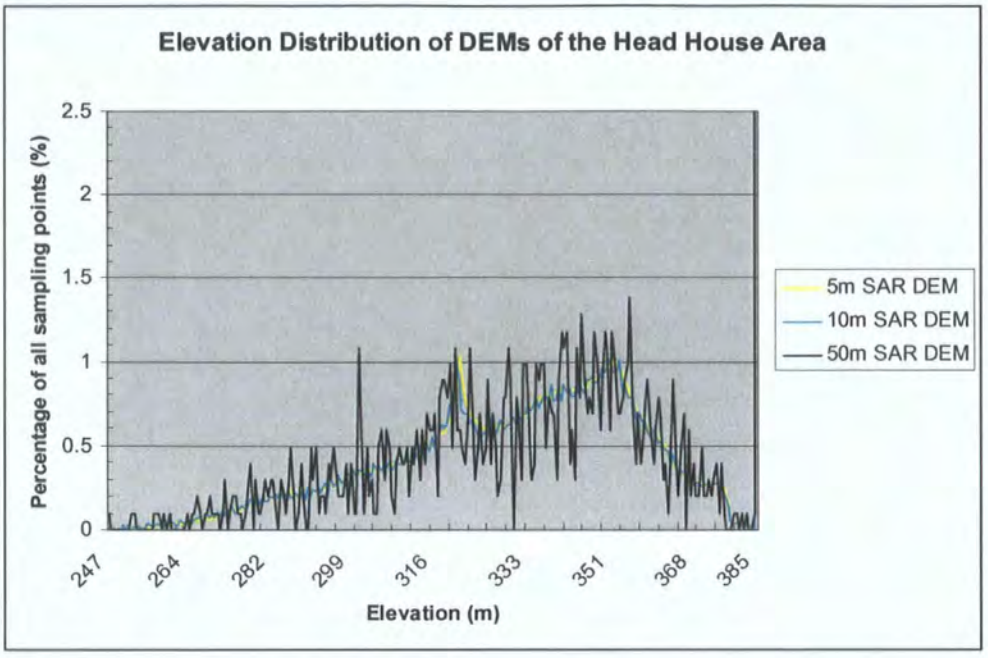

(a) SAR DEMs

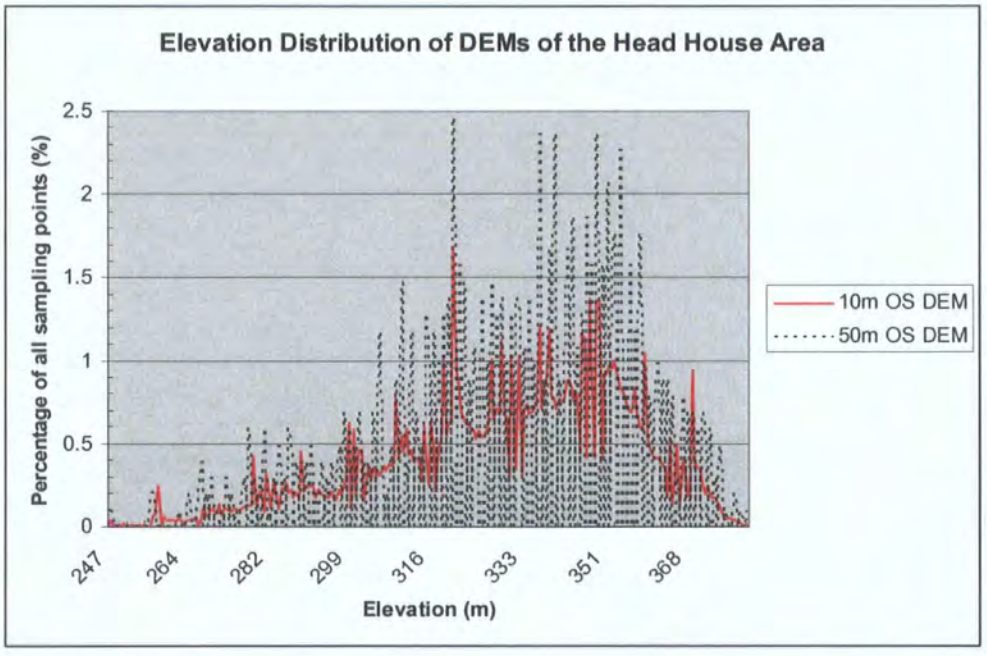

(b) OS DEMs

Figure 3.5 DEM elevation distribution comparison by different resolutions (1)

Fig. 3.5 compares elevation distributions from DEMs derived from interferometric radar (Fig. 3.5 (a)) and the data derived from the Ordnance Survey topographic maps (Fig. 3.5 (b)), respectively at different spatial posting with elevation as x-axis value and percentage of all sampling points as y-axis value.

DEMs produced from the same data source show different amount of variance in finer resolution DEM. However, the resolution increase from 10 m to 5 m in SAR DEMs has very limited impact on variance (Fig. 3.5 (a)).

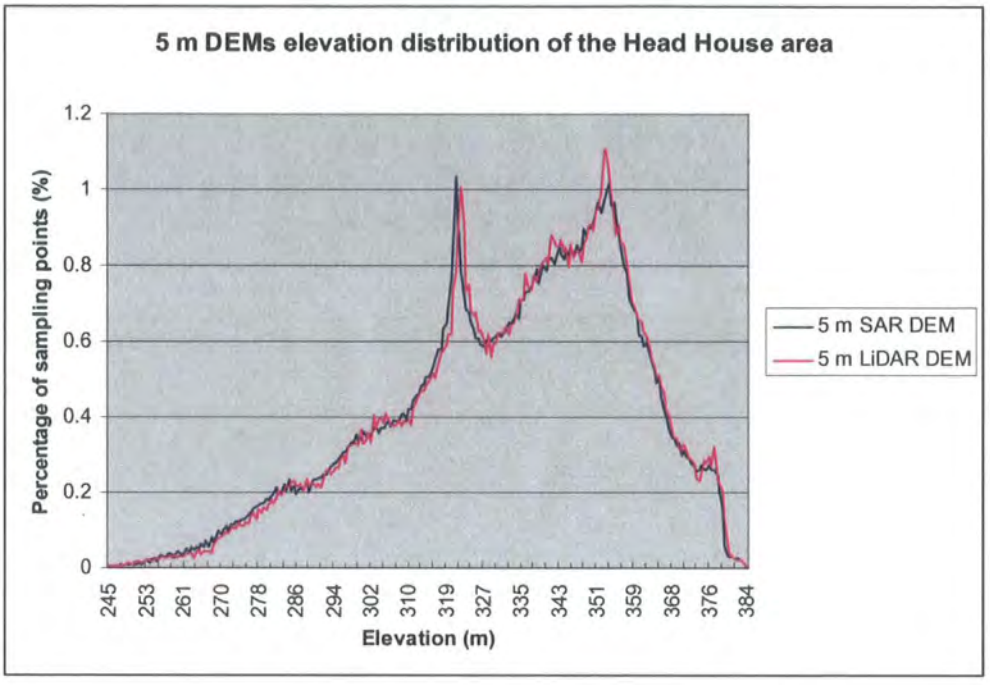

(a) 5 m DEMs

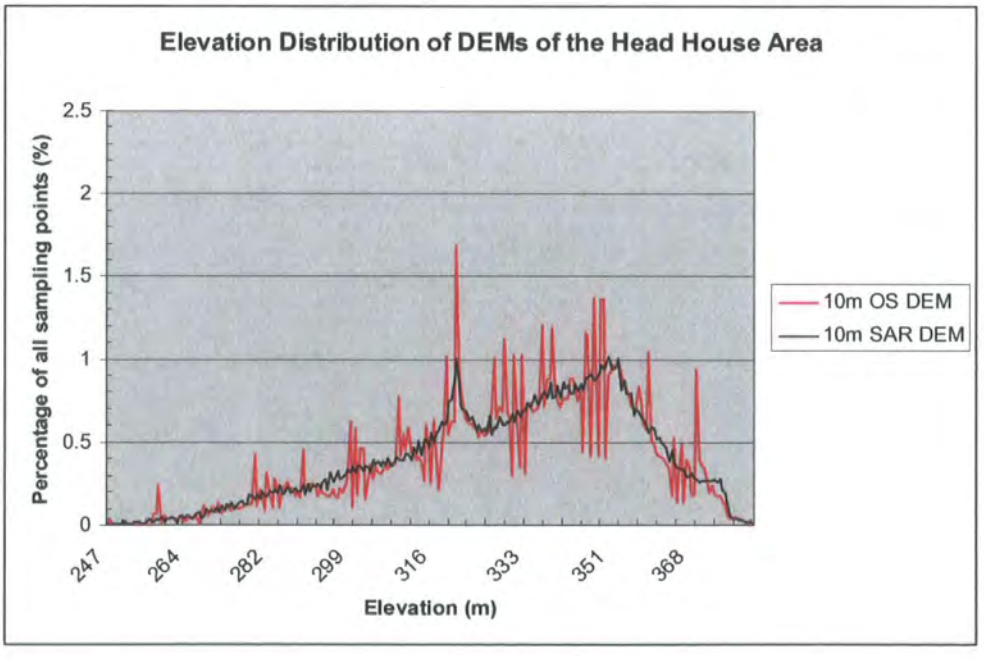

(b) 10 m DEMs

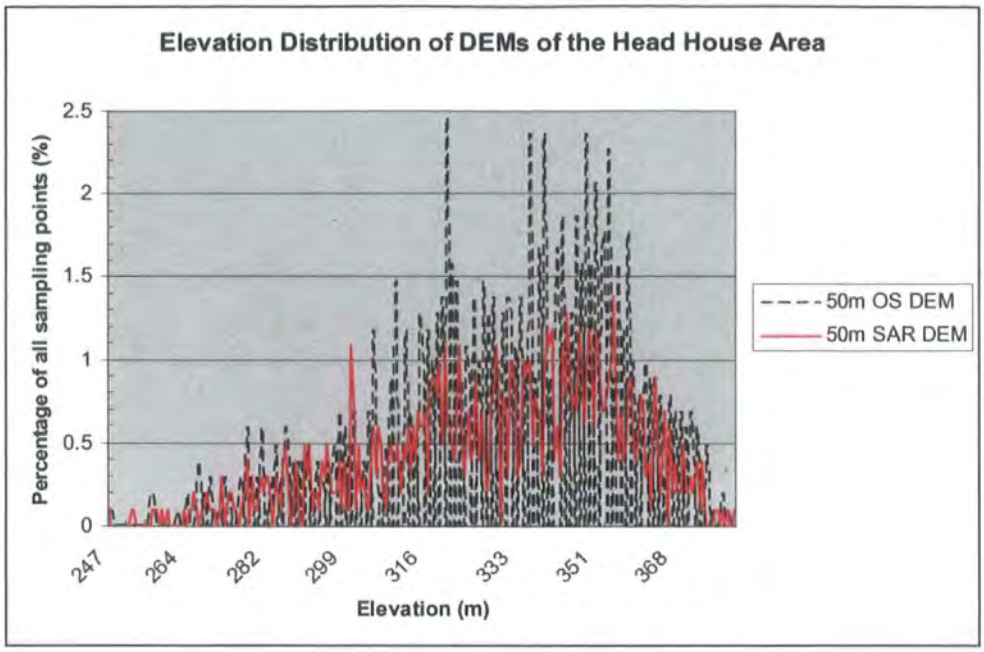

(c) 50 m DEMs

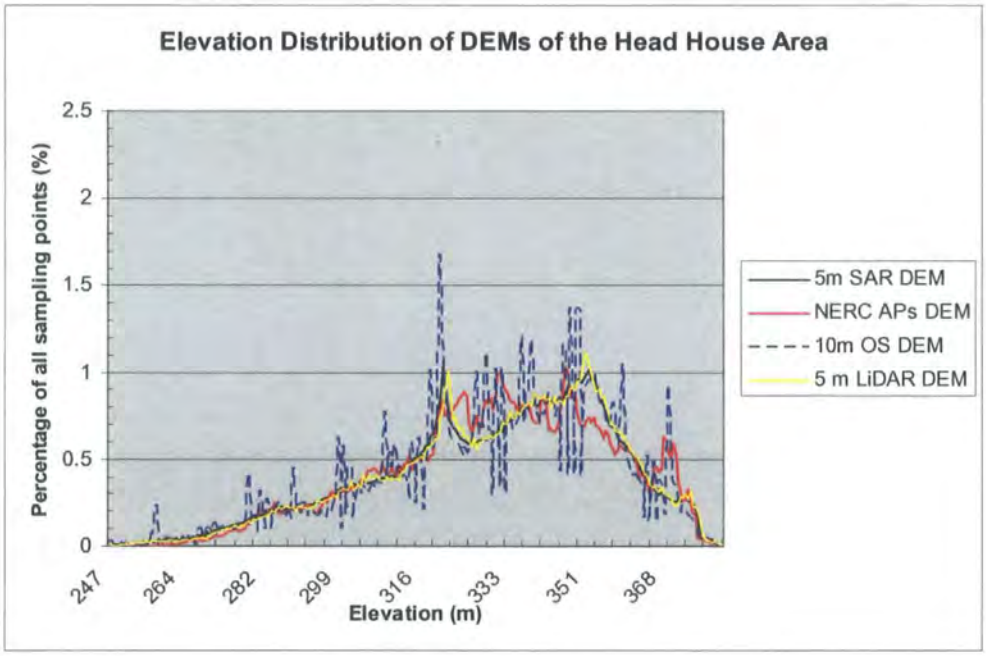

(d) Finest x-y resolution DEMs

Figure 3.6 DEM elevation distribution comparison with different data source (1)

Fig. 3.6 shows the differences among data sources in elevation distribution for the Head House area. Plots (a), (b) and (c) compare the 5 m, 10 m and 50 m DEMs respectively from the LiDAR data, OS data and SAR images. Plot (d) shows the difference between the finest resolution DEMs from all four data sources.

Plot (a) compares both 5 m resolution DEMs from the LiDAR and SAR data respectively. The SAR DEM shows a 2.2 m higher minimum elevation but 0.1° smaller standard deviation than the LiDAR DEM. In addition, both DEMs show a close agreement and have the same maximum and mean elevation values.

In plot (b), the mean elevations are 332.3 m and 333.3 m of the OS DEM and SAR DEM respectively. The median elevations are 336.1 m and 337.3 m respectively. The whole pattern looks similar with increase trends from the lowest elevation to about 325 m, where two DEMs both show the highest peak in histograms. Their second peaks are both shown at roughly 351 m in elevation. The amounts both decrease to zero afterwards. Two differences are shown in this image: One is that the DEM derived from the OS data receives one and a half time lager amount in both two peaks than the DEM derived from the SAR images does respectively. For example, 1% of points at around 324 m elevation is shown in the 10 m SAR DEM compared with 1.5% of points in the 10 m OS DEM.

In plot (c), the mean elevations are 332.5 m and 334.4 m of the OS DEM and SAR DEM respectively. The median elevations are 335.5 m and 338.2 m respectively. Their difference is larger than the one from the 10 m resolution DEMs. Like the image from the 10 m DEMs, the whole pattern looks similar with increase trend in histogram peaks, from the lowest elevation to about 325 m. Two 50 m DEMs show four or five peaks in the range of 340 m to 360 m. The SAR DEM shows a smoother pattern of elevation in histogram.

Comparing both DEMs from large scale aerial photographs, the DEM from the InfoTerra aerial photographs showed a relatively higher elevation in the Head House area overall. The mean elevations are 334.5 m and 331.8 m for the InfoTerra APs DEM and NERC aerial photographs DEM respectively. The median elevations are 336.8 m and 333.6 m respectively.

Results are consistent over the whole study area.

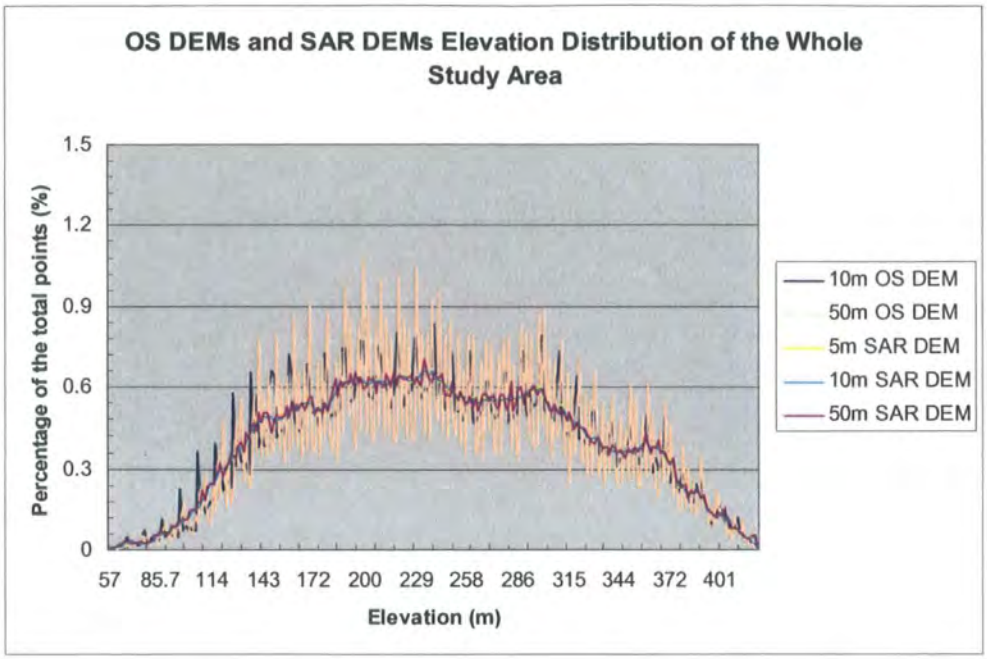

Figure 3.7 DEMs elevation distribution of the whole study area

Fig. 3.7 shows the whole pattern of DEM elevation distributions for the whole study area.

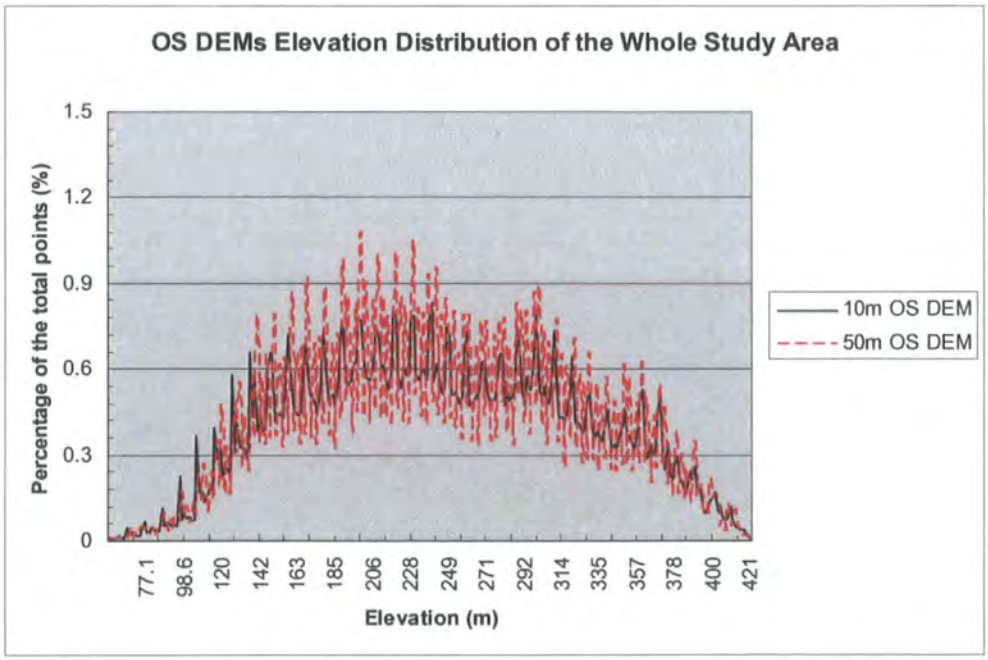

(a) OS DEMs

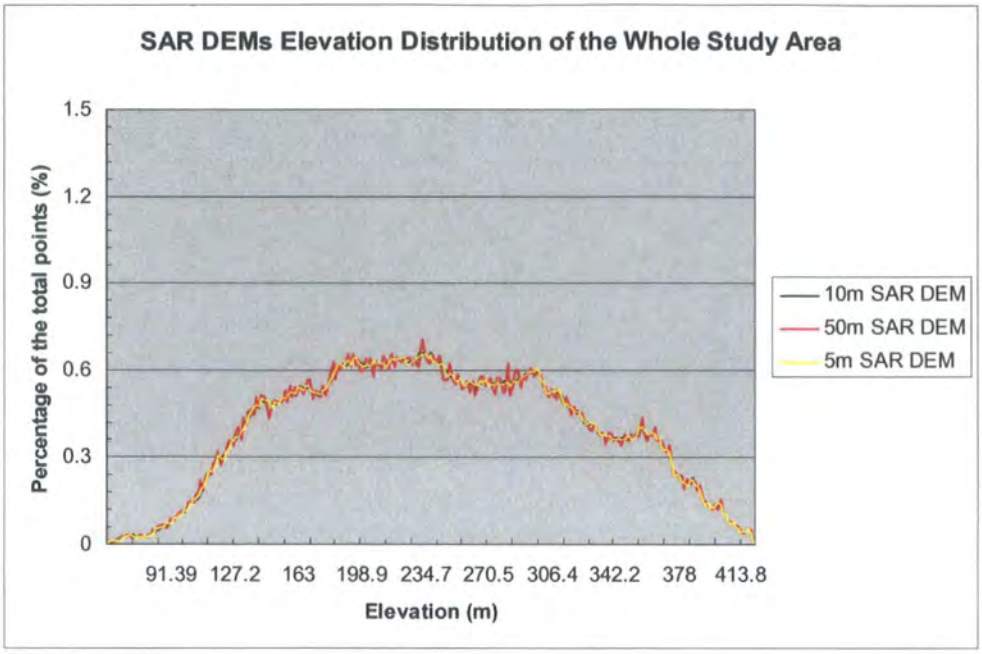

(b) SAR DEMs

Figure 3.8 DEM elevation distribution comparisons with different resolutions (2)

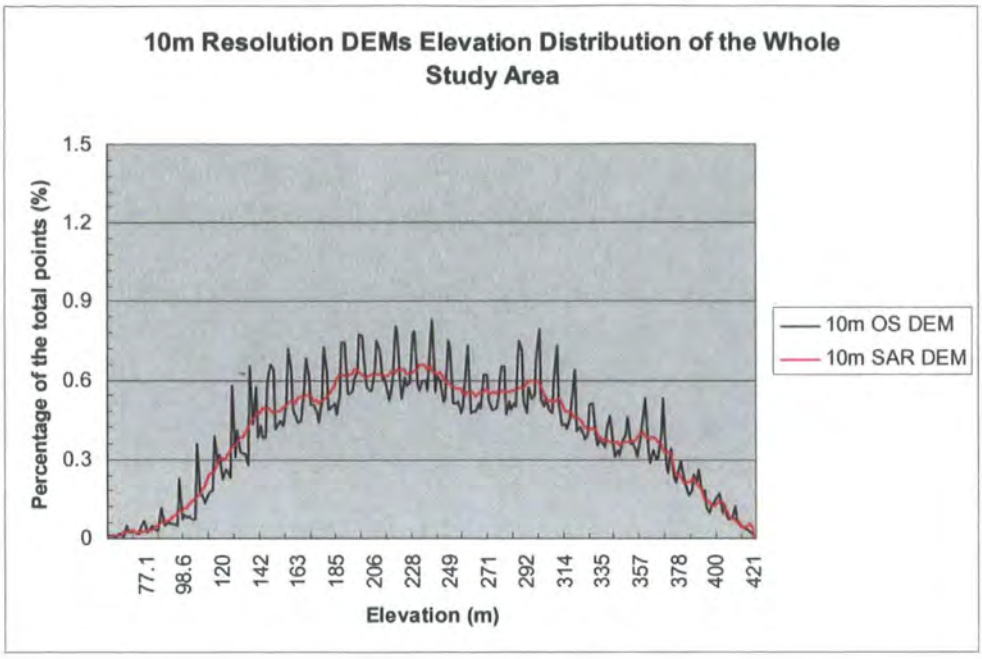

(a) 10 m DEMs

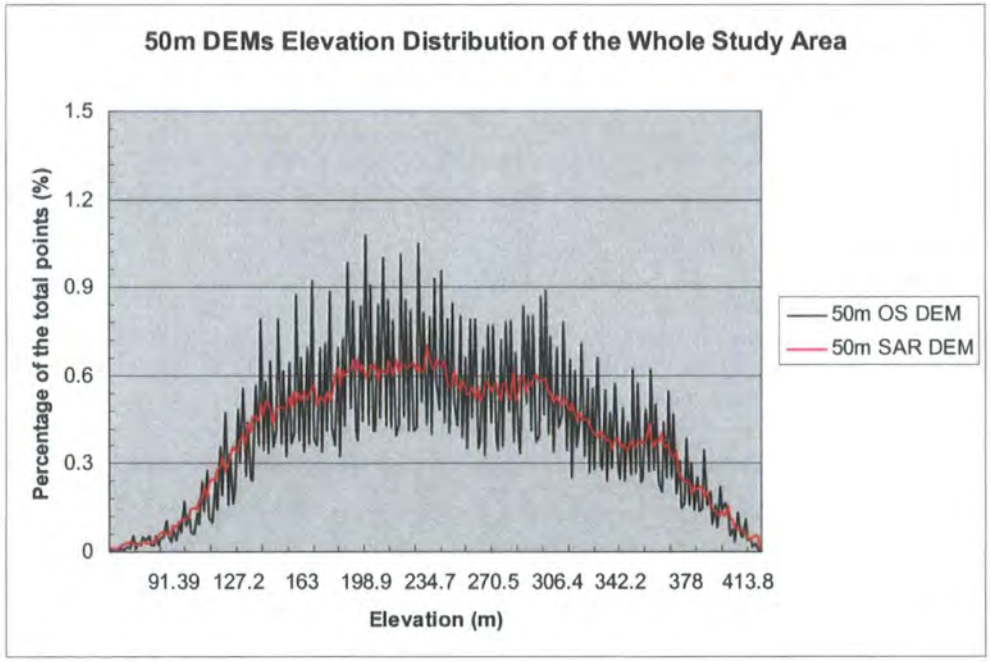

(b) 50 m DEMs

Figure 3.9 DEM elevation distribution comparison with different sources (2)

Fig. 3.8 and Fig. 3.9 show the difference between resolutions and data sources in elevation distribution for the same area.

At this larger geographical scale, DEMs at different resolutions tend to be more similar in terms of variation especially for the SAR DEMs at three resolutions.

In Fig. 3.9 (a), the mean elevations are 246.62 m and 246.94 m of the OS DEM and the SAR DEM respectively. The median elevations are 240.15 m and 243.12 m respectively. The two 10 m resolution DEMs have the same sample points in total and show similar distribution. Again, the one from OS data contains much aliasing.

In Fig. 3.9 (b), the mean elevations are 245.40 m and 246.67 m for the OS DEM and SAR DEM respectively. The median elevations are 241.88 m and 241.81 m respectively. They both show similar trends of change in elevation distribution and again the one from the OS data shows much aliasing in it.

Although the elevation distribution data have similar patterns for DEMs with the same resolution, the DEM pattern still needs to be compared and contrasted by different sources and different resolutions. Therefore cumulative probabilities were determined.

3.5.1.2. Cumulative Probability

The cumulative probability is calculated and shown for the Head House area and the whole study area separately.

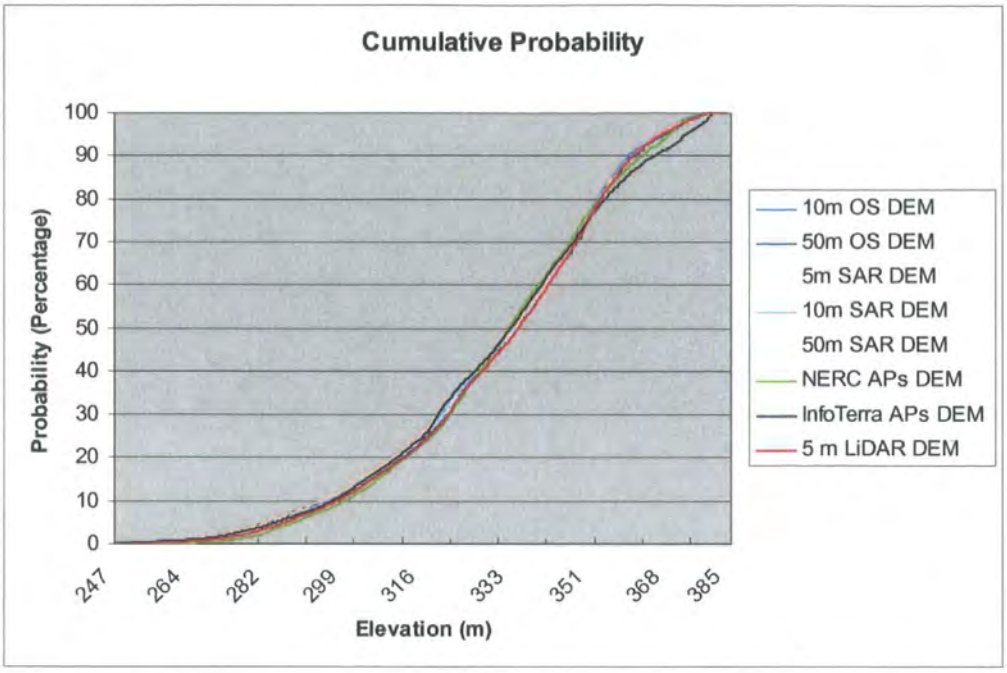

(a) the Head House area

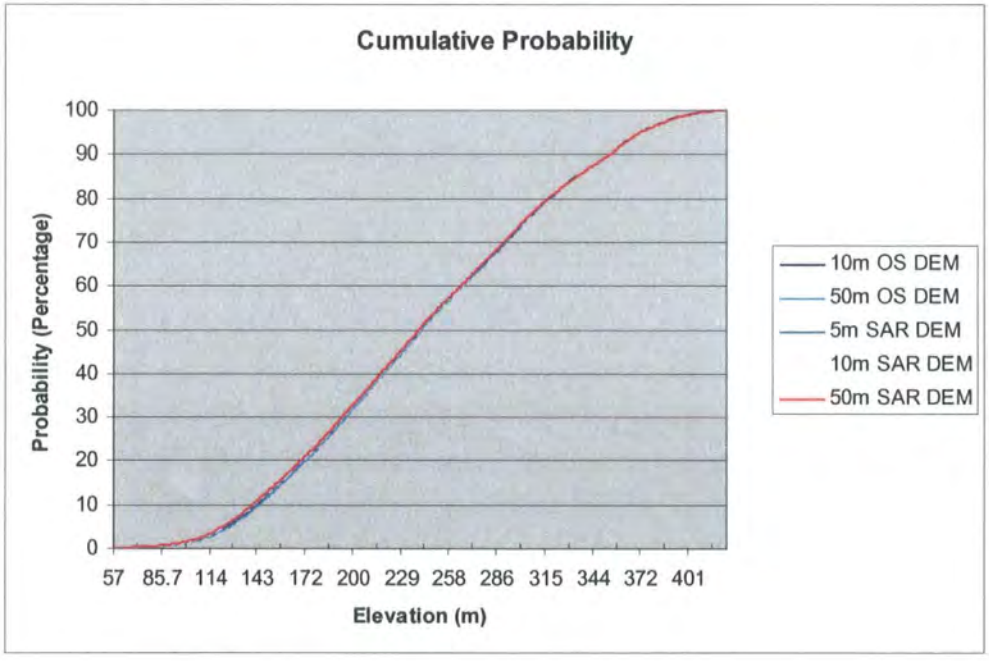

(b) the Whole study area

Figure 3.10 Cumulative probability in DEMs of the Head House Area (a) and the Whole study area (b)

Fig. 3.10 shows the cumulative probability for all available DEMs for both the Head House area and the whole study area.

The cumulative probability plots are very similar for all DEMs. Apart from which derived from the others, the DEM derived from the InfoTerra aerial photographs at higher altitude shows a difference in the Head House area.

Table 3.1 5% Percentile and 95% Percentile of Elevations for the Head House Area (1 digit precision)

Statistics / DEM	5% Percentile (m)	95% Percentile (m)
10 m OS DEM	367.0	283.5
50 m OS DEM	368.5	281.5
5 m SAR DEM	366.5	284.5
10 m SAR DEM	366.5	283.5
50 m SAR DEM	367.0	281.5
0.5 m NERC APs DEM	369.0	288.0
3 m InfoTerra APs DEM	372.0	284.0
5 m LiDAR DEM	369.0	284.0

Table 3.2 5% Percentile and 95% Percentile of Elevations for the Whole Study Area (1 digit precision)

Statistics / DEM	5% Percentile (m)	95% Percentile (m)
10 m OS DEM	373.0	125.5
50 m OS DEM	373.0	128.0
5 m SAR DEM	373.0	124.0
10 m SAR DEM	373.0	124.0
50 m SAR DEM	373.0	123.5

Table 3.1 and Table 3.2 summarise the 5% and 95% percentiles of elevations of each DEM for the Head House area and the whole study area in 1 digit precision. Extreme similarity can be noted for the whole study area.

3.5.1.3. Histograms

3.5.2. Slope

3.5.2.1. Statistical Analysis

Slope expressed in degrees from 0° to 90°, is a first order derivative of elevation. Table 3.3 summarises statistics from each set of slope calculations. Precision is set to one decimal place.

Table 3.3 Slope statistics in degrees

(a) 3×3 and 5×5 in the whole study area

DEM \ Statistics		Min	Max	Mean	Std. Dev.
10 m OS	3×3	0.0	52.5	7.8	±6.6
	5×5	0.0	46.6	7.6	±6.3
50 m OS	3×3	0.0	32.4	7.2	±5.4
	5×5	0.0	26.4	6.8	±4.8
5 m SAR	3×3	0.0	64.4	7.8	±6.5
	5×5	0.0	59.1	7.7	±6.3
10 m SAR	3×3	0.0	56.4	7.7	±6.3
	5×5	0.0	46.4	7.5	±6.0
50 m SAR	3×3	0.0	32.3	7.1	±5.4
	5×5	0.0	26.7	6.6	±4.8

(b) in the Head House area

DEM	Min	Max	Mean	Std. Dev.
10 m OS	0.0	88.5	7.6	±1.4
10 m SAR	0.1	88.5	7.4	±1.3
5 m SAR	0.0	37.7	6.3	±0.5
50 m OS	0.6	21.4	5.9	±0.4
50 m SAR	0.5	18.6	5.8	±0.3
0.5 m NERC Aerial photographs	0.0	88.0	9.4	±1.3
3 m InfoTerra Aerial photographs	0.0	67.2	7.5	±0.8
5 m LiDAR	0.0	47.2	6.8	±0.9

Table 3.3 summarises statistics for slope, where Table 3.3 (a) describes those results calculated with both 3 by 3 windows and 5 by 5 windows from the DEMs covering the whole study area as shown in Fig. 2.4 using the ENVI 4.1 software. Table 3.3 (b)

lists statistics calculated only using a 3 by 3 window from the Head House area using the SAGA software package. Since slope was calculated after filling the depressions/pits, almost all results show the minimum value as zero.

In Table 3.3 (a), all DEMs have mean slope values of no larger than 7.8°, which indicates that the whole study area is relatively flat. The maximum slope varies from approximately 27° to 65°, where significantly different representation of surface from different DEMs can be seen.

In Table 3.3 (b), slope statistics from different DEMs vary more significantly. For instance, the maximum slope varies from 18.6° in the 50 m resolution SAR DEM to 88.5° in the 10 m resolution SAR DEM. The DEM derived from the NERC aerial photographs shows a much larger mean slope as 9.4°. It is notable that DEMs with the same resolution give similar results. For example, the 5 m SAR DEM and the 5 m LiDAR DEM show only 9.6°, 0.4° and ±0.4° in the maximum, mean slope and standard deviation respectively.

The larger window size (5×5) calculates a more generalised slope. From all slope results, both maximum values and mean values are smaller using a 5 by 5 window image than using 3 by 3. The 'real' slope is smoothed by a 5 by 5 window, so that standard deviation becomes smaller.

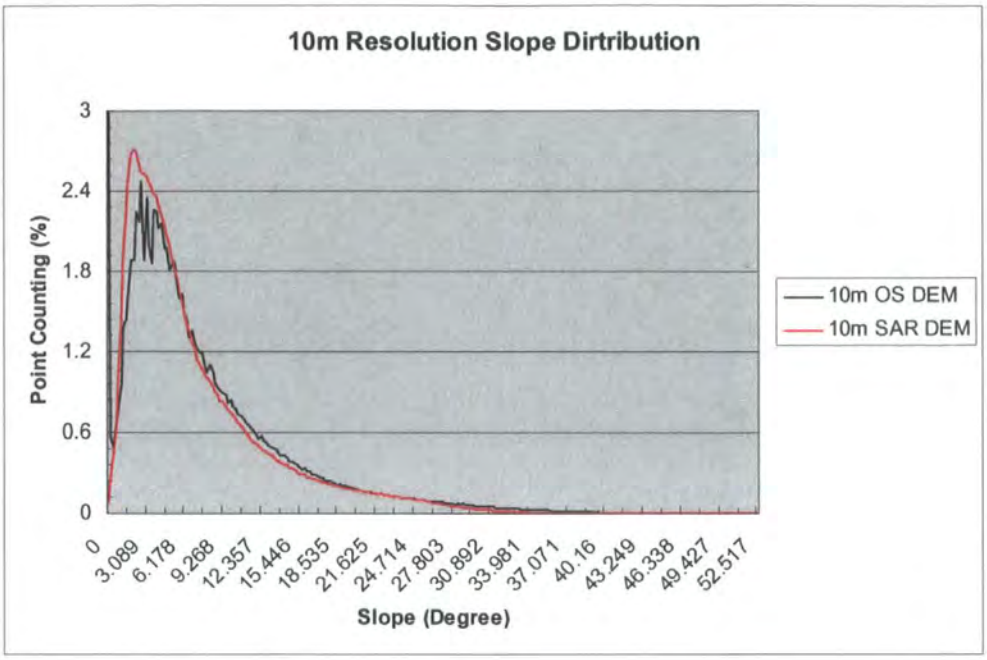

(a) Slope distribution of 10 m resolution DEMs

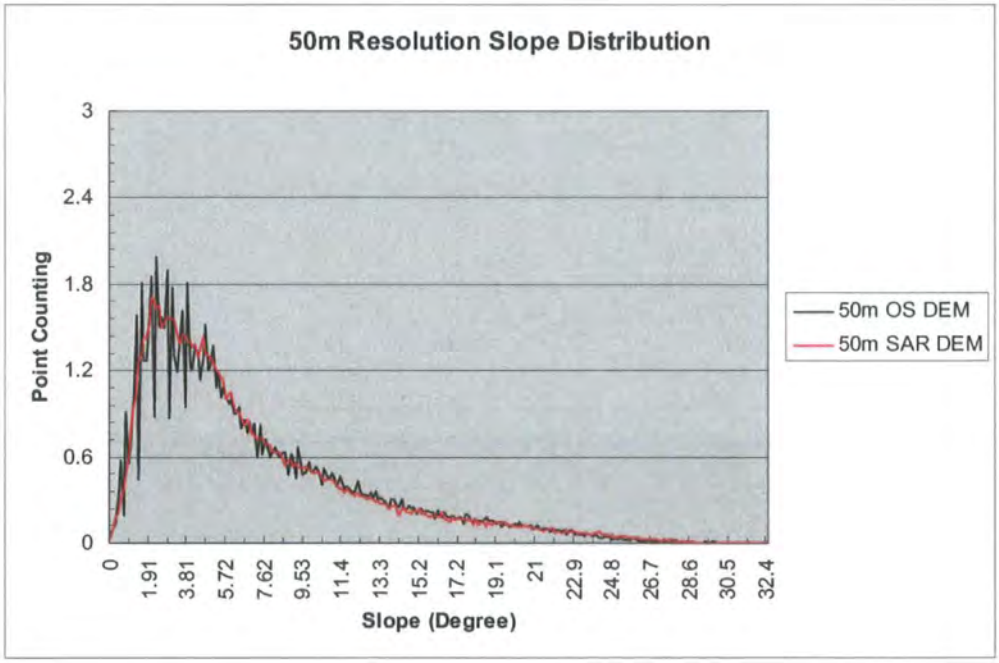

(b) Slope distribution of 50 m DEMs

Figure 3.12 Slope distribution comparisons from different data sources of the whole study area

Fig. 3.12 shows the slope distribution from both 10 m and 50 m resolution DEMs derived from the Ordnance Survey contour maps and SAR data of the whole study area.

In plot (a), the mean slopes are 7.8° and 7.7° for the OS DEM and SAR DEM respectively. The standard deviations are ±6.6° and ±6.3° respectively. They both show similar patterns in slope distribution with a peak at around 4.0°. The one from the SAR images shows more smoothed curve than the one from the OS data.

The mean slopes are 7.2° and 7.1° for the OS DEM and SAR DEM respectively. The standard deviations are both ±5.4°. Although they both show a similar pattern of slope distribution, the peak is at around 20.0° slope area, which is much larger than the one shown in Fig. 3.12. Again, the distribution of slopes from the SAR data shows a smooth pattern compared to the OS data.

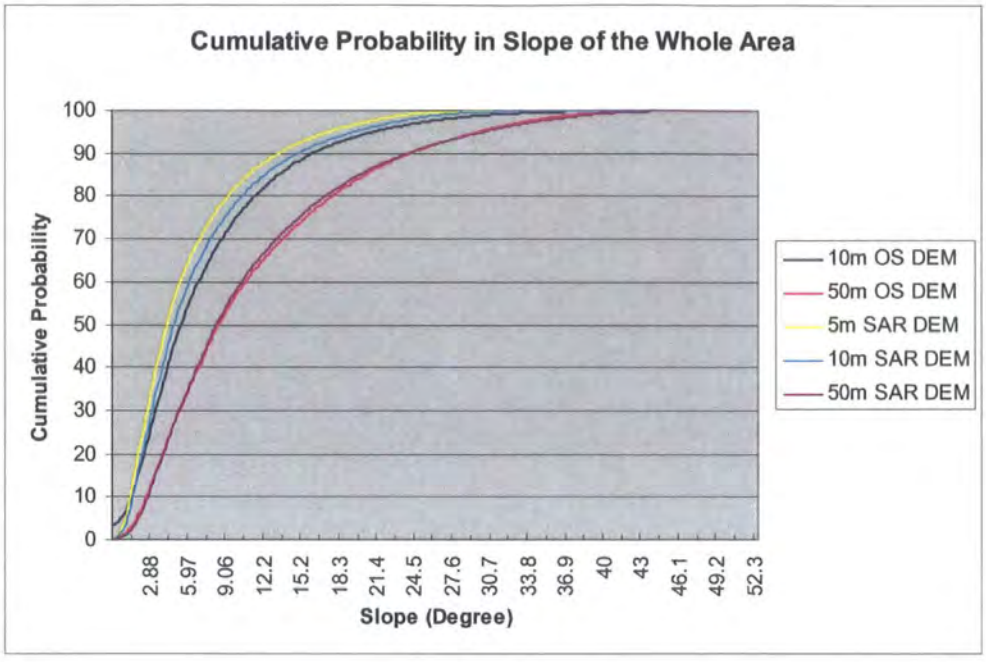

(a) the Whole Study area

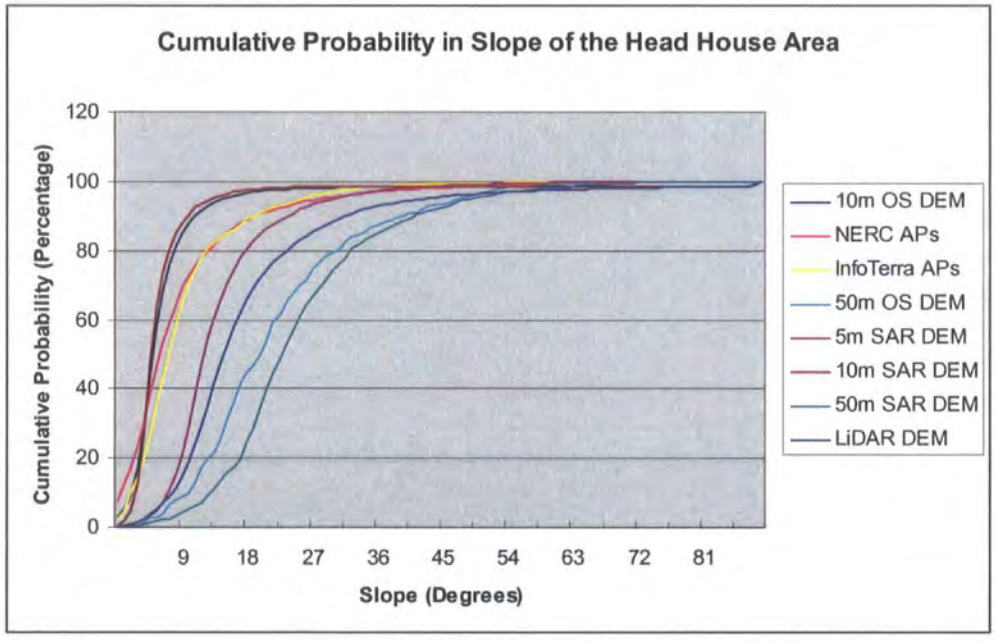

(b) the Head House area

Figure 3.13 Cumulative probability of slope of the whole study area (a) and the Head House area (b)

Fig. 3.13 shows the cumulative probability plots for slope for both study areas.

In plot (a), five DEMs are compared. Although all DEMs show similar patterns of cumulative probability, the two OS DEMs show a lower cumulative probability value for low slope angle compared with the DEMs from the SAR data. In terms of

resolution, higher resolution DEMs give higher cumulative probability values for low slope angles. In summary, the cumulative probability curve data shows a pattern where the DEMs are ordered as: 5 m SAR DEM; 10 m SAR DEM; 50 m SAR DEM; 10 m OS DEM; and 50m OS DEM.

In plot (b), significant differences exist among these DEMs. The cumulative probability increases most quickly in the 10 m SAR DEM followed by the 10 m OS DEM. Both DEMs derived from aerial photographs show almost the same trend in cumulative probability, followed by the 5 m SAR DEM closely. Both DEMs at 50 m resolution increase the most slowly. Overall, both DEMs from aerial photographs, the 5 m and 10 m SAR DEMs and the 10 m OS DEMs reach 100% almost the same at 40.0° area, and both DEMs at 50 m resolution turn to be much later at around 65.0° area.

3.5.2.2. Slope Difference Comparison

Slope maps were compared to investigate the data source and DEM resolution impact on slope calculation in terms of difference interpretation.

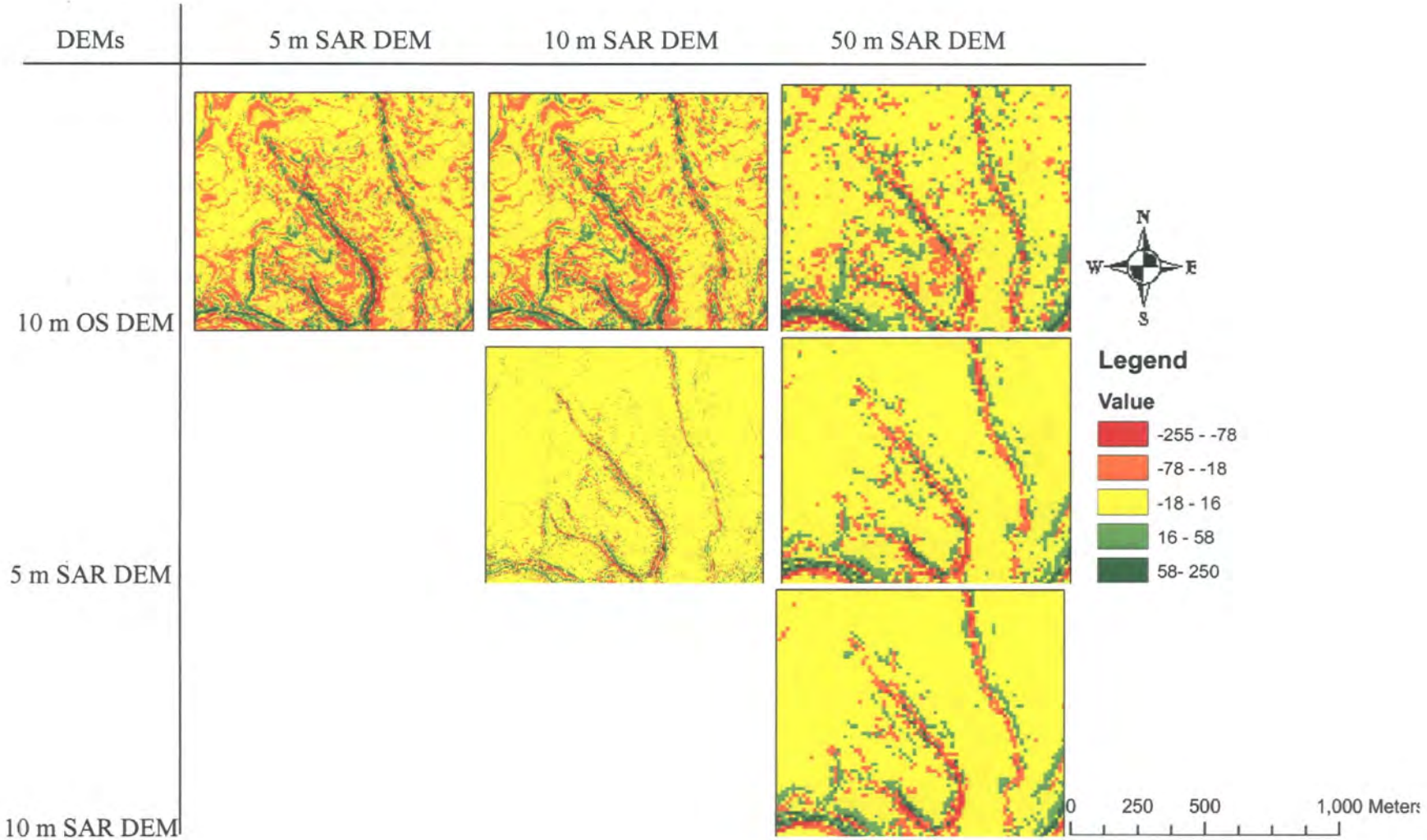

Figure 3.14 Difference maps in slope from OS DEMs and SAR DEMs

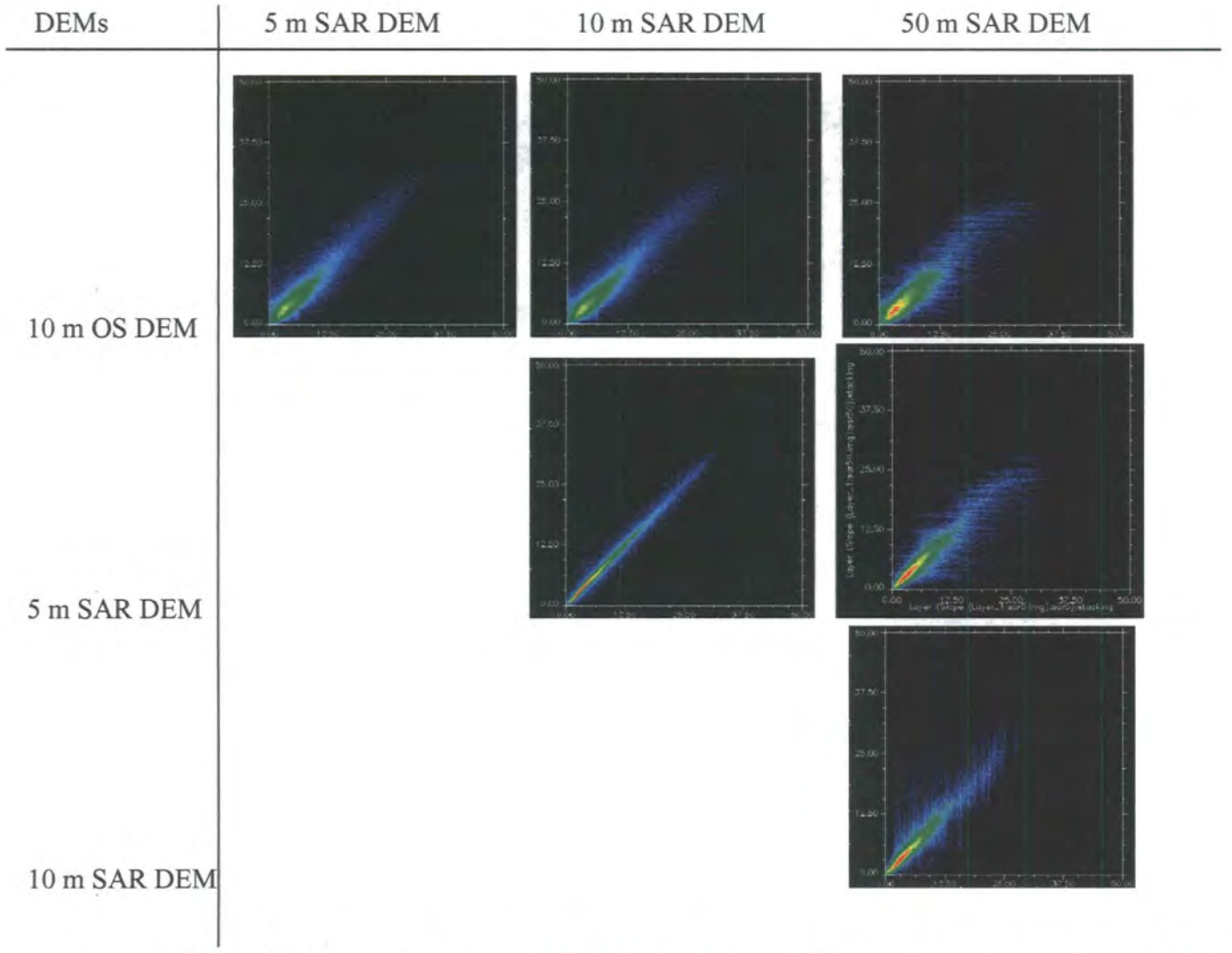

Figure 3.15 Scatter plots of the slope calculated from 10 m OS DEM and 5 m, 10 m, and 50 m resolution SAR DEMs of the whole study area

Fig. 3.14 shows a matrix of difference maps in slope from the 10 m resolution OS DEM comparing the 5 m, 10 m, and 50 m resolution SAR DEMs for a 1×1 km sampling area.

The red and green areas represent the locations with large difference in slope between two DEMs, and the yellow area represents agreement between the two DEMs.

Using the ENVI basic tools module, two dimensional (2D) scatter plots were generated as shown above. The scatter plot density distribution is colour coded using a rainbow colour table from purple to red with purple indicating low density.

Fig. 3.15 shows the scatter plots of slope between each two DEMs from the OS data and SAR images.

Only the scatter plot between SAR DEMs shows high agreement as the red part and the comparison between the 5 m and 10 m SAR DEM shows the least variation. No large difference is noticed in the comparison between the 10 m OS DEM and any of the SAR DEMs.

In addition, Table 3.4 summarises the mean of difference in slope from the SAR DEMs. It shows that differences within SAR series DEMs are very limited, almost within 1.0° in slope in all cases. The only exception lies in the difference between the 5 m SAR DEM and the 50 m SAR DEM with a 5 by 5 window size.

Table 3.4 Mean slope difference in degrees from SAR series DEMs

DEMs / Window size	10 m and 5 m	50 m and 10 m	50 m and 5 m
3 by 3	-0.1	-0.6	-0.7
5 by 5	-0.2	-0.9	-1.1

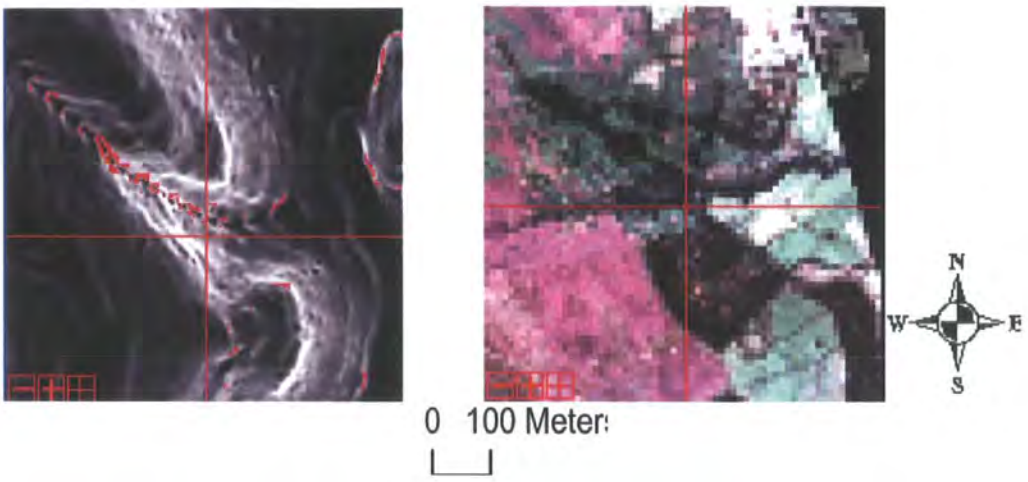

(a) Slope Difference in the 10 m OS DEM and the 50 m SAR DEM of a small outcrops area

(b) a NERC 1:15 000 aerial photograph of a small outcrops area

Figure 3.16 Slope difference in outcrops of resistant strata

Fig. 3.16 (b) shows the location on NERC 1:15 000 aerial photographs where slope is different between the 10 m OS DEM and the 50 m SAR DEM. The red cross in each small image directs the same geographical location. The combination of horizontal and vertical axis represents the image attribute. For example, the image in the first row and the first column represents the difference area between the 5 m SAR DEM and the 10 m OS DEM. These images show that the majority of differences in slope in these DEMs are in the river channels.

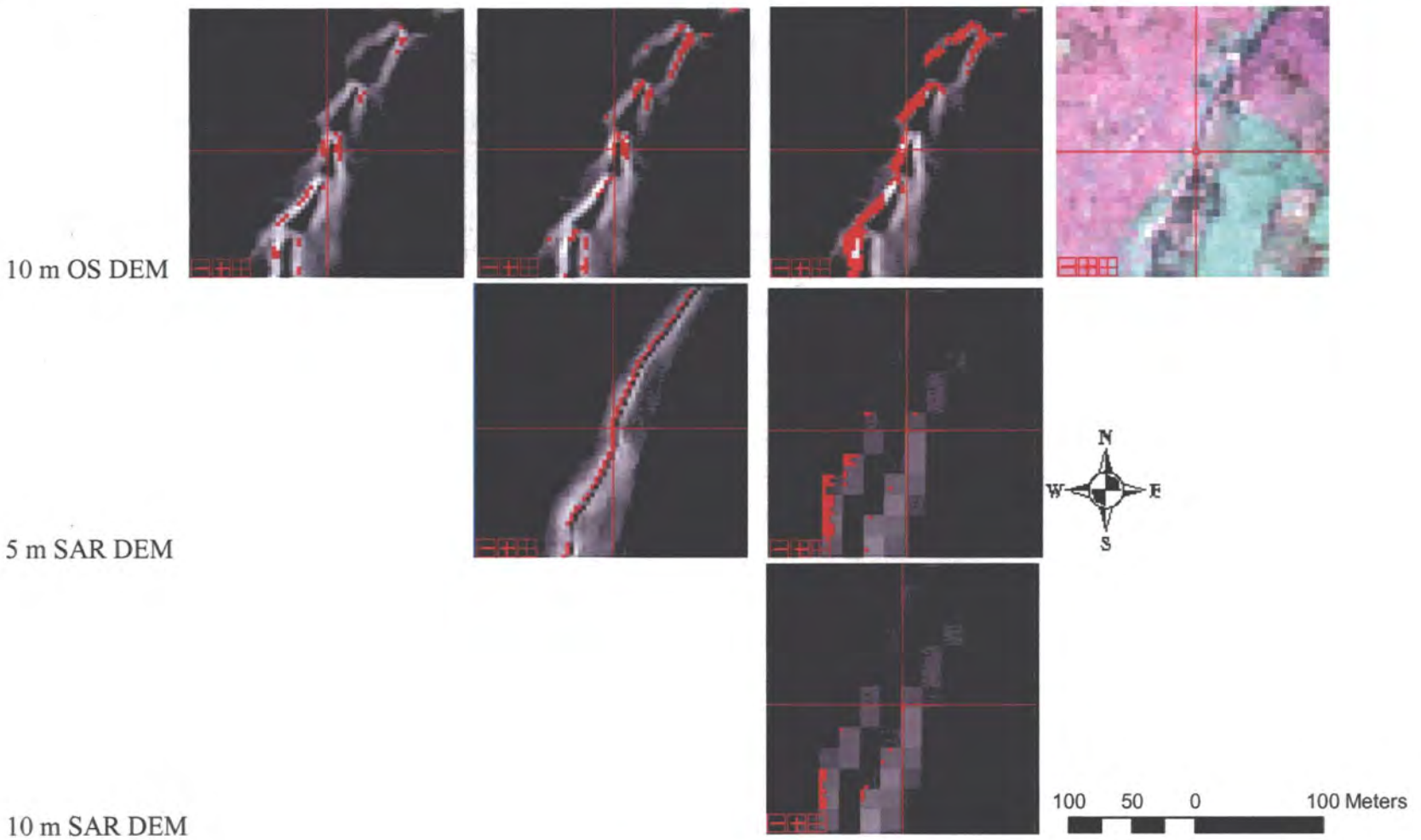

Figure 3.17 Slope differences from OS DEM and SAR DEMs

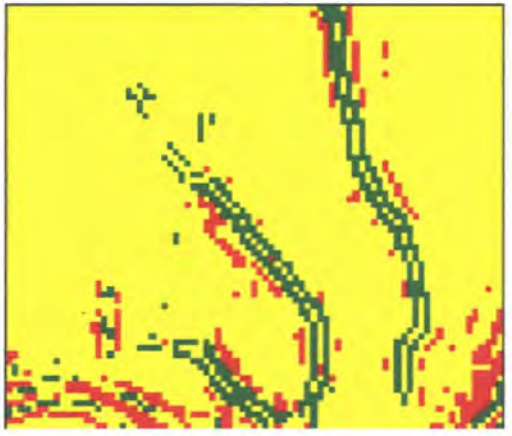

(a) 50 m SAR DEM

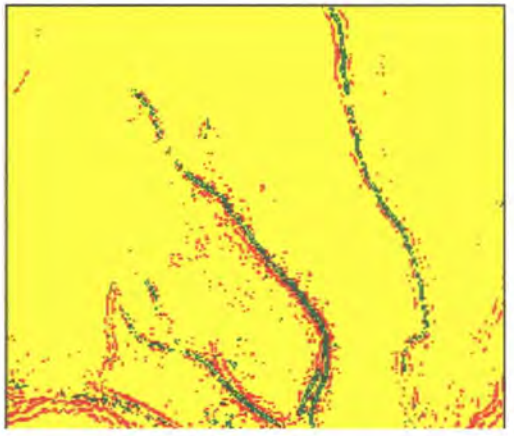

(b) 10 m SAR DEM

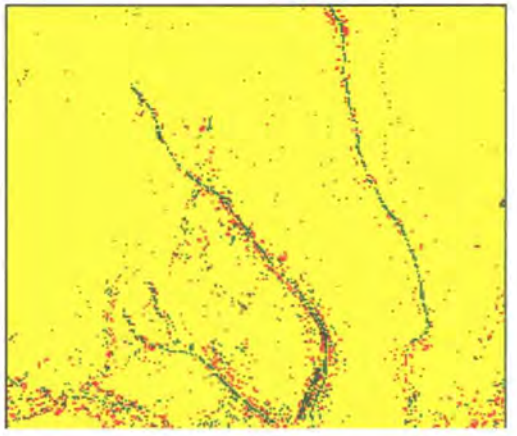

(c) 5 m SAR DEM

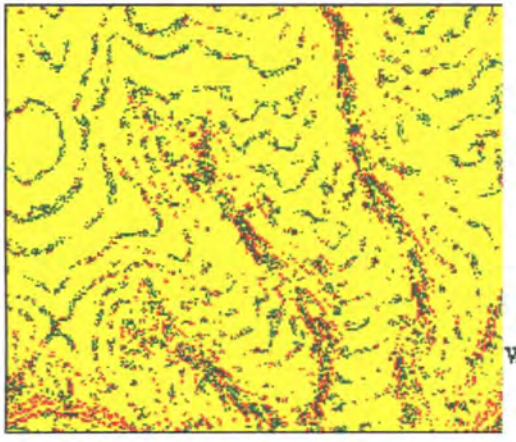

(d) 10 m OS DEM

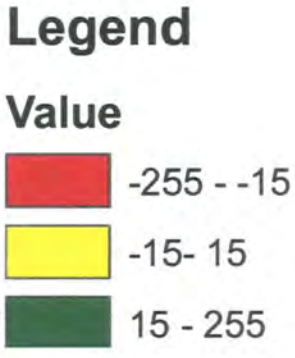

Figure 3.18 Kernel size impact on slope difference

Fig. 3.17 shows there are differences in break of slope along small outcrops of resistant strata. This kind of difference is only seen when comparing two DEMs from OS contour maps and SAR images.

Fig. 3.18 shows the effect of kernel size changing from 3×3 to 5×5. Images were generated using the minus function in the Arc/GIS. The difference value was rescaled to -255 to 255.

The red area means that the slope is smaller by using a 3×3 window than a 5×5 window. All the four images show differences in the area of river channels. Besides these differences, the image from the 10 m OS DEM shows another kind of difference along the contour lines, where slope is larger by using the smaller kernel window than the larger window.

3.5.2.3. Algorithm Comparison

Parameters that were compared are presented in Table 3.5 without filling depressions in the original LiDAR DEM.

Table 3.5 summarises the differences between the results from the ENVI 4.2, Arc/GIS and SAGA software packages for calculating slopes for the Head House area. Red colour highlights the largest difference and the black colour means the smallest difference in the three results from each tested DEM.

The SAGA, using the algorithm in Zeverbergen and Thorne (1987), calculated slopes with the smallest standard deviations. Also, this algorithm tended to derive larger maximum slopes, with the only exception being the DEM generated from 1:6 000 NERC aerial photographs.

Table 3.5 Comparison of ENVI 4.1, Arc/GIS, and SAGA slope results in the Head House Area

Statistics / DEM	Min			Max		
	ENVI	Arc/GIS	SAGA	ENVI	Arc/GIS	SAGA
3 m InfoTerra Aerial photographs	0.0	0.0	0.0	70.1	71.0	74.5
0.5 m NERC 1:6 000 Aerial photographs	0.0	0.1	0.0	87.2	90.0	88.0
5 m InSAR	0.0	0.0	0.0	36.4	36.6	37.7
10 m InSAR	0.1	0.1	0.1	87.0	27.9	88.5
50 m InSAR	0.1	0.2	0.5	13.9	14.4	18.6
10 m OS	0.0	0.0	0.0	87.0	34.5	88.5
50 m OS	0.4	0.4	0.6	15.5	16.1	21.4
5 m LiDAR	0.0	0.1	0.0	47.2	48.3	49.7

Statistics / DEM	Mean			Std. Dev.		
	ENVI	Arc/GIS	SAGA	ENVI	Arc/GIS	SAGA
3 m InfoTerra Aerial photographs	7.5	7.5	7.7	±6.0	±6.1	±0.8
0.5 m NERC 1:6 000 Aerial photographs	10.8	27.3	10.9	±11.6	±17.0	±1.6
5 m InSAR	6.3	6.3	6.3	±3.4	±3.4	±0.5
10 m InSAR	7.3	6.2	7.4	±10.1	±3.2	±1.3
50 m InSAR	5.4	5.4	5.8	±2.2	±2.2	±0.3
10 m OS	7.5	6.3	7.6	±10.3	±3.9	±1.4
50 m OS	5.6	5.5	5.9	±2.5	±2.6	±0.4
5 m LiDAR	6.8	6.7	6.8	±4.8	±4.6	±0.6

3.5.3. Aspect

Aspect expressed in degrees, is another first order derivative of elevation and represents the slope direction from facing north clockwise. An aspect image not only gives us details of slope direction but also an overview of topography of the research location. Aspect was calculated with both 3×3 window and 5×5 window using the ENVI 4.1 software.

3.5.3.1. Statistical Analysis

Table 3.6 Aspect statistics in degrees

(a) in the Whole Study Area

DEM \ Statistics		Min.	Max.	Mean	Std. Dev.
10 m OS	3×3	0.0	360.0	171.4	±85.2
	5×5	0.0	360.0	170.2	±85.0
50 m OS	3×3	0.4	360.0	168.9	±83.9
	5×5	0.1	360.0	167.9	±83.3
5 m SAR	3×3	0.0	360.0	169.9	±84.9
	5×5	0.0	360.0	169.7	±84.7
10 m SAR	3×3	0.0	360.0	169.6	±84.6
	5×5	0.0	360.0	169.4	±84.4
50 m SAR	3×3	0.0	360.0	168.8	±83.7
	5×5	0.0	360.0	168.4	±83.1

(b) in the Head House Area

DEM \ Statistics		Min.	Max.	Mean	Std. Dev.
3 m InfoTerra Aerial photographs	3×3	0.0	360.0	215.9	±72.4
	5×5	0.0	360.0	217.4	±70.8
0.5 m NERC 1:6 000 Aerial photographs	3×3	0.0	360.0	203.6	±86.4
	5×5	0.0	360.0	203.8	±86.1
10 m OS	3×3	0.0	360.0	213.9	±70.0
	5×5	0.0	357.6	213.5	±69.6
50 m OS	3×3	8.1	347.5	216.5	±65.8
	5×5	61.7	351.0	217.2	±63.2
5 m SAR	3×3	0.5	359.3	217.1	±66.6
	5×5	3.5	360.0	217.1	±66.3
10 m SAR	3×3	7.1	357.7	215.1	±67.5
	5×5	5.1	354.9	213.8	±67.8
50 m SAR	3×3	58.7	328.7	219.4	±64.2
	5×5	103.3	323.8	219.7	±61.8
5 m LiDAR	3×3	2.9	360.0	213.8	±67.4
	5×5	1.3	360.0	216.5	±67.3

Table 3.6 describes the aspect statistics to one decimal place, where part (a) gives the results from the larger area and part (b) provides the information from the Head House area.

In Table 3.6 (a), the results are quite similar in all fields. Mean value varies from c. 167.9° to c. 171.4°. Standard deviation varies from ±83.1° to ±85.2°. By comparing the two sizes of windows in use, the larger window leads to a smaller maximum, mean and standard deviation in all cases.

Table 3.6 (b) shows more differences among those DEMs of the Head House area. The minimum and maximum aspect increases and decreases significantly, respectively along with either the decrease in DEM resolution or the increase in window size. For example, the two red values in Table 3.6 (b) show that 50 m

resolution with a 5×5 window size generalises the surface with the minimum aspect to c. 103.3° in the 50 m SAR DEM compared the result using 3×3 windows as 58.7°.

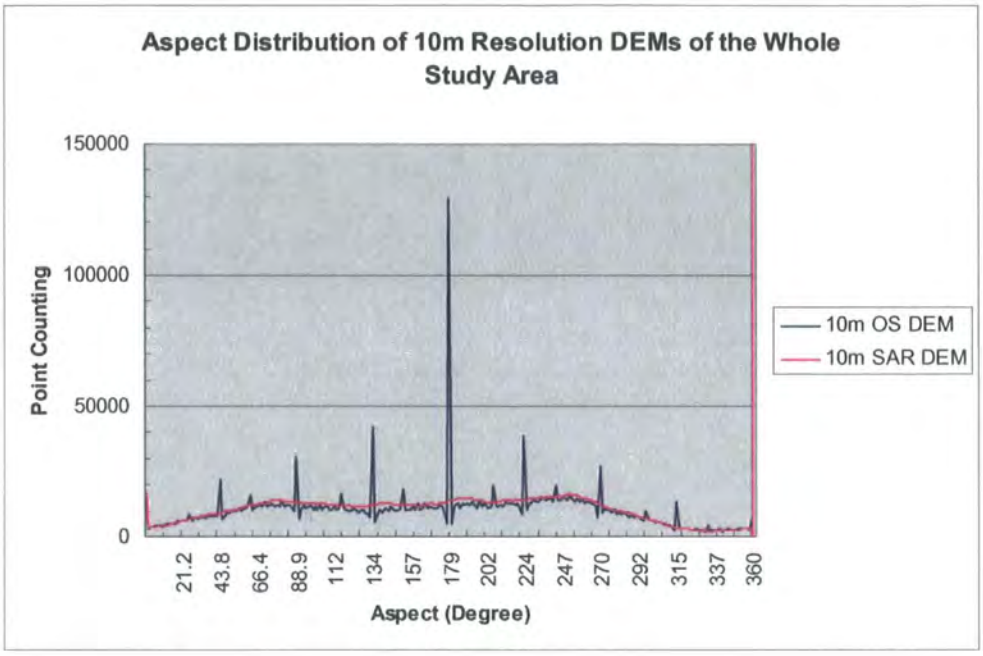

(a) 10 m DEMs

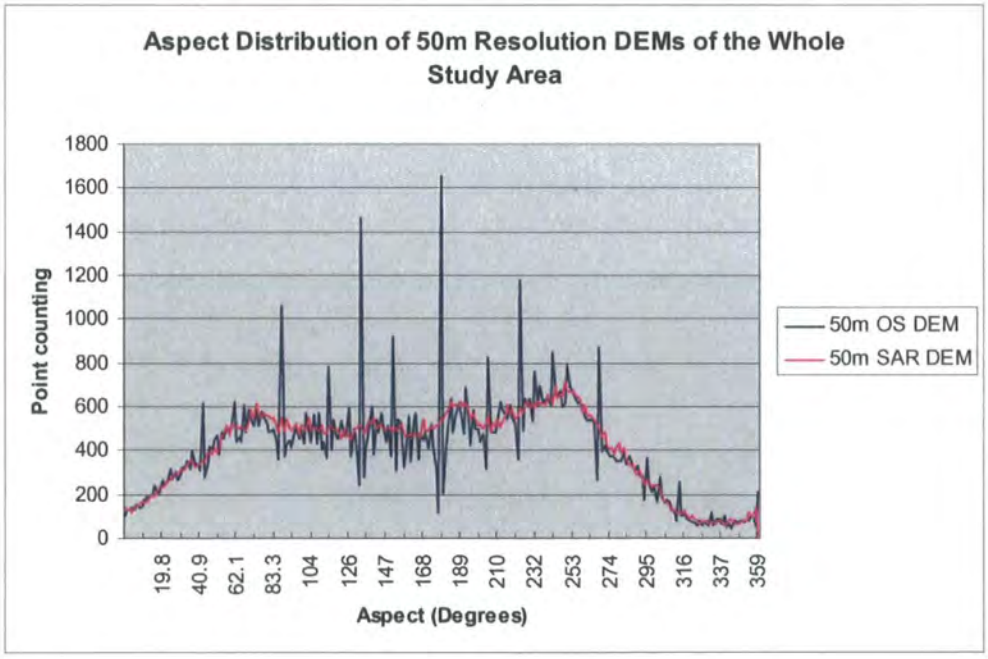

(b) 50 m DEMs

Figure 3.19 Aspect distribution of DEMs of the whole study area

Fig. 3.19 (a) and Fig. 3.19 (b) show the aspect distribution of 10 m resolution and 50 m resolution DEMs respectively for the whole study area.

In plot (a), the mean aspects are 213.9° and 215.1° for the OS DEM and the SAR DEM respectively. Their standard deviations are 70.0° and 67.5° respectively. Both DEMs show median values of aspect at around 180.0°. Compared to the line from the OS contour maps, the one from the SAR DEM shows a much smoother distribution. In addition, the former one shows significant difference with a space about 44.0° and with the highest peak at about 180.0°. The latter finding may be caused by an edge effect. Due to the overall point amounts, compared aspect distributions are sorted by DEM resolution to give a better representation.

In plot (b), the mean aspects are 216.5° and 219.4° for the OS DEM and the SAR DEM respectively. Their standard deviations are 65.8° and 64.2 respectively. Similar to the comparison from the 10 m DEMs, both distributions show the same patterns excluding several peaks in the 10 m OS DEM.

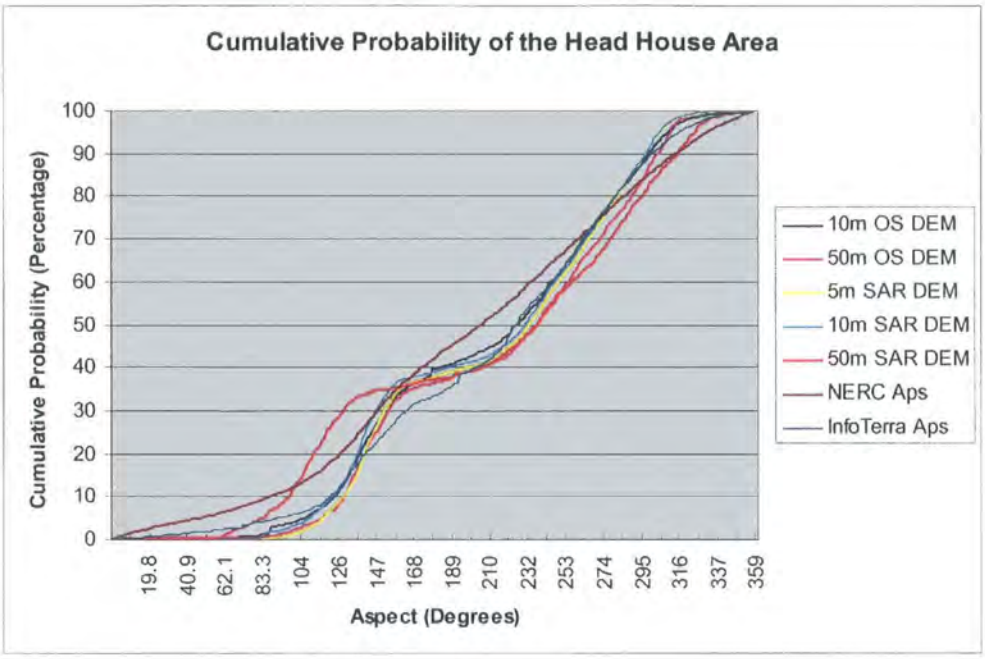

(a) the Head House area

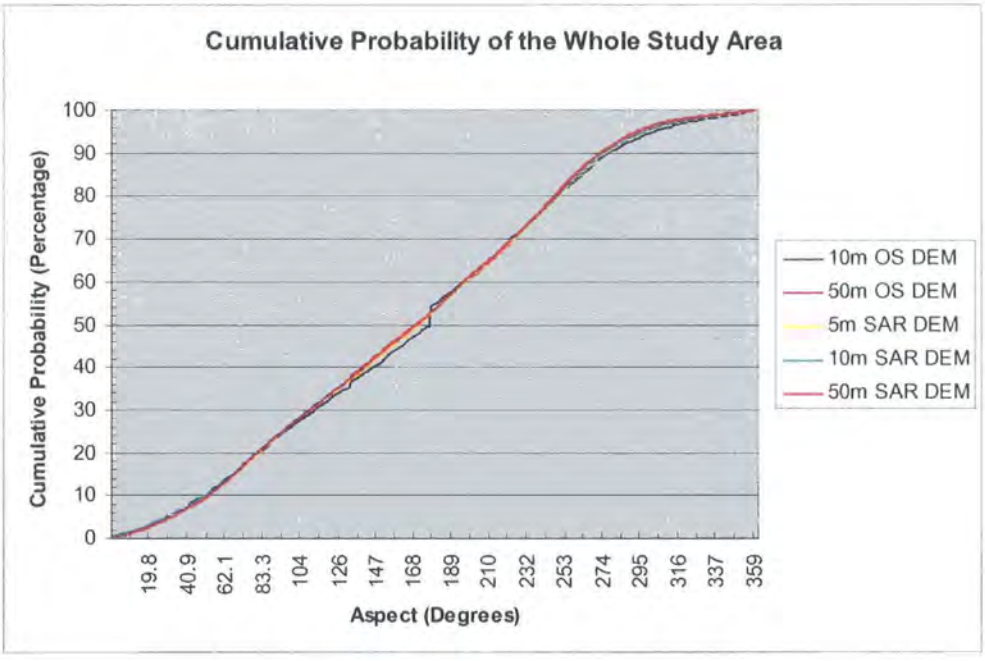

(b) Whole Study area

Figure 3.20 Cumulative probability of aspect of the Head House area (a) and the whole study area (b)

Fig. 3.20 shows the cumulative probability in aspect for DEMs in both study areas

This figure shows that all these five DEMs produce very close cumulative probabilities in aspect for the whole study area. Only minor difference can be noticed

among the cumulative probability lines. Excluding the 50 m InSAR DEM and the one derived from the NERC 1:6 000 aerial photographs, all DEMs show similar patterns of cumulative probability for the Head House area. The one from the 50 m SAR DEM shows an increase at around 130.0° area and the one from NERC 1:6 000 aerial photographs shows slightly different patterns in cumulative probability. The curve from the 10 m OS DEM shows a similar (cf. Fig.3.19) significant increase in number of pixels for an aspect of 180°.

Table 3.7 5% Percentile and 95% Percentile of the Aspects in the Head House Area

Statistics / DEM	5% Percentiles	95% Percentiles
10 m OS DEM	311.0	106.0
50 m OS DEM	303.0	119.0
5 m InSAR DEM	306.0	118.0
10 m InSAR DEM	305.0	115.0
50 m InSAR DEM	303.0	120.5
0.5 m NERC APs DEM	332.5	49.0
3 m InfoTerra APs DEM	317.0	92.0

Table 3.8 5% Percentile and 95% Percentile of the Aspects in the Whole Study Area

Statistics / DEM	5% Percentiles	95% Percentiles
10 m OS DEM	304.0	31.0
50 m OS DEM	296.0	34.0
5 m InSAR DEM	300.0	33.0
10 m InSAR DEM	298.5	31.0
50 m InSAR DEM	295.0	33.0

Table 3.7 and Table 3.8 summarise the 5% percentiles and 95% percentiles of the aspects from each DEM for both Head House area and the whole study area in one

decimal place. In Table 3.7, DEMs derived from aerial photographs have much smaller 95% percentiles than others and all OS and SAR DEMs have similar statistics in both areas.

3.5.3.2. Aspect Visualisation

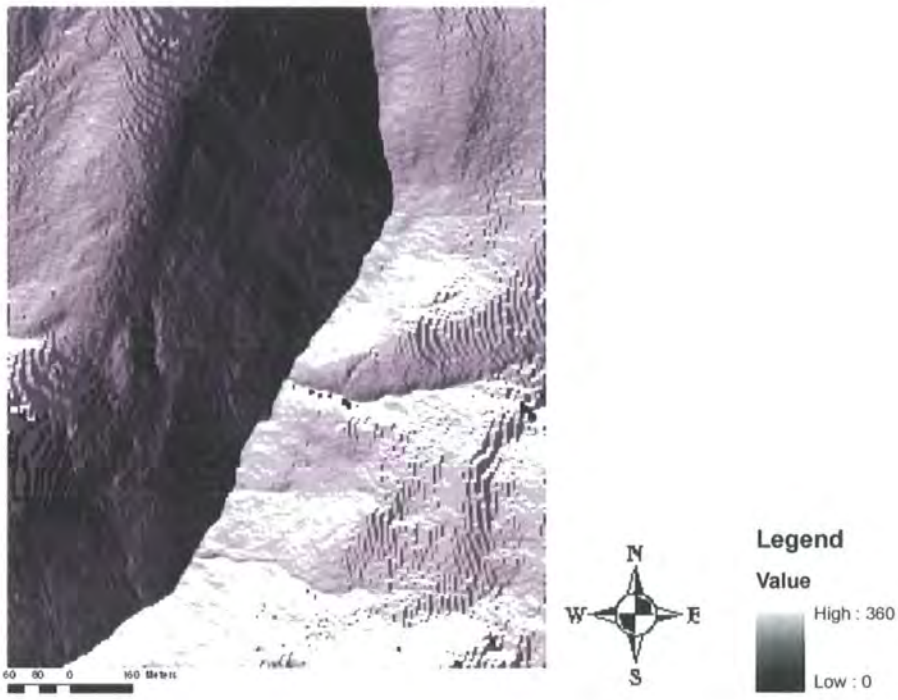

Figure 3.21Aspect image of the original 5 m LiDAR DEM

Fig. 3.21 shows a visualised aspect image from the original LiDAR DEM of the Head House area using the SAGA. The DEM shows that LiDAR data provide more details in topographic representation such as the wrinkle shape feature in the Head House stream.

(a) 5 m InSAR DEM (b) 10 m InSAR DEM (c) 50 m InSAR DEM

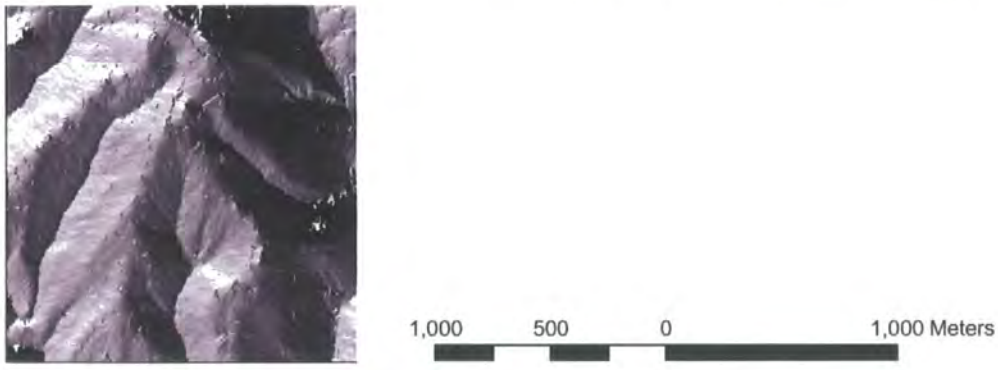

(d) 10 m OS DEM

Figure 3.22 Aspect visulisation

Fig. 3.22 compares the visualised aspect in a group, from all InSAR DEMs and the 10 m OS DEM in an area of c. 1.3 km^2 using the Arc/GIS. The aspect images from the 5 m and 10 m InSAR DEMs offer vivid demonstrations of surface geomorphology. Surface features, such as river channels and streams can be easily identified. River channels are shown as thin lines between the areas of two opposite directions of slopes in these images. The one from the 10 m OS DEM also shows the local surface clearly. The aspect image from the 50 m resolution InSAR DEM shows a smoother surface than the other three.

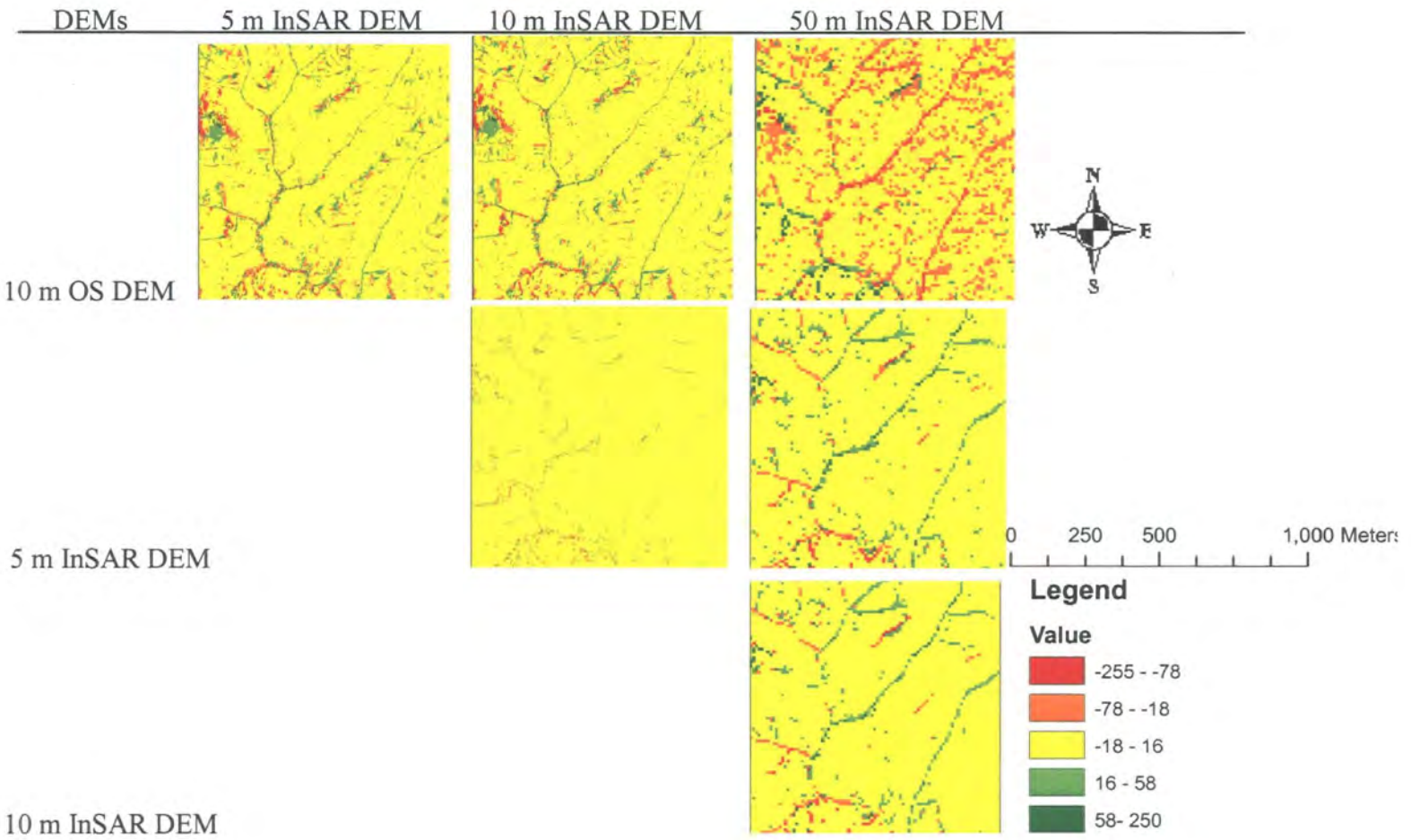

Figure 3.23 Difference maps of aspect from OS DEMs and InSAR DEMs

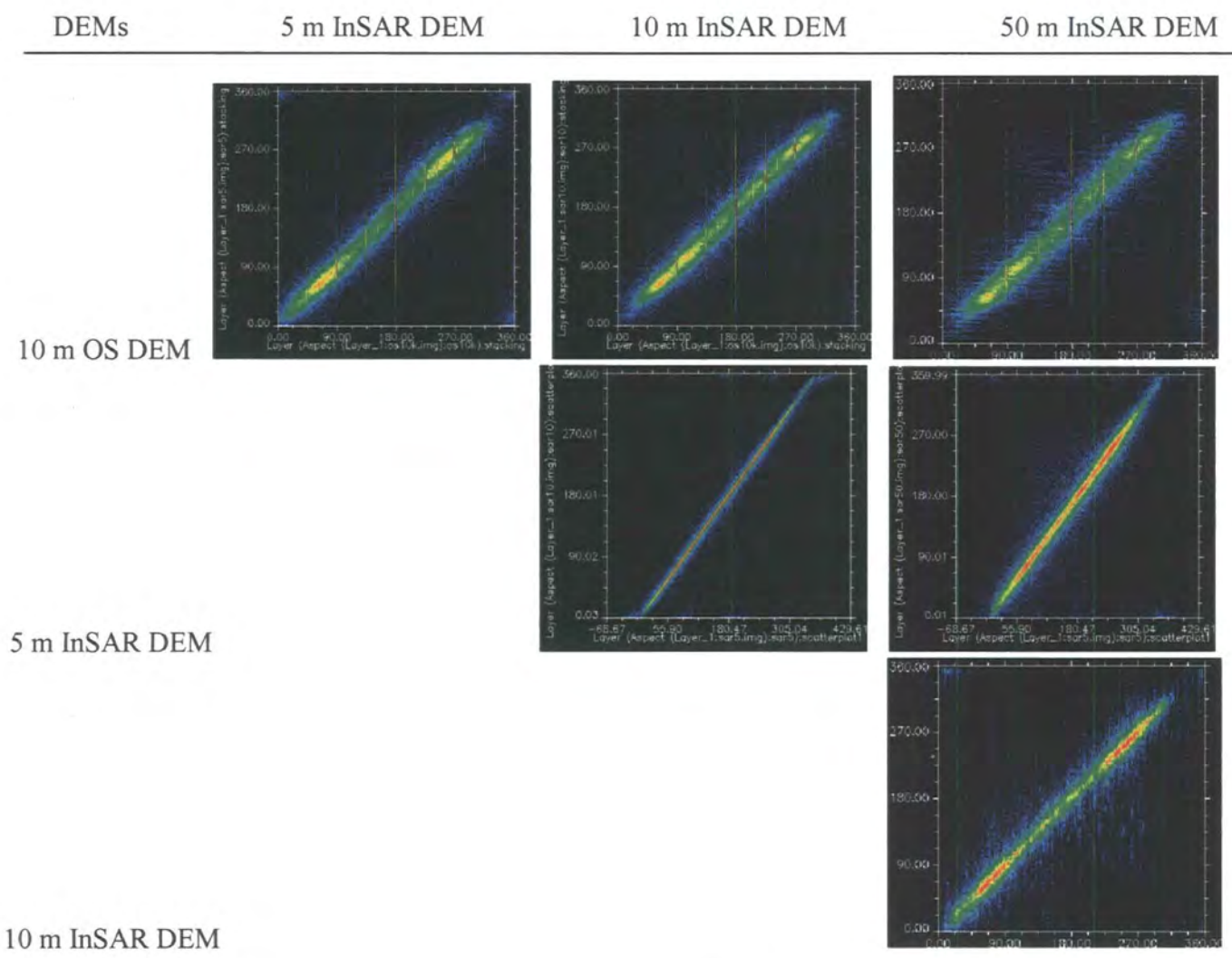

Figure 3.24 Aspect 2D scatter plots

3.5.3.3. Aspect Difference Comparison

Fig. 3.23 shows a matrix of difference maps in aspect from the 10 m resolution OS DEM and all three InSAR DEMs in an area of about 0.54 km^2. They all were calculated using the Arc/GIS.

Overall, differences between the 10 m OS DEM and any of the InSAR DEMs are larger than the difference between any two InSAR DEMs. A coarser resolution of InSAR DEM produces a larger difference with the OS DEM. The 5 m and 10 m resolution InSAR DEMs are most similar in value among all the DEMs, and there are no big differences when comparing the 10 m OS DEM to the 50 m resolution InSAR DEM.

Fig. 3.24 shows the 2D scatter plots of aspect between the 10 m OS DEM and InSAR DEMs for the whole study area. It shows that the 5 m and 10 m resolution InSAR DEMs have the fewest differences and hence the scatter plot in comparison of 10 m and 50 m resolution InSAR DEMs is extremely similar to the one of the 5 m and 50 m resolution DEMs. No big difference exists in the comparison of the 10 m OS DEM and any of InSAR DEMs.

3.5.3.4. Algorithm Comparison

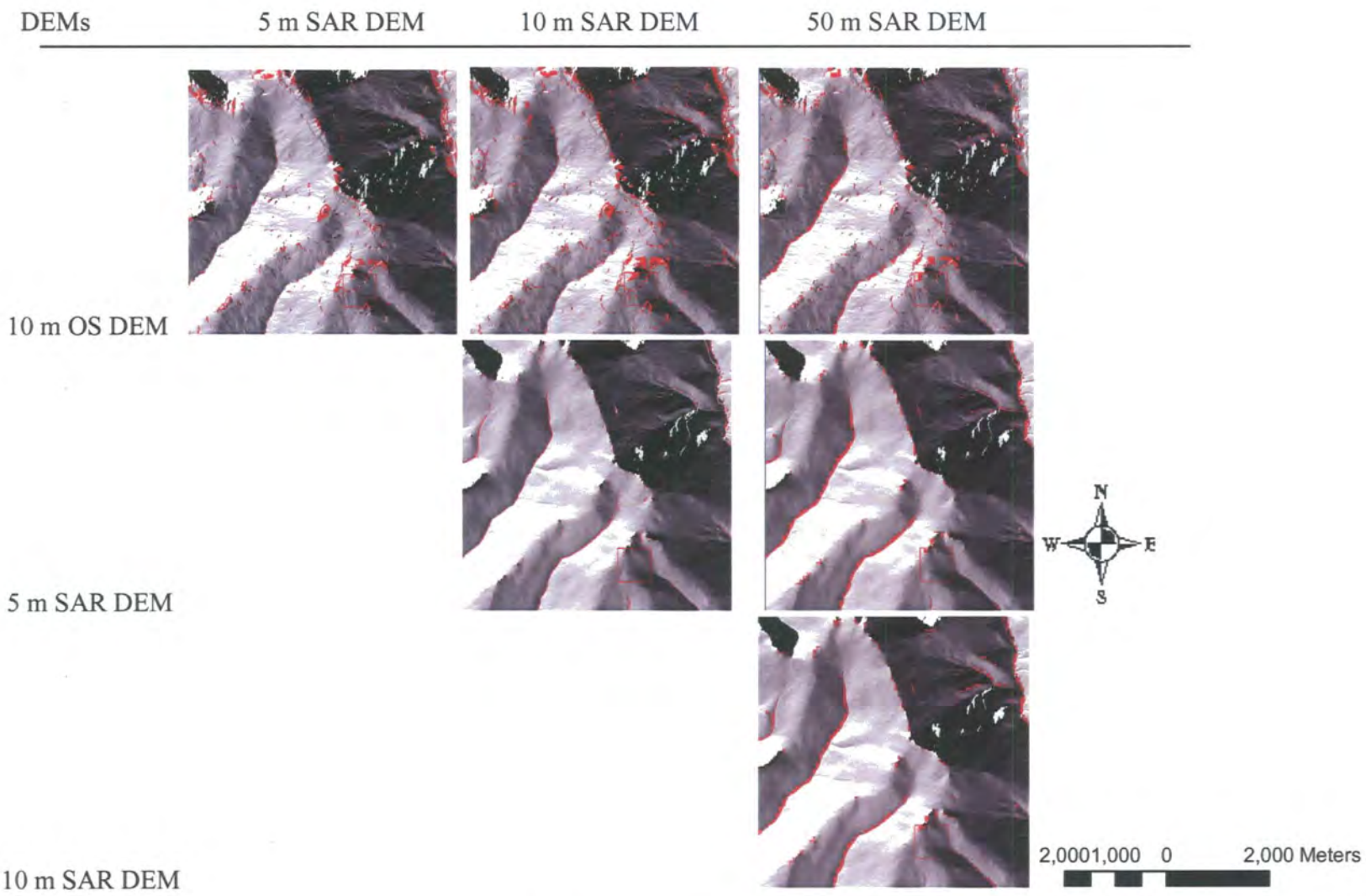

Figure 3.25 Aspect Differences in OS DEM and SAR DEM

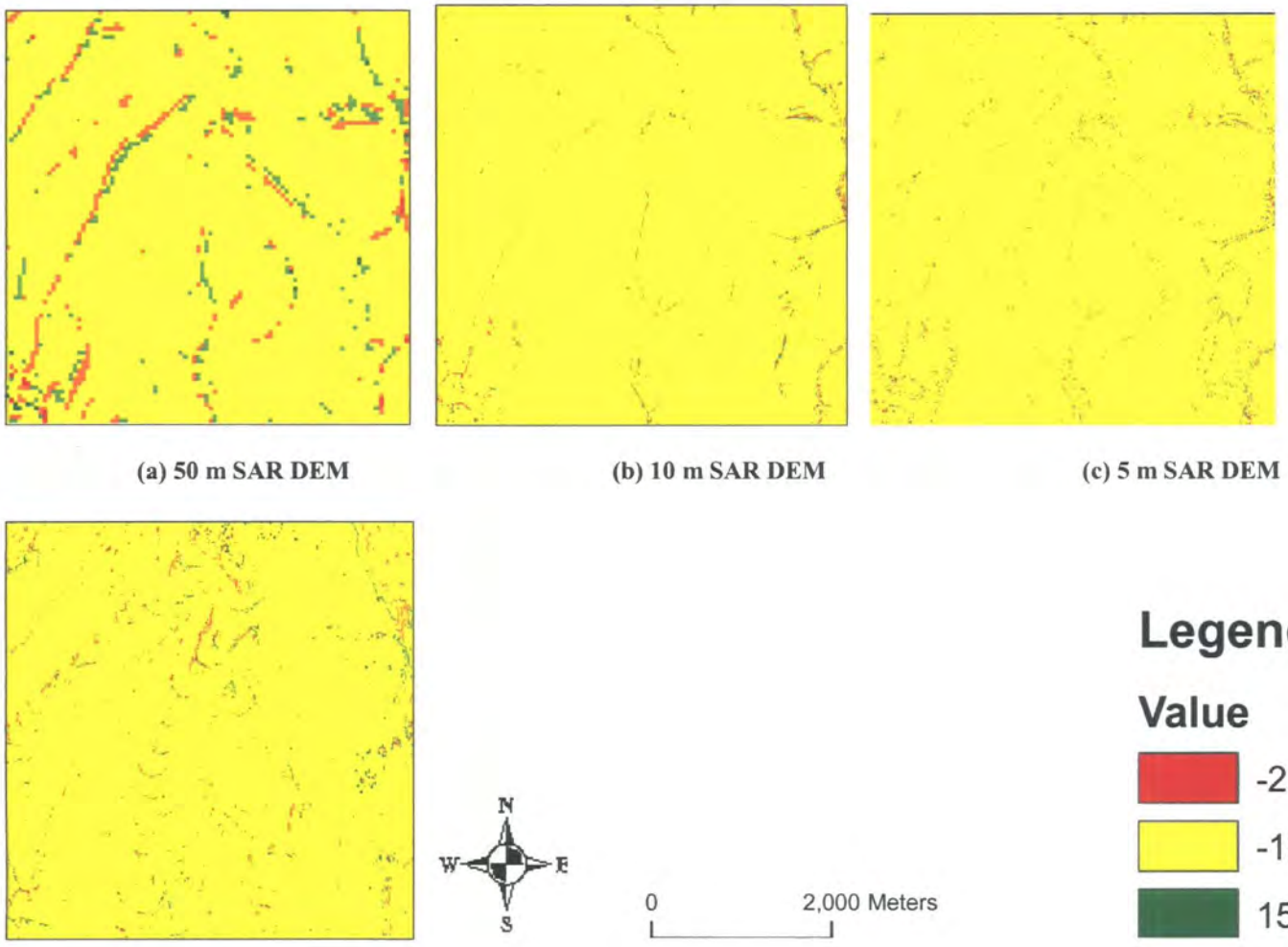

(a) 50 m SAR DEM

(b) 10 m SAR DEM

(c) 5 m SAR DEM

(d) 10 m OS DEM

Figure 3.26 Kernel size impact on aspect

Table 3.9 Comparisons of the ENVI 4.1, Arc/GIS, and SAGA aspect result for the Head House area

Statistics / DEM	Min			Max		
	ENVI	Arc/GIS	SAGA	ENVI	Arc/GIS	SAGA
InfoTerra Aerial photographs	0.0	0.0	0.0	360.0	360.0	360.0
NERC 1:6 000 Aerial photographs	0.0	0.0	0.0	360.0	360.0	360.0
5 m SAR	0.5	1.0	1.8	359.3	359.5	359.5
10 m SAR	7.1	1.3	13.8	357.7	351.2	359.9
50 m SAR	58.7	75.0	30.6	328.7	327.2	332.3
10 m OS	0.0	0.0	3.2	360.0	360.0	360.0
50 m OS	8.1	23.2	33.7	347.5	350.5	360.0
5 m LiDAR	2.9	0.0	0.2	360.0	360.0	360.0
Statistics / DEM	Mean			Std. Dev.		
	ENVI	Arc/GIS	SAGA	ENVI	Arc/GIS	SAGA
InfoTerra Aerial photographs	215.9	215.9	215.6	±72.4	±72.5	±9.6
NERC 1:6 000 Aerial photographs	203.6	180.6	203.5	±86.4	±17.6	±11.4
5 m SAR	217.1	217.2	217.2	±66.6	±66.6	±8.8
10 m SAR	215.1	217.3	215.2	±67.5	±66.2	±8.9
50 m SAR	219.4	219.7	220.1	±64.2	±64.3	±8.6
10 m OS	213.9	214.9	214.0	±70.0	±73.2	±9.4
50 m OS	216.5	216.8	217.2	±65.8	±65.8	±8.8
5 m LiDAR	213.8	216.3	216.1	±67.4	±68.0	±9.0

Fig. 3.25 compares the differences in aspect between the 10 m resolution OS DEM and all three InSAR DEMs.

The matrix shows clearly that the difference within the source of InSAR purely exists on the lines between opposite facing slopes, and they could be river channels or ridges. Apart from this kind of difference, comparisons between the 10 m resolution OS DEM and InSAR DEMs show other differences and they seem to be lying randomly in that area. Among all DEMs, the 5 m and 10 m resolution InSAR DEMs make the smallest difference.

Fig. 3.26 shows the impact of kernel size in calculation of aspect from the 10 m resolution OS DEM and InSAR DEMs at 5 m, 10 m, and 50 m resolution.

The coarse resolution DEM has larger differences in aspect when the kernel size is enlarged from 3×3 to 5×5 and these differences are on the lines of between two facing slopes, such as the river channels. In addition, the OS DEM shows some difference in along the contour lines.

Table 3.9 summarises the statistics of aspect calculation for the Head House area using the ENVI 4.2, Arc/GIS, and SAGA packages before filling any depressions. In each cell, red figures mean the largest and the black figures mean the smallest.

Comparison shows that different algorithms calculate many different minimum and maximum values. However, there is no evidence to show a relationship between the algorithm and the minimum or maximum aspect values. Although differences lie in the minimum and maximum values, mean values among these three results are relatively the same. Significant differences are seen in the standard deviation, where the algorithm in Zeverbergen and Thorne (1987) used by SAGA calculated almost one eighth value of others compared to the other two results in all cases.

3.5.4. Profile Curvature

The profile curvature, as a second order derivative to elevation, intersecting with the plane of the z-axis and the aspect direction, measures the rate of change of the slope along the profile. Principally, it measures the maximum gravity effects in the

direction orthogonally. Profile curvature statistics are summarised in Table 3.10 below (to one decimal space).

3.5.4.1. Statistical Analysis

Table 3.10 Profile curvature in radius per metre statistics for the whole study area

DEM \ Statistics		Min	Max	Mean	Std. Dev.
10 m OS	3×3	-13.3	8.7	0.0	±0.6
	5×5	-6.7	4.1	0.0	±0.3
50 m OS	3×3	-1.2	1.8	0.0	±0.1
	5×5	-0.6	0.8	0.0	±0.1
5 m SAR	3×3	-38.6	23.0	0.0	±0.7
	5×5	-17.8	8.4	0.0	±0.5
10 m SAR	3×3	-14.0	7.3	0.0	±0.4
	5×5	-6.2	4.2	0.0	±0.3
50 m SAR	3×3	-1.8	1.7	0.0	±0.1
	5×5	-0.7	0.8	0.0	±0.1

Table 3.10 summaries significant differences in the minimum and maximum values of profile curvature from different DEMs. For example, the 5 m SAR DEM has the smallest minimum profile curvature as -38.6 units and the largest maximum profile curvature as 23.0 using the 3×3 kernel size. The correspondent values are -1.8 units and 1.7 units from the 50 m SAR DEM. In contrast, mean values of profile curvature from these DEMs are roughly the same, approximately zero, which as well as the less than ±0.8 units of the standard deviation together represent relatively continuous rate of change of slope along the profile. It is noted that all images with 5×5 windows bring smaller standard deviation due to the smoothing effect from larger windows.

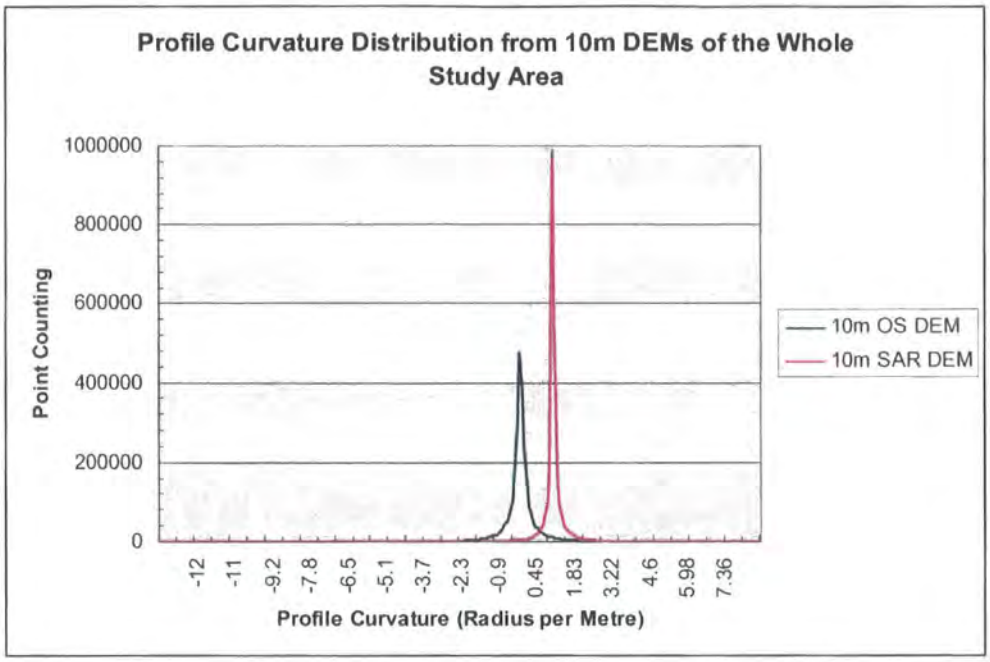

(a) 10 m DEMs

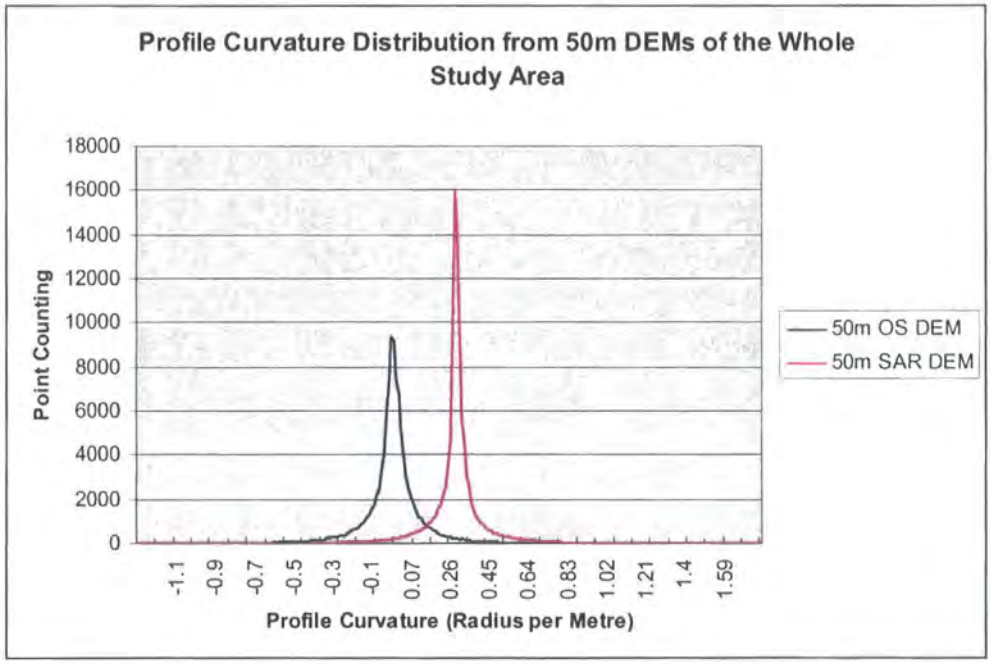

(b) 50 m DEMs

Figure 3.27 Profile curvature distribution of 10 m resolution (a) and 50 m resolution (b) DEMs of the whole study area

Fig. 3.27 shows the profile curvature distribution calculated using the ENVI 4.2 software package for DEMs of the whole study area.

In plot (a), the OS DEM has a variation of ±0.6 units which is larger than ±0.4 units from the SAR DEM.

In plot (b), the OS DEM has a smaller variation of ±0.136 units than the ±0.143 units from the SAR DEM, and the mean profile curvatures are 0 and 0.001 respectively in radius per metre. Results from both 10 m and 50 m resolution DEMs show that the SAR DEM has a larger median value in profile curvature than the OS DEM at corresponding resolution. The SAR DEM also has a peak doubled as the one from the corresponding OS DEM and hence more points in the SAR DEM have the value within ±1 unit than the OS DEM.

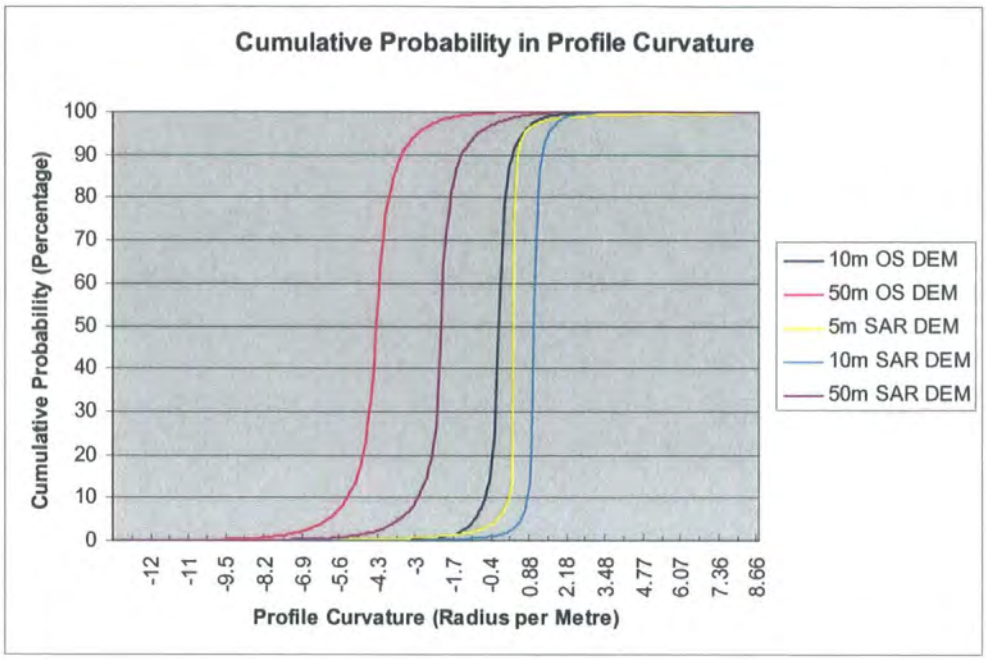

(a) the whole study area

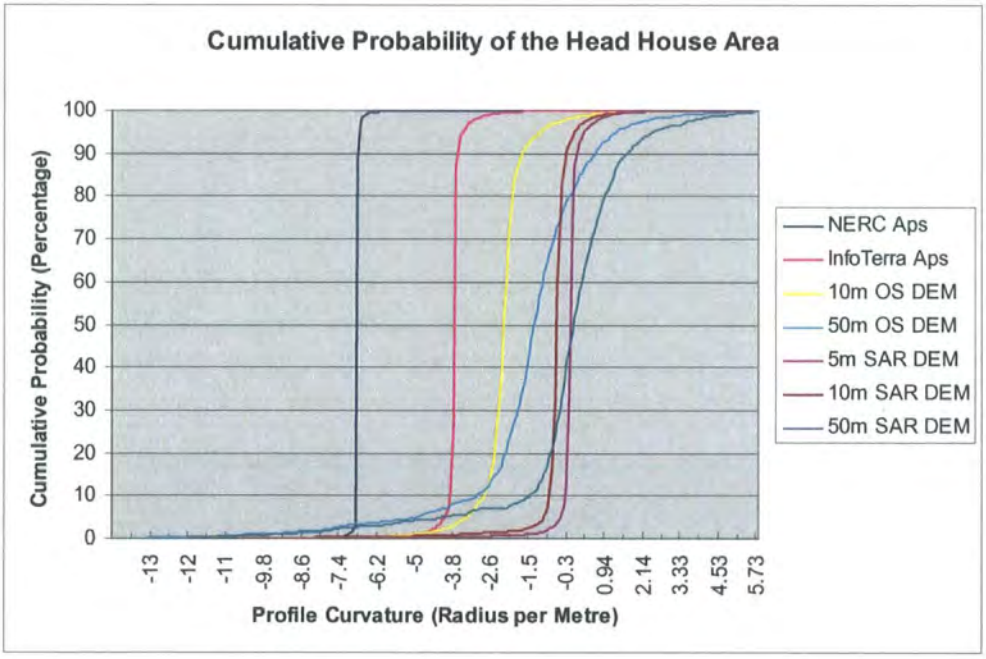

(b) the Head House area

Figure 3.28Cumulative probability of profile curvature of the (a) whole study area and (b) the Head House area

Fig. 3.28 shows the cumulative probability in profile curvature for both the whole study area and the Head House area.

It shows that the 50 m resolution DEMs have lower profile curvatures than the DEMs at finer resolutions. The 10 m DEMs and the 5 m DEM do not show significant differences for the whole study area. 50 m resolution DEMs show bigger differences than the higher resolution DEMs in accumulation profile curvature, where the former cumulate increase at a much lower rate than the other DEMs in the Head House area.

3.5.4.2. Profile Curvature Difference Comparison

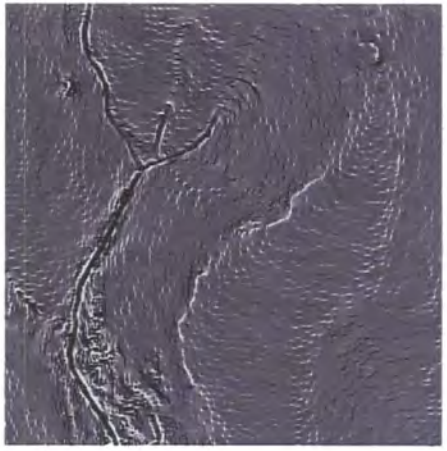

(a) 5 m SAR DEM

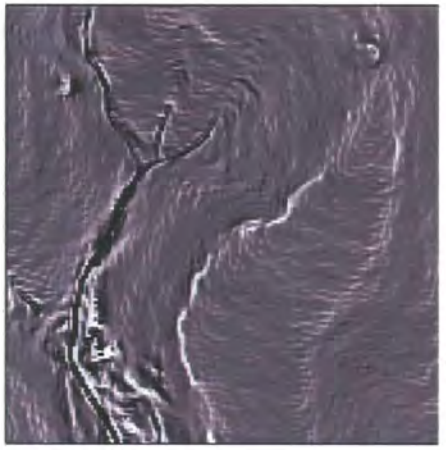

(b) 10 m SAR DEM

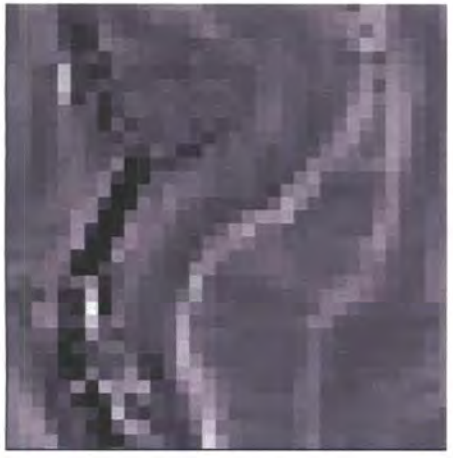

(c) 50 m SAR DEM

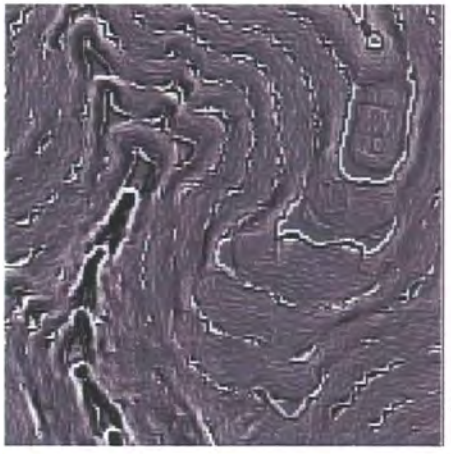

(d) 10 m OS DEM

Figure 3.29Profile curvature maps of a 400 m ×400 m area

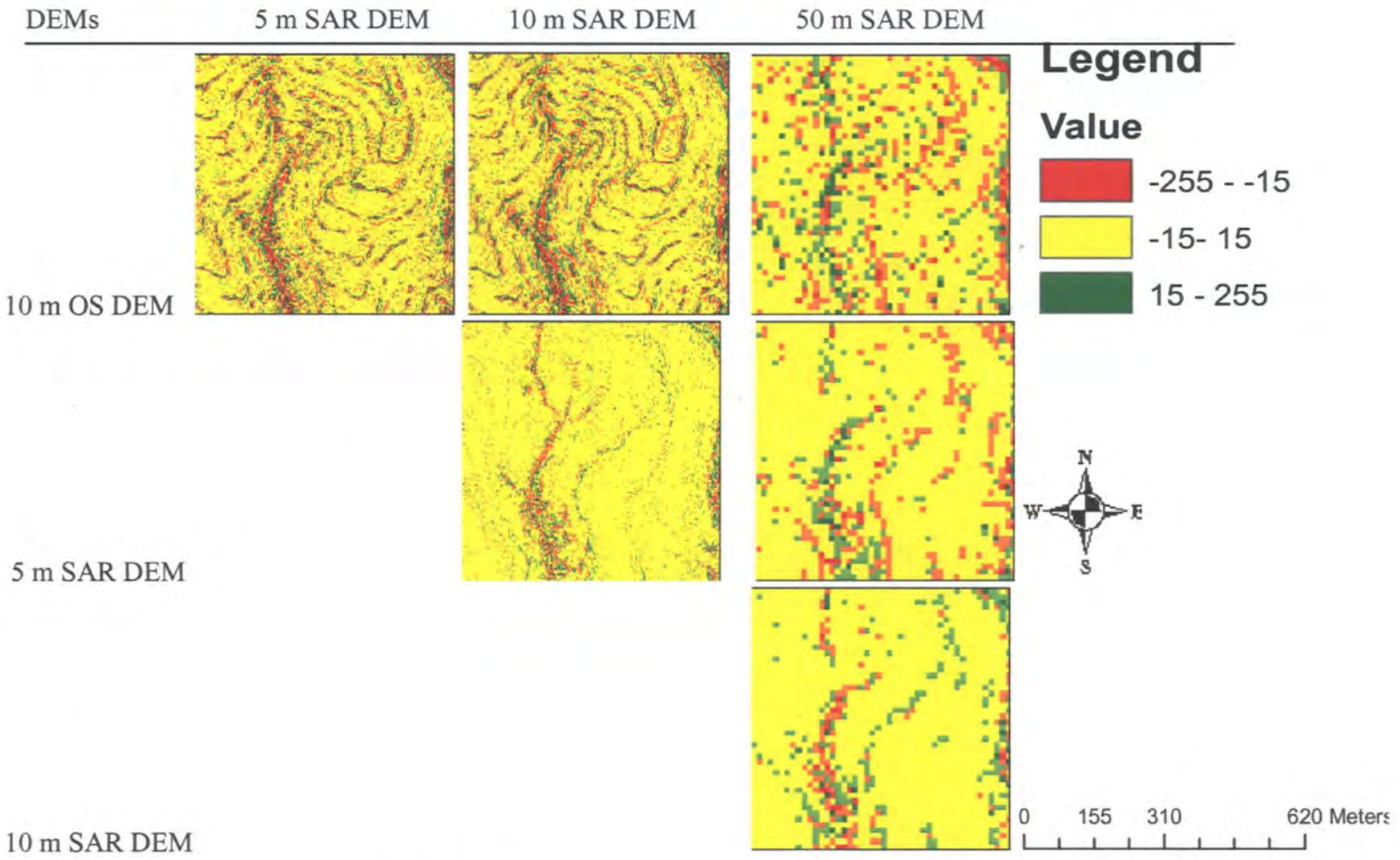

Figure 3.30 Profile curvature differences maps from the 10m resolution OS DEM and SAR DEMs

Fig. 3.29 shows profile curvature maps in an area of c. 500 m×500 m for all SAR DEMs and the 10 m resolution OS DEM calculated using the Arc/GIS package.

The profile curvature was rescaled to 0 to 255. The map from a 5 m resolution SAR DEM shows the clearest profile curvature and the smoothest one is from the 50 m SAR DEM. The map from the 10 m OS DEM shows changes in the profile curvature along the contours.

Fig. 3.30 shows the differences in profile curvature for the same site in Fig. 3.28, calculated using the Arc/GIS as well.

The difference was rescaled to -255 to 255. The red and green parts mean the area with negative and positive differences in profile curvature respectively. The comparison between the 5 m and the 10 m SAR DEMs shows the clearest surface features which is possibly the ridge or river channels. The comparisons between the 10 m OS DEM and the 5 m and the 10 m SAR DEMs contain differences in not only the location of facing slopes also on contour lines. The comparisons between the 5 m and the 50 m SAR DEMs and the 10 m and the 50 m SAR DEMs show much coarser result. The one from the 10 m OS DEM and the 50 m SAR DEM cannot display any reasonable feature on the surface.

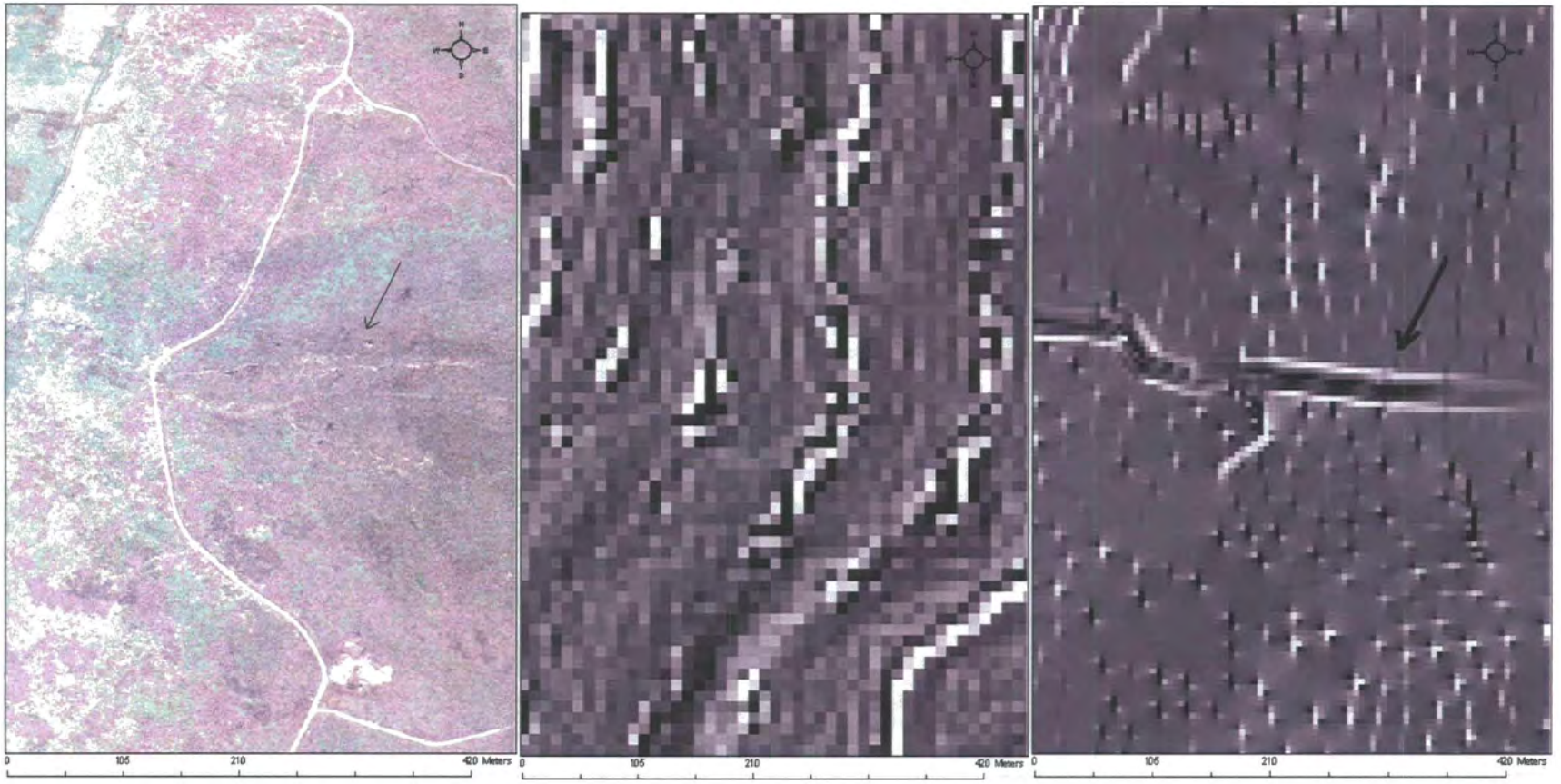

Figure 3.31 Same stream in different images (The left hand one is a colour aerial photograph at 1:15 000 scale, the middle image is a DEM profile curvature map from 10 m resolution OS DEM and the right hand one is from 5 m resolution SAR DEM profile curvature map)

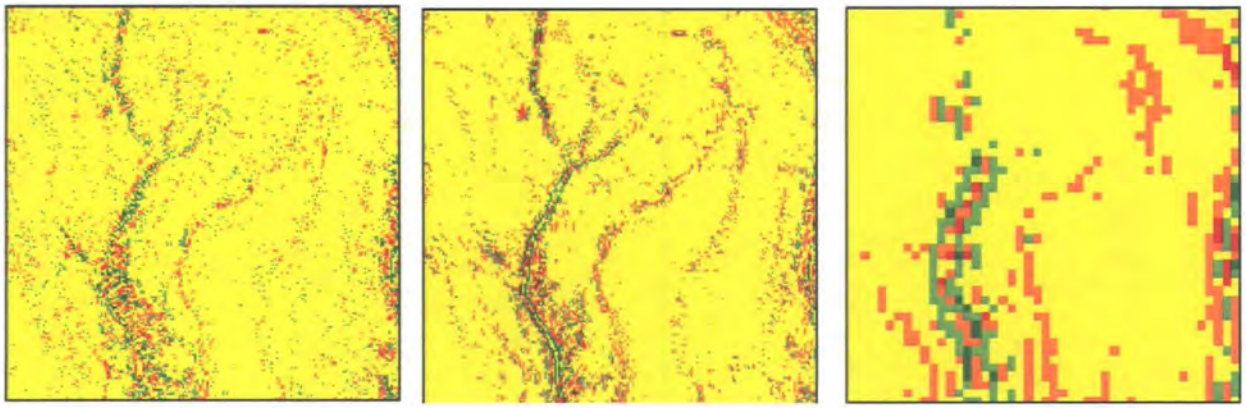

(a) 5 m SAR DEM

(b) 10 m SAR DEM

(c) 50 m SAR DEM

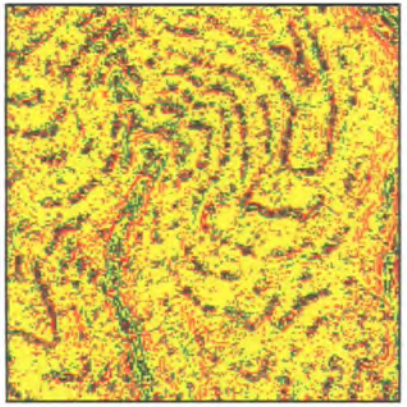

(d) 10 m OS DEM

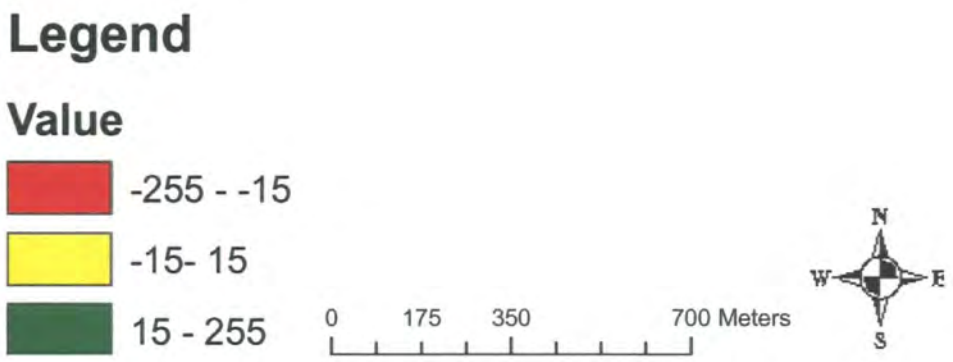

Figure 3.32 Kernel size impact on profile curvature difference

The black arrow in Fig.3.31 indicates a drainage which is obviously identified in the profile curvature maps from the 5 m resolution SAR DEM and. However, it cannot be found on the profile curvature maps generated from the 10 m resolution OS DEM and the 50 m resolution SAR DEM. In images from kernel size of five similar results can be seen.

3.5.4.3. Algorithm Comparison

Since the ArcGIS package only calculates curvature rather than the curvature in profile and plan directions separately, no calculation result is available from the ArcGIS for profile curvature.

Profile curvature statistics tend to be different for different algorithms. The quadratic surface in Evans (1979) used by the ENVI package tends to compute much smaller minimum value and larger maximum value from all DEMs than the one from Zeverbergen and Thorne (1987) used by the SAGA. For example, the ENVI calculated c. -1704.0 as the minimum profile curvature and c. 2732.6 as the maximum value from the NERC APs DEM compared to the results from the SAGA as c. -103.7 and 80.9 respectively. In addition, the SAGA calculated relatively smaller standard deviation from all DEMs. For both algorithms, mean values of profile curvature are relatively equal.

Table 3.11 Comparison profile curvature calculation result from ENVI 4.1, Arc/GIS and SAGA packages in the Head House area

Statistics / DEM	Min.		Max.		Mean		Std. Dev.	
	ENVI	SAGA	ENVI	SAGA	ENVI	SAGA	ENVI	SAGA
InfoTerra Aerial photographs DEM	-78.3	-1.6	68.4	1.8	0.0	0.0	±2.3	0.0
NERC 1:6 000 Aerial photographs DEM	-1704.0	-103.7	2732.6	80.9	0.2	0.0	±18.8	±0.7
5 m SAR	-14.5	-0.2	5.8	0.1	0.0	0.0	±0.5	0.0
10 m SAR	-6.1	-0.1	2.7	3.8	0.0	0.0	±0.3	±0.3
50 m SAR	-0.6	-0.0	0.2	0.0	0.0	0.0	±0.1	0.0
10 m OS	-7.8	-0.1	5.0	3.8	0.0	0.0	±0.5	±0.3
50 m OS	-0.6	-0.0	0.4	0.0	0.0	0.0	±0.1	0.0
5 m LiDAR	-21.3	-0.3	12.3	0.2	0.0	0.0	±2.1	0.0

Table 3.12 Summary of slope, aspect and profile curvature in the whole study area

Statistics / DEM	Slope				Aspect				Profile curvature			
	Min	Max	Mean	Std. Dev.	Min	Max	Mean	Std. Dev.	Min	Max	Mean	Std. Dev.
10 m OS	0.0	52.5	7.8	±6.6	0.0	360.0	171.4	±85.2	-13.3	8.7	0.0	±0.6
50 m OS	0.0	32.4	7.2	±5.4	0.4	360.0	168.9	±83.9	-1.2	1.8	0.0	±0.1
5 m SAR	0.0	64.4	7.8	±6.5	0.0	360.0	169.9	±84.9	-38.6	23.0	0.0	±0.7
10 m SAR	0.0	56.4	7.7	±6.3	0.0	360.0	169.6	±84.6	-14.0	7.3	0.0	±0.4
50 m SAR	0.0	32.3	7.1	±5.4	0.0	360.0	168.8	±83.7	-1.8	1.7	0.0	±0.1

Table 3.13 Summary of slope, aspect and profile curvature in the Head House area

Statistics / DEM	Slope				Aspect			
	Min	Max	Mean	Std. Dev.	Min	Max	Mean	Std. Dev.
10 m OS	0.0	88.5	7.6	±1.4	0.0	360.0	213.9	±70.0
50 m OS	0.1	88.5	7.4	±1.3	8.1	347.5	216.5	±65.8
5 m SAR	0.0	37.7	6.3	±0.5	0.5	359.3	217.1	±66.6
10 m SAR	0.6	21.4	5.9	±0.4	7.1	357.7	215.1	±67.5
50 m SAR	0.5	18.6	5.8	±0.3	58.7	328.7	219.4	±64.2
0.5 m NERC Aerial photographs	0.0	88.0	9.4	±1.3	0.0	360.0	203.6	±86.4
3 m InfoTerra Aerial photographs	0.0	67.2	7.5	±0.8	0.0	360.0	215.9	±72.4
5 m LiDAR	0.0	47.2	6.8	±0.9	2.9	360.0	213.8	±67.4

Statistics of slope, aspect and profile curvature from DEMs of the whole study area were summarised in Table 3.12. Statistics of slope and aspect from eight DEMs of the Head House area were summarised in Table 3.13. Since slope and aspect were more crucial than profile curvature in geomorphological and hydrological research in the Head House area, profile curvature data were ignored in this table to keep clear.

3.5.5. Topographic Wetness Index

Both algorithms and DEM resolution have impacts on the Topographic Wetness Index (TWI) derivation. Different algorithms cause different flow path definition and hence different upslope contributing area. Low resolution may fail to represent some convergent slope features. However, too fine a resolution may introduce perturbations to flow directions and slope angles that may not represent the real flow direction as well. (Beven, 2000)

3.5.5.1. Statistical Analysis

The Topographic Wetness Index was calculated for both the Head House area and the flood inundation model area using the SAGA. Statistics are summarised in Table 3.14 and Table 3.15 to one decimal place.

Table 3.14 Topographic Wetness Index of the Head House area

Statistics / DEM	Min.	Max.	Mean	Std. Dev.	5% Percentile	95% Percentile
50 m SAR	5.7	13.8	8.1	1.1	9.5	6.5
10 m SAR	-0.7	15.8	7.5	1.4	8.8	5.7
5 m SAR	2.1	18.5	7.6	1.0	8.8	5.7
10 m OS	-0.7	18.7	7.4	1.8	9.8	4.9
50 m OS	5.7	14.1	8.1	1.1	9.6	6.6
NERC Aerial photographs	-3.6	21.8	5.6	2.7	10.6	1.5
InfoTerra Aerial photographs	0.5	20.0	7.0	1.9	9.6	3.8
5 m LiDAR	1.8	16.6	7.4	1.2	9.1	5.3

Table 3.15 Topographic Wetness Index of the flood inundation model test area

Statistics / DEM	Min.	Max.	Mean	Std. Dev.	5% Percentile	95% Percentile
5 m LiDAR	0.5	15.3	5.5	2.5	10.9	2.2
5 m SAR	2.1	16.8	6.1	2.5	11.4	3.4
10 m OS	3.3	15.3	7.7	3.0	12.9	4.2
10 m SAR	3.1	13.9	6.1	1.6	10.0	4.4

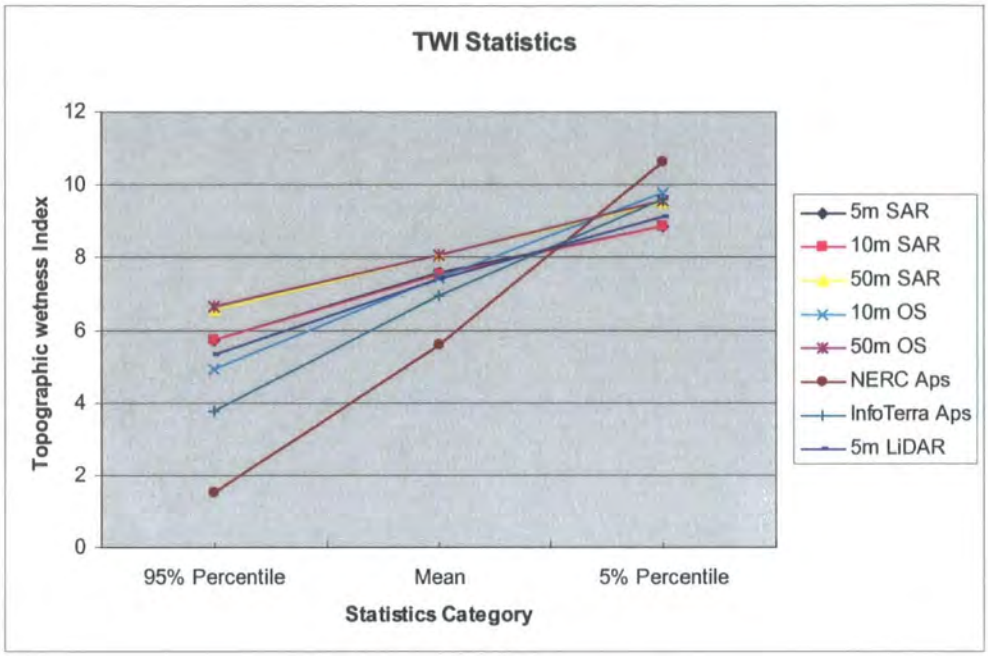

(a) the Head House area

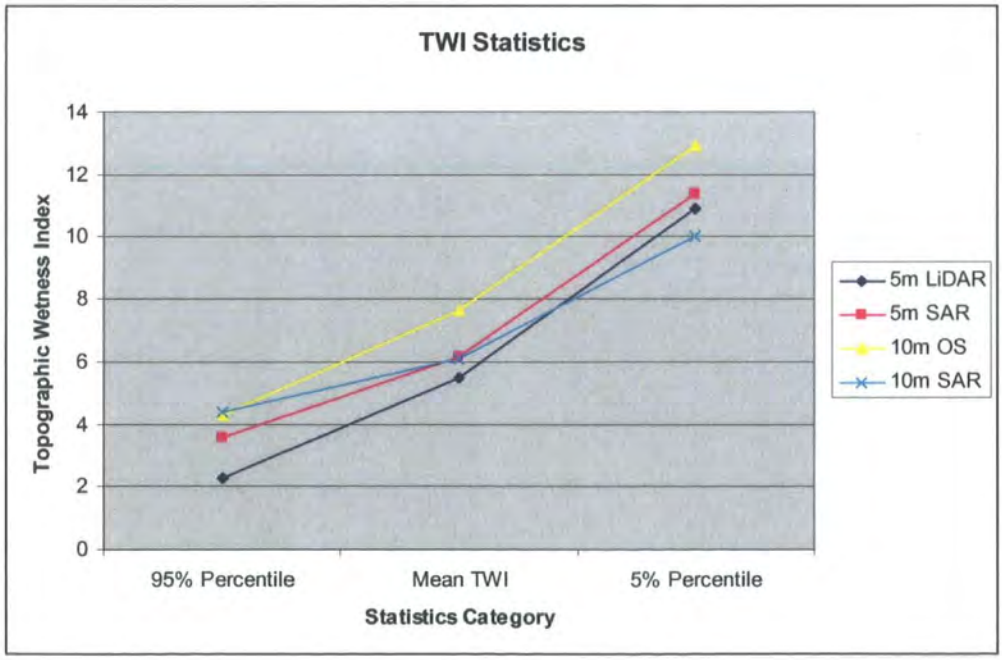

(b) Model test area

Figure 3.33TWI statistics of (a) the Head House area and (b) the model test area

Fig. 3.33 shows the 95% Percentile, mean and 5% percentile values of the Topographic Wetness Index for the Head House area and the model test area.

The Topographic Wetness Index calculation varies within DEM resolution and data source.

- Within the same source of dataset, a coarser resolution DEM has larger minimum and mean values and a smaller maximum value. For example, the 50 m SAR DEM calculates 5.7 and 13.8 as the minimum and maximum TWI while the 10 m SAR DEM computes -0.7 and 15.8 respectively. One exception is the difference between the 5 m and the 10 m SAR DEMs, where the former DEM calculated a higher mean value of the TWI for both the Head House area and the model test area. Fig. 3.34 (a) shows clearly that the increase trend of the TWI from 95% percentile to mean value then to the 5% percentile is different from data sources. The 5 m LiDAR DEM calculates a more similar TWI to the 5 m SAR DEM.
- DEMs at the same resolution tend to have similar results. For example, the differences in the maximum TWI from the 50 m SAR DEM and the 50 m OS DEM is only -0.3 for the Head House area while there is only no difference in both the minimum and mean values for the same area. The coarser the DEMs, the more similarity in DEMs at the same resolution. However, this result is not significant in the flood model test area.
- In the flood model test area, the LiDAR DEM shows a much smaller minimum TWI value (0.5) and similar standard deviation to the 5 m SAR DEM. The 10 m OS DEM shows a much larger 5% percentile value as 12.9 than 11.3 in the 5 m SAR DEM followed by 10.9 and 10.0 in the 5 m LiDAR DEM and the 10m SAR DEM respectively. Both 10 m DEMs show larger 95 % values than both 5 m DEMs which means the 5 m DEMs tend to have more areas with low TWI values than the 10 m DEMs.
- The 0.5 m DEM derived from the NERC aerial photographs has much different TWI values than others as shown in Fig. 3.32 (a).

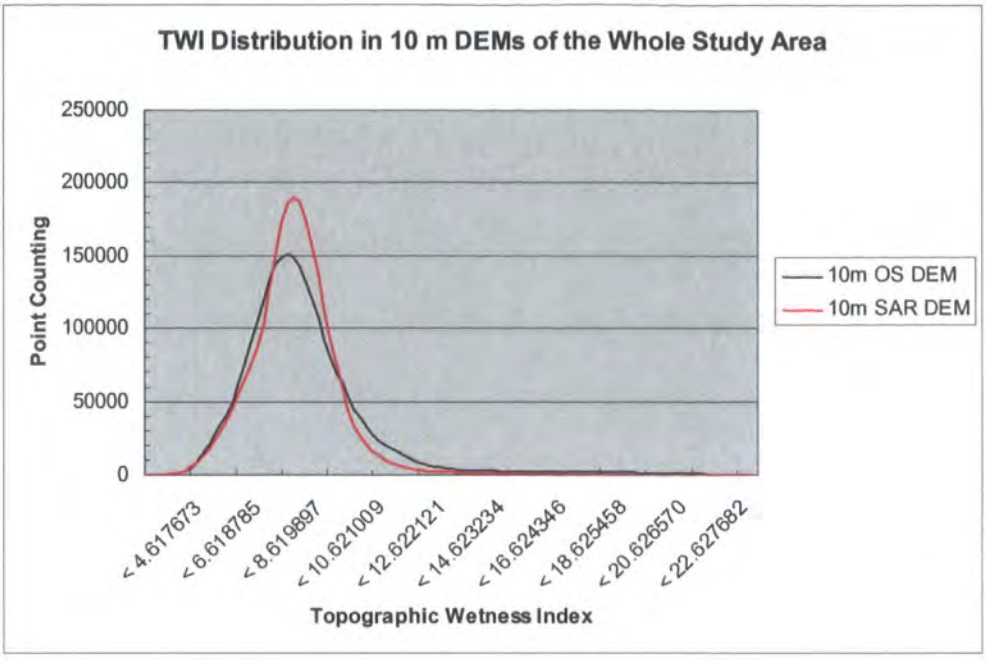

(a) 10 m DEMs

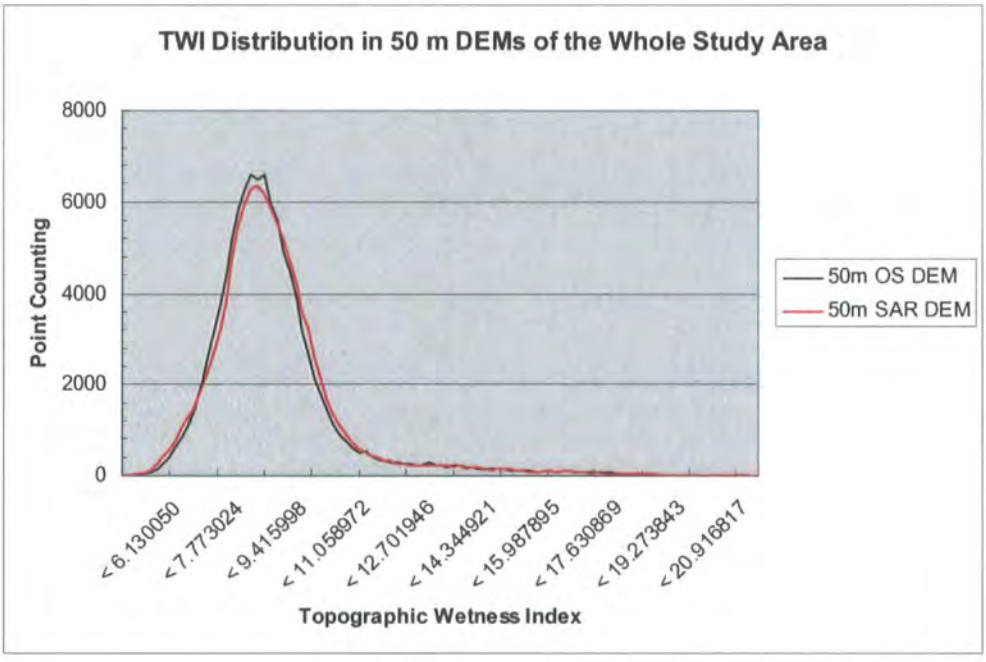

(b) 50 m DEMs

Figure 3.34Topographic Wetness Index distribution of 10 m DEMs and 50 m DEMs of the whole study area

Fig. 3.34 shows the TWI distribution in both 10 m DEMs and 50 m DEMs of the whole study area calculated using the SAGA package.

In plot (a), the mean TWIs are 7.5 and 7.4 from the OS DEM and the SAR DEM respectively. Their standard deviations are ±1.4 and ±1.8 respectively. Both DEMs

show similar patterns of distribution in the Topographic Wetness Index of the whole study area. The 10 m SAR DEM produces higher peak (c. 18000 points) than (c. 15000 points) the one from the OS data.

In plot (b), the mean TWIs are both 8.1 from the OS DEM and the SAR DEM. Their standard deviations are ±1.4 and ±1.8 respectively. Like the DEMs at 10 m resolution, both DEMs at 50 m resolution show similar pattern of distribution in the Topographic Wetness Index of the whole study area. Differently, the DEM from the OS data shows a slightly more (c. 300) points at the peak.

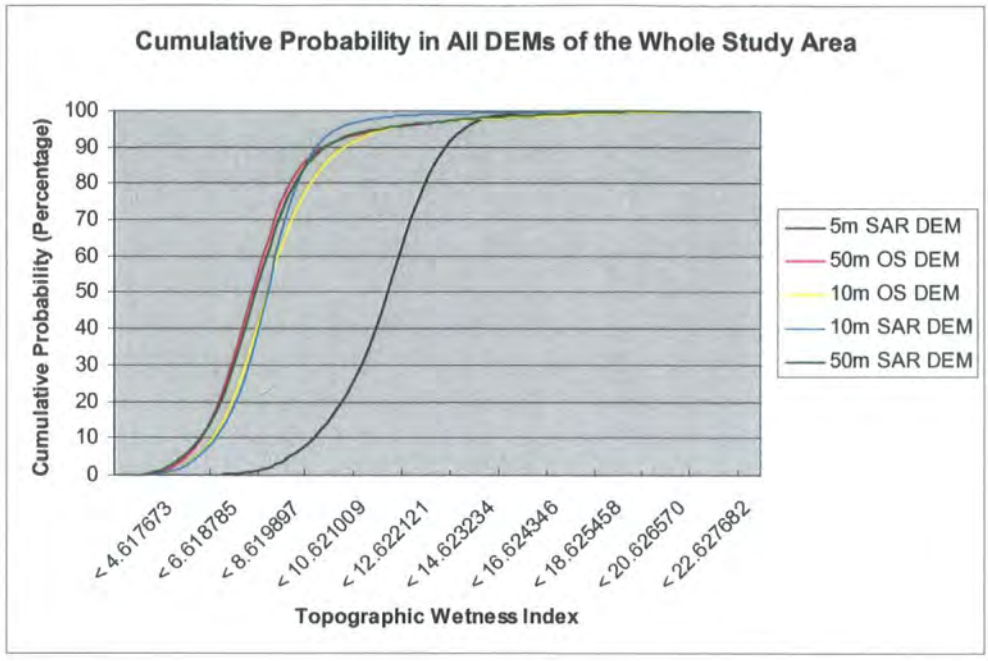

(a) the whole study area

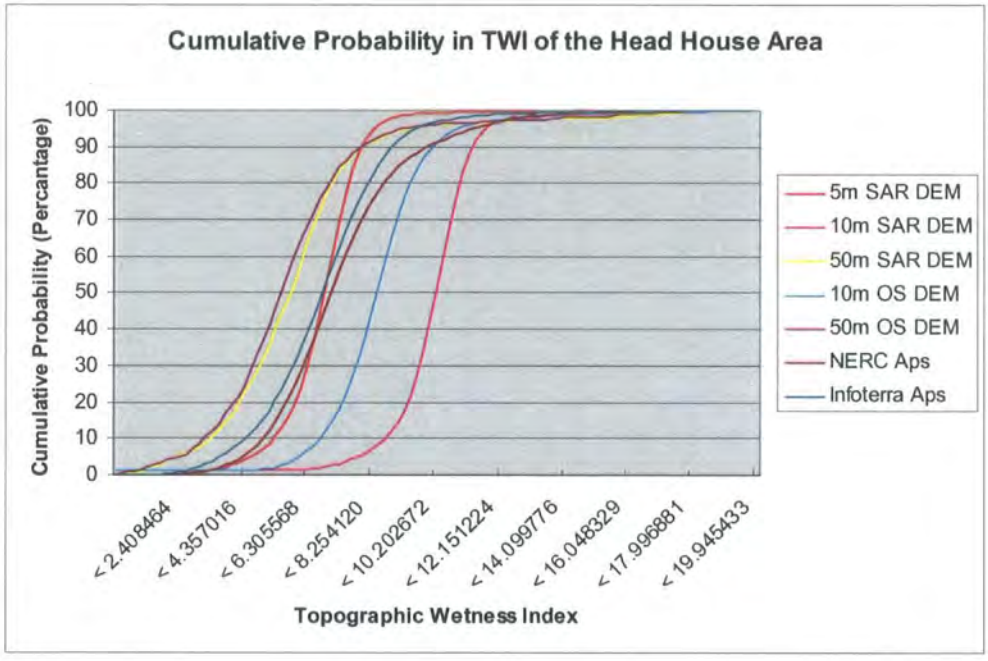

(b) Head House Area

Figure 3.35 Cumulative probability of the TWI in all DEMs of both study areas

Fig. 3.35 shows the cumulative probability of the Topographic Wetness Index from all eight DEMs of the whole study area (a) and the Head House area calculated by the SAGA package.

All DEMs show similar patterns of cumulative probability in the Topographic Wetness Index of the whole study area. The 5 m SAR DEM tends to have larger values of the

TWI than other DEMs in most areas. 10 m DEMs tend to increase quicker than the DEMs at 50 m resolution and the DEMs derived from aerial photographs as well as the 5 m SAR DEM show mediate increasing rate in accumulation.

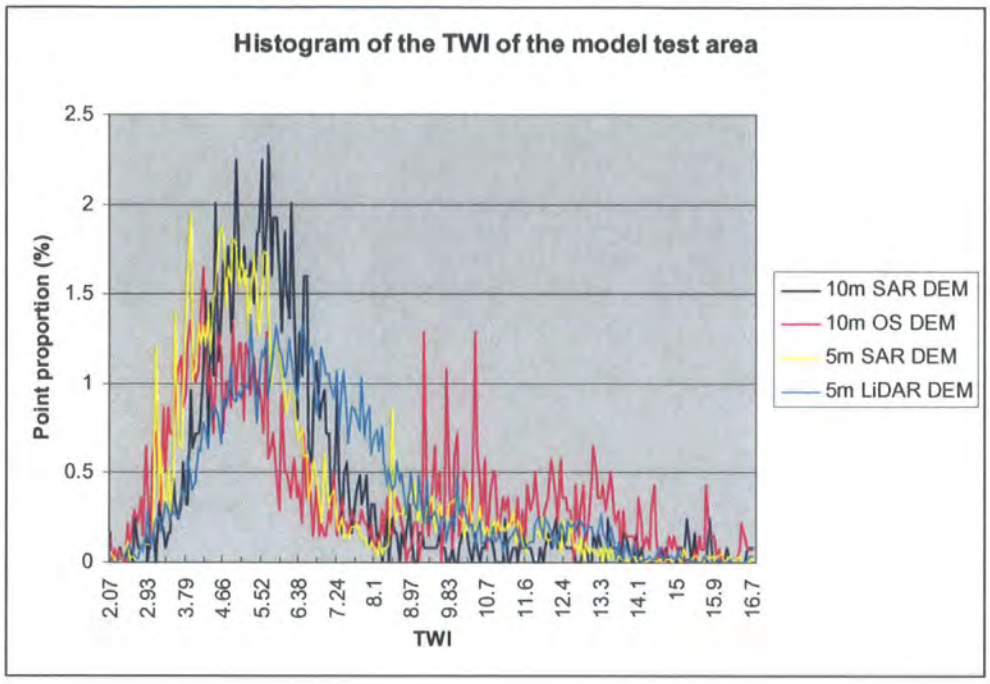

(a) Histogram

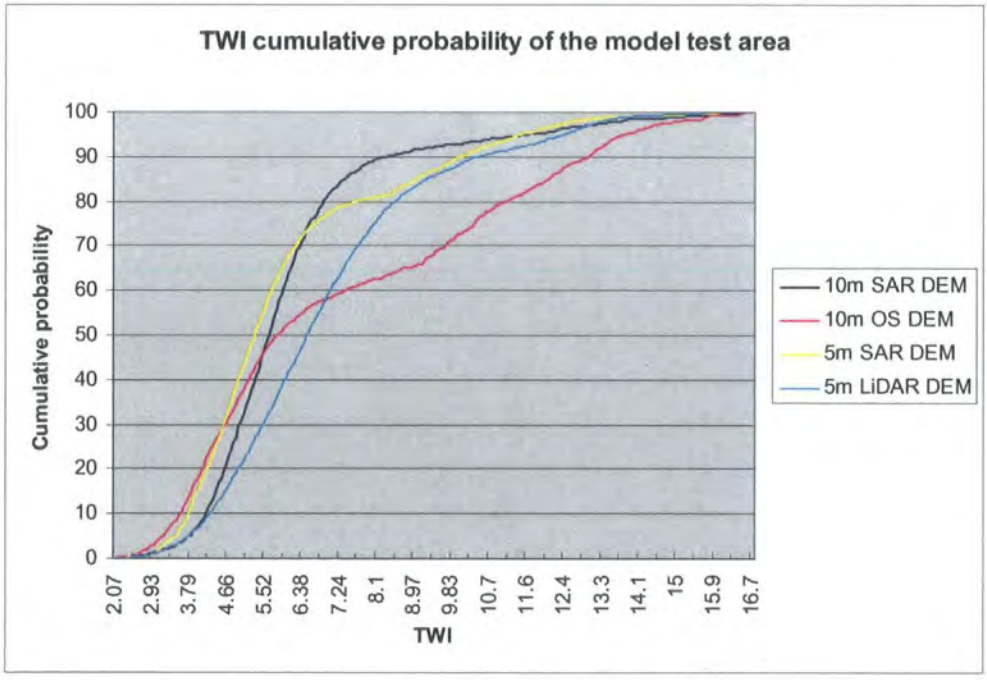

(b) Cumulative probability

Figure 3.36TWI histogram and cumulative probability of the model test area

Fig. 3.36 shows the histogram and cumulative probability of the Topographic Wetness Index of the model test area.

The histogram shows that both SAR DEMs receive much higher peaks than the OS DEM and the LiDAR DEM. The OS DEM shows a larger area in high TWI value than other three DEMs. Therefore, the cumulative probability increases slower than others. The cumulative probability shows that significant difference exists between the 10 m OS DEM and other DEMs. Both SAR DEMs are similar.

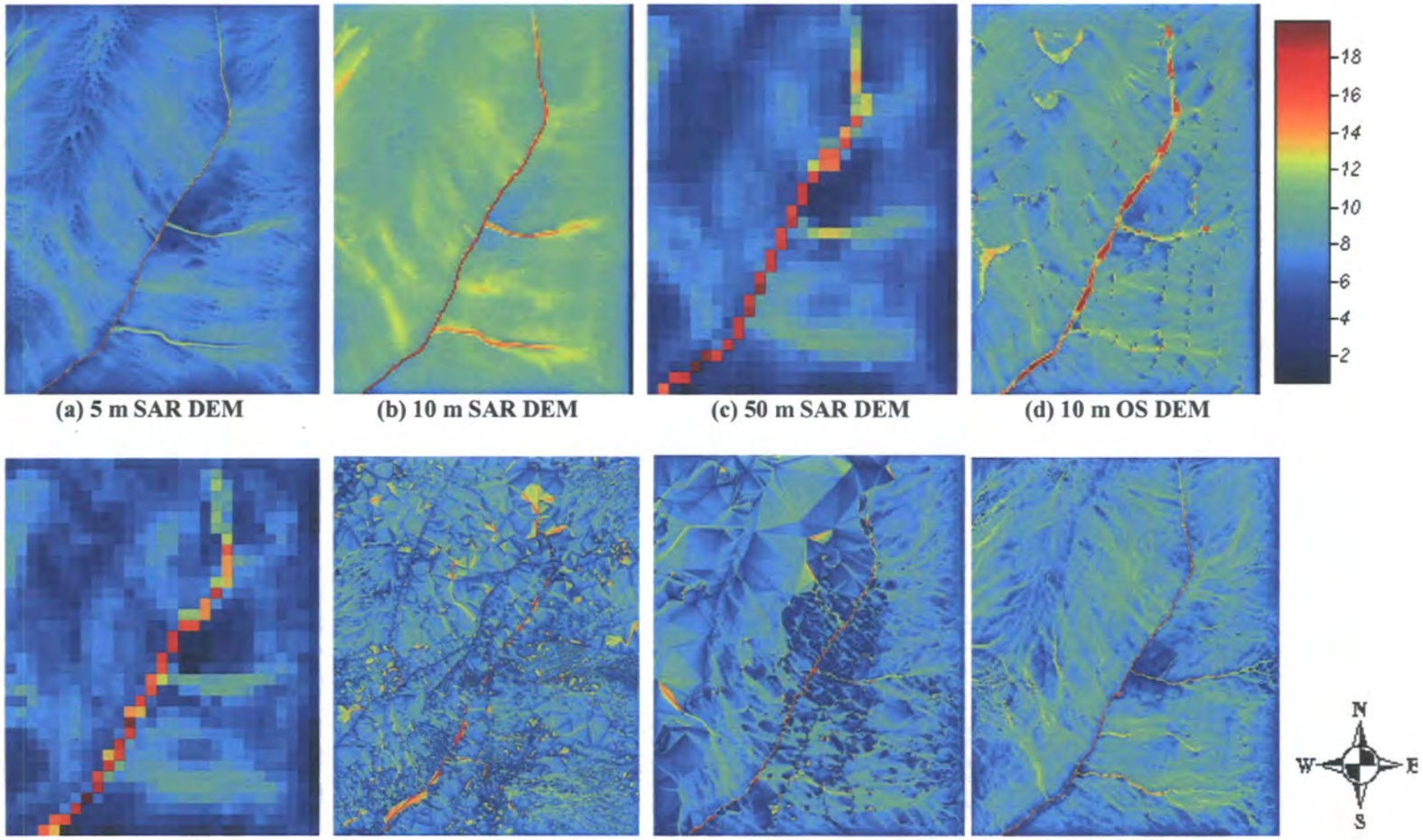

Figure 3.37 Topographic Wetness Index maps of the Head House area

3.5.5.2. TWI Visualisation

Fig. 3.37 illustrates the visualisation of the Topographic Wetness Index from all DEMs of the Head House area, which were calculated using the SAGA package based on the multiple flow direction algorithm. Results from both 5 m DEMs show a good representation in surface texture as well as river channels. Results from both 10 m DEMs are only able to show the channels. Results from both 50 m DEMs can only separate the river channel from slope side and not show any more details on the surface. Results from both APs DEMs present a large number of blocks on the surface.

3.5.5.3. TWI Difference Comparison

Fig. 3.38 shows the differences in the TWI from all DEMs of the Head House area calculated using the SAGA package. The difference was rescaled to -2 to 2. Differences are only interpretable when either comparing the results from DEMs at the same resolution or from the same data source. These differences only exist in the river channels and other areas with high Topographic Wetness Index values.

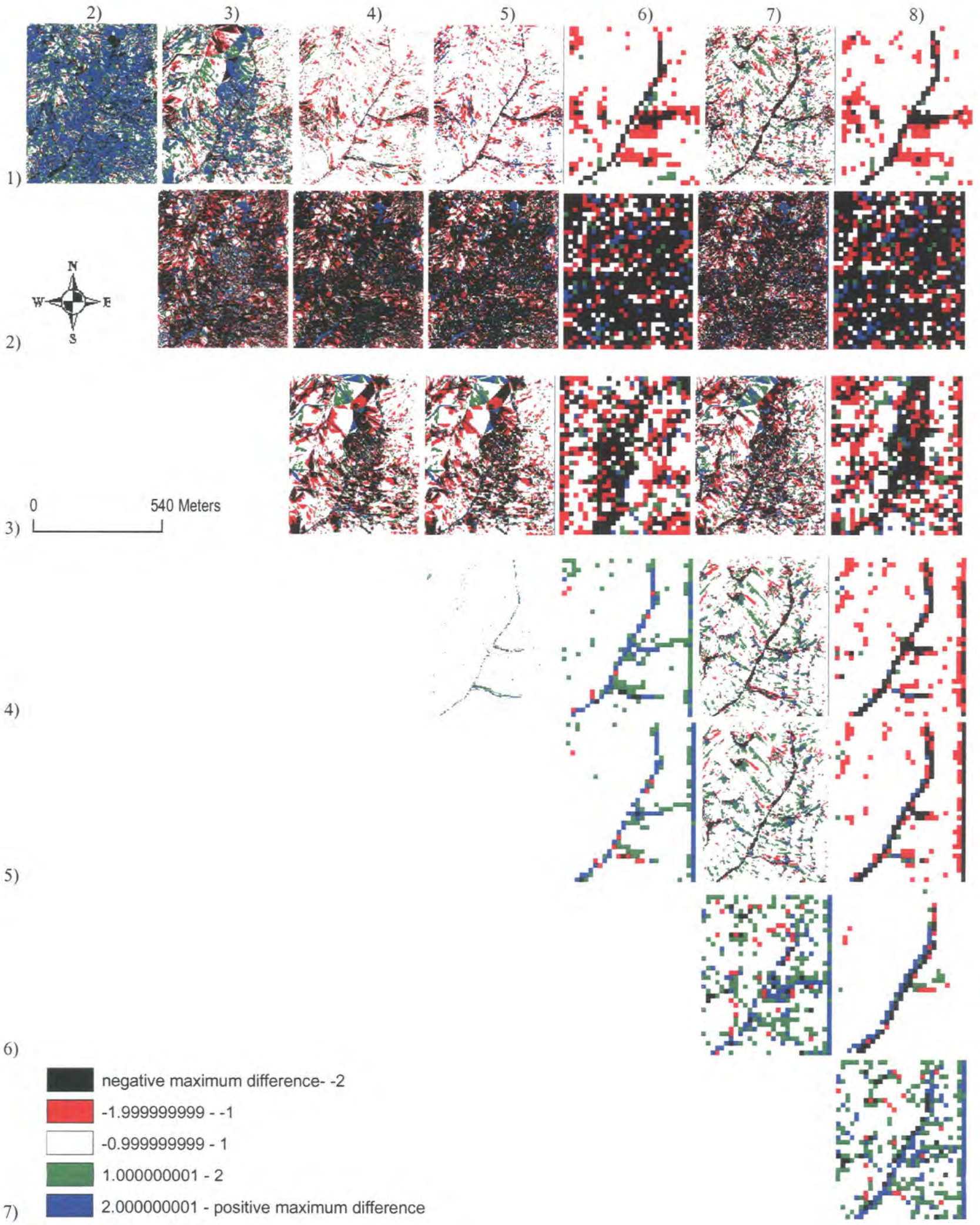

Note: 1) 5 m LiDAR DEM; 2) 0.5 m NERC APs DEM; 3) 3 m InfoTerra APs DEM; 4) 5 m SAR DEM; 5) 10 m SAR DEM; 6) 50 m SAR DEM; 7) 10 m OS DEM; 8) 50 m OS DEM

Figure 3.38 TWI Differences Maps of the Head House Area

3.6. Applications

To better understand the differences among all DEMs, each pair of DEMs was subtracted to create difference images using the Arc/GIS. Both 5 m DEMs derived from the SAR and LiDAR data as well as the DEM derived from post-event aerial photographs were taken as examples for further investigation of data source impacts.

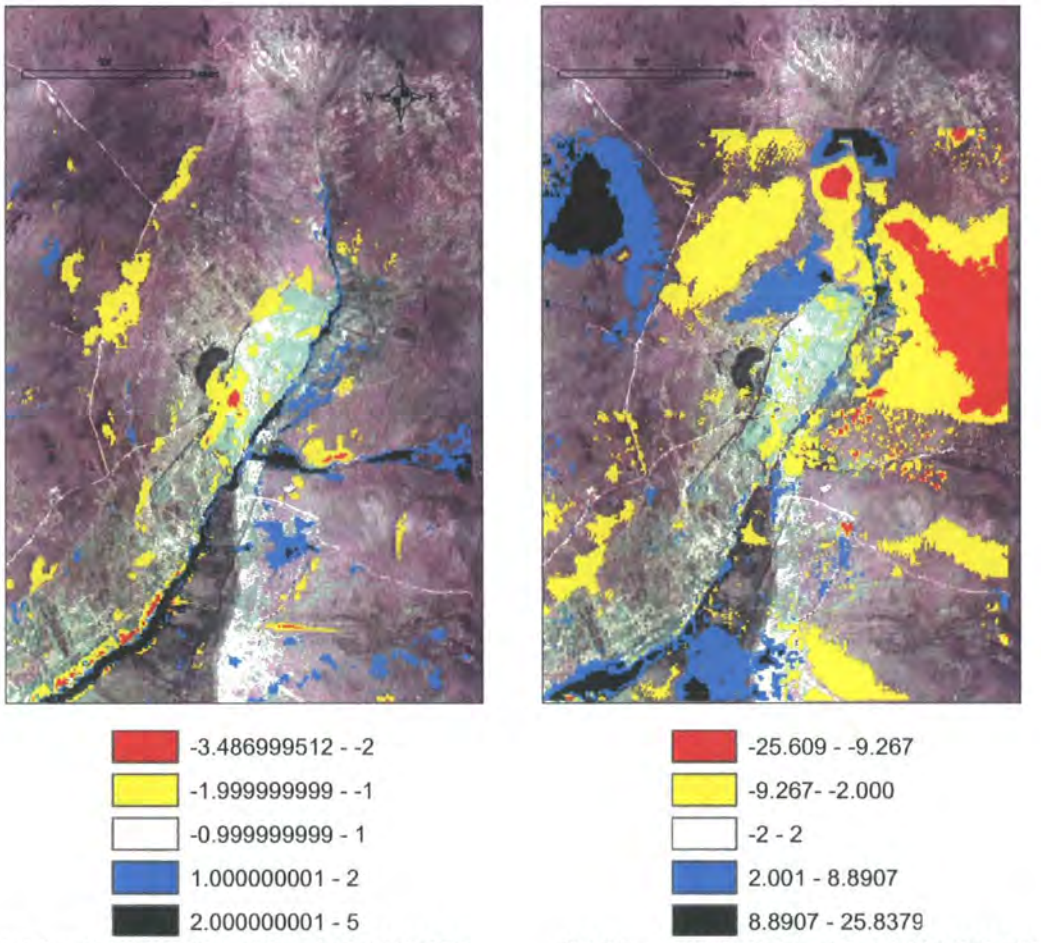

(a) 5 m SAR DEM and 5 m LiDAR DEM **(b) 0.5 m APs DEM and 5 m LiDAR DEM**

Figure 3.39 Elevation difference between the 5 m SAR DEM and the 5 m LiDAR DEM of the Head House area with the post-event 1:15 000 NERC aerial photographs as background. Differences were scaled to five categories and the colour of difference from -1 to 1 was set to transparent.

Plot (a) shows that elevation values in both DEMs agree reasonably well, as the majority of locations in the Head House area show a difference of less than 1 m. As the SAR data were captured before the flood and landslide event, the dark blue areas in plot (a) clearly show that the LiDAR DEM is able to detect important geomorphological changes such as the peat slide and the possible channel and bank

erosion. The LiDAR DEM also demonstrates its ability to remove the dense trees from the surface model.

Plot (b) shows DEMs derived from the post-event aerial photographs and LiDAR survey. As elevation difference from these two DEMs is less than 1 m in most part of the channels and the peat slide area, both DEMs are able to represent the topography after the event. However, both DEMs show large disagreement in part of the heather field which is shown in purple on the aerial photographs.

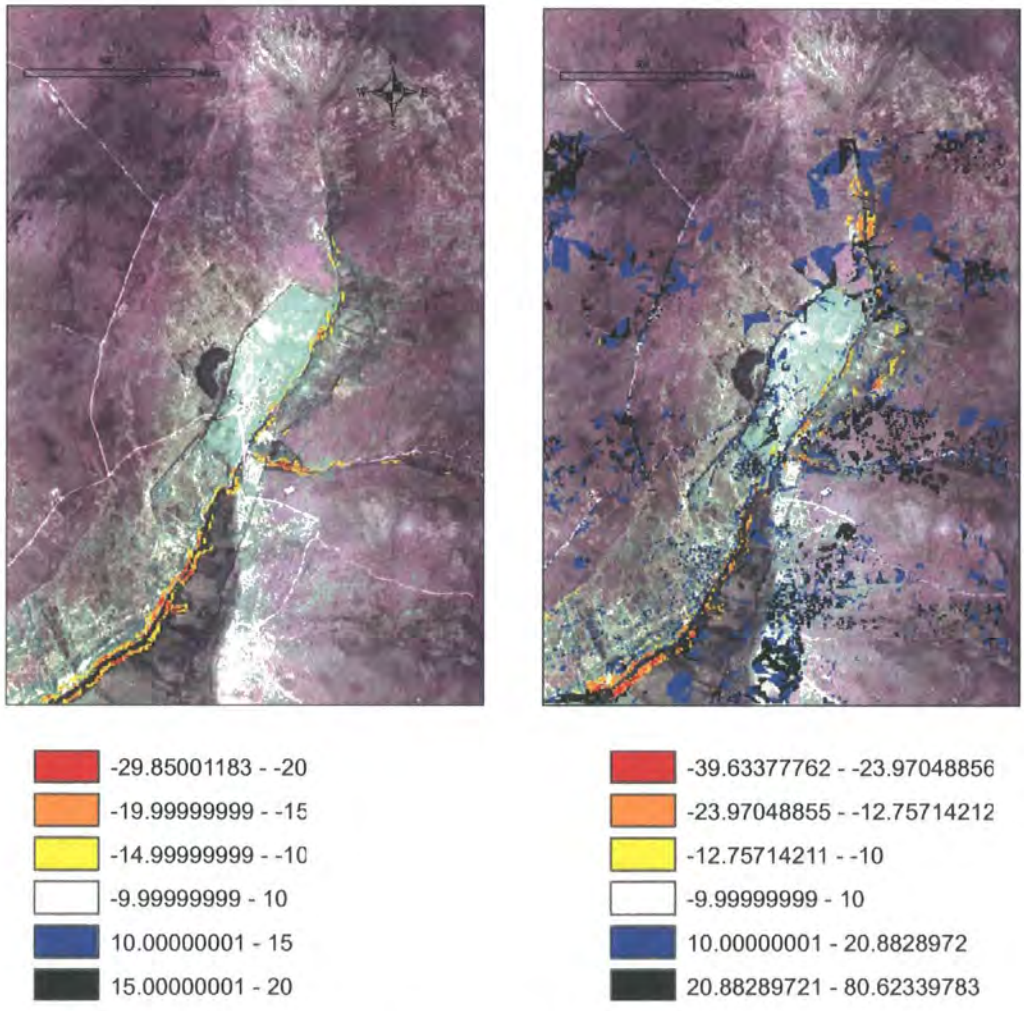

(a) 5 m SAR DEM and 5 m LiDAR DEM **(b) 0.5 m NERC APs DEM and 5 m LiDAR DEM**

Figure 3.40 Slope difference maps from 5 m SAR DEM and 5 m LiDAR DEM (plot (a)) and 0.5 m NERC APs DEM and 5 m LiDAR DEM (plot (b)) of the Head House area with NERC 1:15 000 aerial photographs as background

Fig. 3.40 compares slope from the 5 m SAR DEM and the 5 m LiDAR DEM (plot (a)) and the 5 m LiDAR DEM and the 0.5 m NERC APs DEM (plot (b)). Difference was scaled to six categories represented by different colours and the range of -10 to 10 was set to be fully transparent. Large portions of the Head House area in both plots show differences in slope values and the channels show the largest differences. However, both post-event DEMs show disagreement of 10° to 20° in the peat slide area (on the right side of centre part of the aerial photograph from east to west) and the 0.5 m NERC APs DEM tends to produce higher slopes in most areas, which have different slopes from these two DEMs.

3.7. Discussion

3.7.1. DEM

DEMs were subdivided into three areas, that is the Head House peat slide zone in the northern part and the flood inundation model test area in the southern part of the whole study area and the whole study area, which was a much larger area covering more channels and ground surface. The Head House area and the whole study areas were chosen for all selected topographic parameter analyses and the model test area was only chosen for the Topographic Wetness Index comparison in this chapter. Statistically all DEMs of a same area present a similar patterns in their histograms (Fig. 3.4).

3.7.1.1. Resolution

The representation ability varies significantly with the change in DEM resolution. Decrease in resolution reduced the amount of data points and hence the details of the surface topographic information, especially in both 50 m resolution DEMs from the OS data and SAR images (Fig. 3.5 (b)). In both coarse-resolution DEMs, parts of data were removed during the DEM generation either from OS contour maps or re-sampling procedures from the 5 m resolution SAR DEM. Since the surface in natural environments is continuous in most cases, the elevation values should be continuous as well. Therefore, these two 50 m pixel size DEMs were assumed to be unsuitable for the study at this geographical scale for the Head House area (c. 2.4 km^2). DEM

quality improved from 50 m resolution to 10 m resolution. Finer resolution DEMs provided smaller value in minimum, mean and standard deviation elevation from Table 2.4. However a finer resolution at 5 m did not make much impact on the SAR DEM quality (Fig. 3.5a).

Aliasing is a notable feature in these DEMs. For both DEMs derived from the OS data, the feature results from the digitising procedure of contour maps (Fig. 3.5b). Elevation values were only assigned to the contour lines on paper-based contour maps and values on each pair of the lines were used to interpolate the elevation values in the area between them. When the scale decreases from 1:10 000 to 1:50 000, larger spaces between each pair of neighbouring contours are expected, and hence large areas with no elevation data have to be interpolated. Large spaces produce gaps in elevation and make the 50 m OS DEM unsuitable for representing the surface.

3.7.1.2. Data Source

In addition, DEMs derived from aerial photographs can represent the geomorphological change during the flood and landslide event when compared to the 5 m LiDAR DEM. Both DEMs derived from aerial photographs showed differences in statistics and it is most likely due to the capturing time of aerial photographs. The InfoTerra and NERC aerial photographs were taken before and after the flood event, respectively. The mean elevations in the InfoTerra and NERC DEMs are 334.5 m and 331.8 m respectively with a 2.6 m difference. The minimum elevations are 249.3 m and 242.8 m respectively with a 6.6 m difference. The maximum elevations are 385.0 m and 383.7 m respectively with a 1.4 m difference.

DEMs at the same resolution but from different sources show difference in variation. For example, a SAR DEM tends to have smaller variation than the one from OS data at the same resolution (Fig. 3.9). Both DEMs derived from aerial photographs show similar variations (Fig. 3.6b).

LiDAR data, with a large amount of measurements on the surface supplied us with a great opportunity to investigate the surface topography in more details even from only gridded DEM (Fig. 3.11). The intensity value could be helpful for land-cover or land-use classification where no photographs are available, since different types of ground feature will have different intensity information back scattered. The short collection and processing periods make it possible to monitor an area at a finer temporal scale. Regardless to the high cost, LiDAR is promising in detailed measurements. The raw measurement points can direct to the location which needs further investigations.

In addition, differences between DEMs tend to be minimised with increases in study area (Fig. 3.10).

3.7.2. Slope

3.7.2.1. Resolution

Statistically, the minimum, maximum, mean slope and standard deviation of slope are sensitive to the DEM resolution and kernel size. Minimum slope increases and maximum, mean slope and standard deviation decrease when DEM resolution decreases or kernel size increases. In terms of resolution, for example the minimum slope increases from 0.000° to 0.023°, the maximum slope decreases from 46.6° to 26.4°, the mean slope decreases from 7.6° to 6.8° and the standard deviation decreases from ±6.3° to ±4.9° from the 10 m OS DEM to the 50 m OS DEM respectively of the whole study area using 5×5 kernel size. This trend is more obvious in the Head House area. In terms of kernel size, the minimum slope increases from 0.023° to 0.030°, the maximum slope decreases from 32.3° to 26.7°, the mean slope decreases from 7.1° to 6.6° and the standard deviation decreases from ±5.4° to ±4.8° in the 50 m SAR DEM from using 3×3 to 5×5 kernel sizes. This result is consistent with Zhang and Montgomery (1994), which mentioned that the mean value decreased as the DEM grid size increased. However, it is not true in the Head House area, where the finest resolution DEM, the one from NERC aerial photographs, does not compute the highest maximum slope in Table 3.3 (b). This is

assumed to be the effect of local geomorphological changes during the flood and landslide event. The aliasing in the OS DEMs have impacts on slope calculations.

Zhang and Montgomery (1994) used cumulative frequency distributions of surface parameters to determine the impact of DEM grid size on mean and local values directly. Fig 3.14 shows clearly that the percent of the whole study areas became steeper when the DEMs grid size decreases. This result is consistent with Zhang and Montgomery (1994). However, results turns out to be different in the Head House area, where Fig. 3.15 shows that more areas are steeper in both 10 m resolution DEMs than the 5 m SAR DEM and both DEMs derived from aerial photographs. This difference could be due to three factors. First, it could be the geographical scale of the study area. The whole study area is 260 km^2 while the Head House area is only 2.4 km^2. Second, it could be the DEM data source effect. The finest-resolution DEMs in this study were both derived from aerial photographs and they were original in TIN format. Walker and Willgoose (2006) found the photogrammetrically-derived DEMs were of less accuracy than the cartometric ones for a 1.4 km^2 study area in terms of Root Mean Square Error (RMSE) in elevation and slope. Third, it could be the geomorphological change. The Head House area has experienced some large geomorphological change from the flood and landslides event. Since the aerial photographs were taken after the event, the DEM derived from NERC aerial photographs was designed to represent the surface after the event. The surface change would definitely produce a different DEM.

For the Head House area, maximum value of the OS DEM decreases significantly from 88.5° at 10 m resolution to 21.4° at 50 m resolution (Table 3.5). This indicates that the coarser DEM may ignore details of surface characteristics such as steep slopes. It is also interesting to see that the 5 m SAR DEM calculated lower maximum slope (-50.8° difference) than the 10 m SAR DEM. The 5 m SAR DEM contains more details of surface topography. Zhang and Montgomery (1994) chose a 10 m grid size as the optimum size for the two study sites. The comparison between the 5 m DEM derived from SAR data and the 5 m LiDAR DEM shows difference in river channels where erosion could have taken place during a flood event. As LiDAR data were obtained after the flood, it may suggest that LiDAR data is able to represent the geomorphological change in small geographical scale. Both DEMs

derived from aerial photographs are more similar to the 5 m SAR DEM in cumulative probability.

3.7.2.2. Data Source

Comparison of DEMs of the same area shows slope is highly sensitive to DEM data sources. All results in Fig. 3.18 show the slope differences in river channels or ridges where slope changes significantly. It is not surprising to see the differences from change of kernel size from 3×3 to 5×5 that larger the size of kernel the coarser the resolution. This filters out some details of surface information as shown in Fig. 3.18. In addition Fig. 3.16 shows the other kind of difference in slope in outcrops of resistant strata of the surface. The difference maps become coarser when DEM resolution decreases. However, it does not make much difference when resolution increases from 10 m to 5 m in SAR DEMs as the comparison between the 50 m and the 5 m SAR DEMs and the 50 m and the 10 m SAR DEMs are not able to give any identified differences (Fig. 3.14). This is consistent with the DEM characteristics, where the 5 m and 10 m SAR DEMs show more similar statistics. Using topographic contour maps sourced from the Ordnance Survey brings much noise to the slope maps (Fig. 3.14). DEMs from the OS data and SAR images have different values along the contour lines and hence these lines can be identified when comparing the 10 m OS DEM and the 5 m and 10 m SAR DEMs. It is surprising to find larger agreement between the 10 m OS DEM and the 50 m SAR DEM than the differences shown in comparisons between the 10 m OS DEM and the other DEMs (Fig. 3.14).

3.7.2.3. Algorithm

In terms of the comparison of algorithms, no obvious results can be concluded. Zeverbergen and Thorne (1987), used by the SAGA package provides the smallest standard deviations of local slope than the other two (Table 3.5). The D8 method, used by the Arc/GIS looks less sensitive to the DEM resolution in calculating the maximum slope, but result in much different slopes from the DEM derived from NERC aerial photographs.

3.7.3. Aspect

3.7.3.1. Resolution

Statistically, the minimum, maximum, mean and standard deviations of aspect are all sensitive to resolution (Table 3.6). The minimum and mean aspect increase and maximum aspect and standard deviation decrease when DEM resolution decreases. This is the case in both study areas especially in the Head House area. In terms of resolution, for example, minimum aspect increases from 0.0° to 8.1°, maximum aspect decreases from 360.0° to 347.5°, mean aspect increases from 213.9° to 216.5°, and standard deviation decreases from ±70.0° to ±65.8° from the 10 m resolution OS DEM to the 50 m resolution DEM respectively using 3×3 kernel size. However, between the 5 m SAR DEM and the 10 m SAR DEM of the Head House area, mean aspect decreases from 217.1° to 215.1° and standard deviation increases from ±66.6° to ±67.5° using a 3×3 kernel size. In addition, no significant trend can be seen in terms of kernel size.

Aspect is able to give a good visualisation of surface shape (Fig. 3.21). The 5 m and 10 m SAR DEMs provide similar representation. The 50 m SAR DEM is too coarse to display details like shallow channels. Noises as crop-shape features on the surface exist in the 10 m OS DEM, which also loses details such as representation of local features like walls. Since walls have a potential effect in hydrological processes, OS DEM derived from contour maps is assumed to be more limited for hydrological application.

The comparison shows that aspect is sensitive to DEM resolution. Fig. 3.22 and Fig. 3.24 show at least an 80% aspect difference in areas with large changes in slope in the comparison within SAR DEMs, such as the river channels, where two-direction slopes facing. More aspect differences were introduced on the surface when comparing the 10 m OS and SAR DEMs and the 50 m SAR DEM tends to be the most different from the 10 m OS DEM in aspect. Difference in aspect is less obvious in 2D scatter plots than the result from the ArcGIS shows (Fig. 3.23). One feature is that DEMs tend to contain equal aspect values around 90.0° and 270.0° areas and

this is the case especially within the SAR DEMs, where slope faces the east or the west.

3.7.3.2. Data Source

The OS DEMs and SAR DEMs show similar pattern of distribution and consistent cumulative probability for the whole study area (Fig. 3.24). However, aspect distribution (Fig. 3.23) shows aliasing at about 45° spacing in the 10 m OS DEM and 22.5° in the 50 m OS DEM, especially in areas facing the south in 10 m OS DEM where c. 120000 more points are taken as of aspect of 180.0°. This feature is assumed to be related to DEM source as an edge effect. The OS DEM derived from contour maps are less able to represent continuous areas. In addition, the NERC APs DEM is able to represent the geomorphological change in the Head House area (Fig. 3.24 (a)), where both DEMs derived photogrammetrically from aerial photographs show similar patterns of cumulative probability, which are different from the ones in other DEMs.

3.7.3.3. Algorithm

In terms of algorithm, no significant trend can be seen in the minimum, maximum and mean aspects. The algorithm described in Zeverbergen and Thorne (1987) used by the SAGA calculated one eighth smaller standard deviation than the other two algorithms (Table 3.9).

3.7.4. Profile Curvature

Statistically, profile curvature as a second order derivative is highly sensitive to DEM resolution and kernel size in terms of minimum, maximum and standard deviation. The mean profile curvature is more likely independent to the resolution and kernel size. The minimum profile curvature increases and the maximum profile curvature and standard deviation decrease when DEM resolution decreases or kernel size increases. For example, the minimum profile curvature increases from

-13.3 (°/m) to -1.2 (°/m), the maximum profile curvature decreases from 8.7 (°/m) to 1.8 (°/m) and the standard deviation decreases from ±0.6 (°/m) to ±0.1 (°/m) from the 10 m OS DEM to the 50 m OS DEM using 3×3 kernel size in the whole study area. The minimum profile curvature increases from -13.3 (°/m) to -6.7 (°/m), the maximum profile curvature decreases from 8.7 (°/m) to 4.1 (°/m) and the standard deviation decreases from ±0.6 (°/m) to ±0.3 (°/m) from using 3×3 to 5×5 kernel sizes in the 10 m OS DEM for the whole study area.

Fig. 3.27 shows that local profile curvature is also sensitive to DEM resolution and DEM source. Fine resolution DEMs like the 5 m and 10 m SAR DEMs show clearly the river channels where topography changes much locally. The 10 m OS DEM introduced aspect differences along contour lines. Fig. 3.31 shows additional evidence that the 10 m resolution OS DEM loses local information such as shallow drainage patterns.

In terms of algorithm, the quadratic surface in Evans (1979) used by the ENVI package calculated lower minimum, larger maximum profile curvature and larger standard deviation than the multi-flow algorithm in Zeverbergen and Thorne (1987) used by the SAGA package (Table 3.11). Mean profile curvature seems less sensitive to these two algorithms.

3.7.5. Topographic Wetness Index

Quinn et al. (1995) investigated the impacts of DEM resolution and the calculation of the Topographic Wetness Index for TOPMODEL (Beven and Kirkby, 1979). They showed that the upslope contributing area and flow routing definition have major impacts on calculation of the Topographic Wetness Index. The TWI tends to be different in terms of spatial pattern and statistical distribution for different DEM resolutions and calculation procedures.

Statistically, the Topographic Wetness Index is highly sensitive to DEM resolution. Zhang and Montgomery (1994) found that cumulative probability was affected greatly by grid size of the DEM in terms of mean and local value. The minimum and mean TWI increase and the maximum TWI and standard deviation decrease when

DEM resolution decreases. For example, the minimum TWI increases from -0.7 to 5.7, the maximum TWI decreases from 18.7 to 14.1, the mean TWI increases from 7.4 to 8.1 and the standard deviation decreases from ±1.8 to ±1.1 from the 10 m OS DEM to the 50 m OS DEM for the Head House area. This trend can be noticed in all DEMs excluding the comparison between the 5 m and 10 m SAR DEMs, where the 5 m SAR DEM had larger minimum, mean TWIs and smaller standard deviations than the 10 m SAR DEM in both study areas. This exception is consistent with slope statistics, where the 5 m SAR DEM had lower maximum and mean slopes and standard deviation than the 10 m SAR DEM. Wolock and Price (1994) explained that the impact of DEM resolution on the TWI calculation increased with grid size increases; the minimum effective catchment area and slope decreases with DEM coarseness. Therefore, the statistics of the TWI for the Head House area are consistent with the literature in all DEMs. Fig. 3.35 (a) proves the finding in Zhang and Montgomery (1994) that coarser DEM resolution tended to make cumulative probability distinction towards lower TWI. As shown in Fig. 3.36, the 50 m resolution DEMs are too coarse that lose much detail of the TWI along the river channel in the Head House area. DEMs derived from aerial photographs representation are limited to the original DEM TIN format.

On data source aspect, Fig. 3.36 shows that the TWI is also sensitive to the contour lines from the 10 m OS DEM. The DEMs derived from contour maps give different topographic representation on the contours. In addition, Fig. 3.37, Fig.3.38 and Fig. 3.39 show the InSAR DEMs at different resolutions have different topographic representation in the channels and the TWIs from all other DEMs are either limited to the data or surface crops. Both histogram and cumulative probability are affected more by data source than by resolution (Fig. 3.35). The SAR DEMs had more similar histograms and cumulative probabilities.

3.8. Summary and Conclusion

The DEMs were categorised in three parts according to the areas of coverage: the Head House, at 2.4 km^2, where significant geomorphological change took place; a c.1.5 km^2 area in the lower reach of the River Rye for hydrological modelling; and the third is the largest area covering c. 260 km^2 in the North York Moors. Eight

DEMs were analysed, including two OS DEMs, three InSAR DEMs, two APs DEMs and one LiDAR DEM. They were processed to cover the Head House area while the two OS DEMs and three InSAR DEMs cover the whole study area. A number of key surface parameters, including slope, aspect and profile curvature were calculated using the ENVI 4.1, Arc/GIS, and SAGA packages. Another crucial topographic attribute, the Topographic Wetness Index was acquired for the Head House area and the hydrological model test area using only the SAGA package. An additional LiDAR dataset was acquired more recently and was generated to a 5 m gridded DEM containing a small number of areas between neighbouring strips (e.g. in the Head House area) with no elevation information in them and these areas were analysed after refilling values for both the Head House area and the flood model test area. Results were compared/contrasted with all DEMs.

The results show that topographic attributes are highly sensitive to resolution, kernel size and data source. The main differences in topographic attributes were found in the river channels where measured topography changed significantly, which show implications for hydrological processes. Amongst all the available DEMs of the whole study area, DEMs at the same resolution tend to calculate similar topographic attributes and hence similar representations of surface characteristics. This emphasises the crucial control of resolution. However, results from the 10 m resolution OS DEM were sensitive to digitisation from contour lines. Coarser resolutions generalised surface characteristics greatly and large amounts of information, in particular topographic information, were lost during generalisation. The 5 m resolution InSAR DEM has very different slope estimation and this has impacts on the calculation of the Topographic Wetness Index. Both DEMs derived from aerial photographs though with higher resolution and being able to represent the change of surface topography in the Head House area, did not show clear results in visualisation due to the raw data format.

In terms of algorithms, three different algorithms were used by three different software packages for calculating topographic attributes. The algorithm used by the SAGA (Zeverbergen and Thorne, 1987) produced results with lower standard deviations than the other two. This may imply more precise estimates but it is difficult to generalise from the data available.

A 10 m resolution DEM was considered as the optimum resolution DEM for a similar scale of environmental research by Zhang and Montgomery (1994). The 5 m LiDAR DEM is able to represent the geomorphological change clearly when differenced with both 5 m and 10 m InSAR DEMs. Therefore, the 5 m and 10 m InSAR DEMs as well as the 5 m LiDAR DEM were considered to be the most suitable DEMs for the geomorphological and hydrological research in study area. The next chapter investigates the impact of topographic representation on hydrological response through a hydrological application to the study area.

4. Flood Inundation Modelling

4.1. Introduction

Topography has an important impact on hydrological processes (e.g. flooding) (Lane et al., 1998). Chapter 3 concluded that DEMs at different resolutions and from different data sources had different topographic parameters and hence represented detailed topography differently in the study area. This chapter investigates the impact of resolution and data source on hydrological processes, specifically valley flooding. The Environment Agency have a flood inundation model based on the SAR DEM for the extreme flood event that happened on the River Rye in the North York Moors during the summer of 2005. Aerial photographs taken four days after the event provided a good opportunity to identify the maximum flood extent. Therefore, the latter dataset can be utilised as independent data for validation of the flood inundation model for the particular event in terms of maximum flood inundated area. In addition, the EA numerical model was validated through comparison of model results with flood extent observations. The EA model has predicted 93.2% of the inundation areas, which were derived from the NERC aerial photographs. This chapter aims to assess the impact of different resolution and data sources of DEMs upon the flood inundation extent prediction using a FLOWMAP 2D model.

4.2. Research Issues

Determining the maximum extent of a flood is a highly important issue among river engineers and field managers (Penning-Roswell and Tunstall, 1996). Ground-based observations are normally limited and so numerical modelling of environment fluid dynamics has been widely adopted (Bates and De Roo, 2000). Horritt and Bates (2001) compared a raster-based model and a finite-element model for a 4 km reach of the upper Thames in the UK using SAR imagery for validation. They concluded that both models offered similar performance in terms of flood extent prediction. The raster-based model needed less calibration. Less focus was put on comparison of the input topographic data sources and their resolutions. In addition, topography, friction and turbulence characteristics make even the simplest application of great complexity in modelling (Marks and Bates, 2000). For example, Bates and De Roo

(2000) concluded that complexities in flood inundation prediction in meandering compound channels meant that predictions will be highly dependent on topography and small errors in simulated water surface would cause large errors in inundation area. Bates et al. (2003) conducted a 1 in 4 year flood event on a 12 km reach of the River Stour in Dorset, UK using a control simulation with a mesh developed independent of topography and two other simulations with a topographically optimum mesh and the topographically optimum mesh incorporating a sub-grid topographic data respectively. It was found that the sub-grid topographic data derived from LiDAR had great impact on model behaviour. Numerical models have become available for dealing with more complex boundary conditions for geomorphology and hydrology since 1990 in particular (Bates and Lane, 1998). Bates et al. (2006) mapped a flood inundation along a similar to 16 km reach of the River Severn, UK using 1.2 m resolution airborne-SAR imagery and found the measured floodplain topography gave a new insight to the factors controlling the predicted inundation pattern at different scales. The floodplain topography acts as an important factor in determining the inundation pattern in flood inundation modelling and topographic data from different sources/at different resolutions will give different topographic representation on floodplains. Highly developed remote sensing techniques (e.g. SAR and LiDAR) provide us a variety range of high-quality topographic data. Therefore, further investigation is needed with into the topographic representation from these high-quality topographic data.

Various models have been developed following from improvements in computation since the early 1980's. These range from one-dimensional (1D) models (such as 1D finite difference solutions of the full St. Venant equations in Fread (1984) and Fread (1993)) to two-dimensional (2D) models (such as 2D finite difference and finite element models in Bates et al., 1992 and Bates et al., 1995) 2D models are able to overcome a number of general limitations of 1D models such as poor representation of areas between cross-sections. In principle, three-dimensional (3D) Navier Stokes Equations govern the flow processes, which alters the Reynolds averaging. The depth-averaged models utilise the 3D Navier Stokes Equations after depth are integrated. The diffusion-wave equations are produced after ignoring the inertial terms in 3D Navier Stokes Equations. With a four parts discretisation, former equations turn to base on raster and hence makes raster-based 2D model available.

The increasingly available high resolution and high accuracy DEMs have helped the development of 2D flood inundation modelling in UK and the Netherlands etc. (Bates and De Roo, 2000). Furthermore, using raster-based models will be more beneficial in ease of formulation, efficiency in computation, and simplicity in calibration. Results from existing 2D inundation models show good predictive ability for flood inundation extent in both depth-averaged and diffusion-wave models (Yu and Lane, 2006a). Yu and Lane (2006a) showed that a 2D flood model based upon diffusion-wave treatment was highly sensitive to local topography in terms of: (1) the resolution of input topographic data; (2) flow-routing representation; and (3) the combined effects of (1) and (2) on water stage and velocities. Yu and Lane (2006b) developed and tested a sub-grid wetting and drying correction for the 2-D diffusion-wave model and showed that representations of sub-grid using roughness parameters were not able to provide adequate representation of the structural elements on floodplains. Therefore, the experiment utilised the 2D diffusion-wave model from Yu and Lane (2006a) for assessment the impact of topographic data on flood extent prediction through modelling.

4.3. Topographic Data Comparison for Flood Inundation Modelling

4.3.1. Model Description

The numerical model used in this study was based on the complex topography flood model FLOWMAP used in Yu and Lane (2006a), and developed for the purpose of the maximum flood extent estimation in the North York Moors. With the permission of the authors, the original java coded application was employed for a better visualisation of results and the description of the model is based on Yu and Lane (2006a). The principle equations of the model are derived.

River and floodplain flows are governed by the vector sum of several forces, which include gravity and friction forces. Gravity leads the water to flow in the direction of the steepest water surface slope. Friction forces the water in the exact opposite direction of the flow at each point. Friction and gravity effects become proportionally smaller for deeper flows where inertial effects become more

important due to the increase in water mass. The basic principles on river flow follow from conservation of mass and momentum (Lane, 1998). Well known hydraulic equations such as Manning's equation and the St Venant equations (and various derivatives thereof, such as the diffusion-wave equation) represent some or all of these factors. When the bankful water depth was reached in the channel, flow started to move towards the shallow slope on floodplains and caused flood inundation. Consider the depth-averaged form of the Navier-Stokes conservation equation for momentum with a Manning type friction law to represent the associated friction sink term:

$$\frac{DV}{Dt} + (V \cdot \Delta)V + g\Delta(z_0 + d) + \frac{n^2 g V|V|}{d^{4/3}} = 0 \qquad \textbf{Equation 4.1}$$

where V is the velocity vector in the depth-averaged river channel, t is the simulation time in this model, z_0 is the river channel bed elevation, d is the flow depth, g is the gravity constant, and n is Manning's n. In this case, a sum of channel bed elevation and flow depth were input as a stage h. The next step is to make a diffusion wave approximation by ignoring the acceleration terms: the first two terms on the left of equation 4.1. This is assuming that the temporal acceleration within a time step (time step is described in equation 4.15) is negligible. Divided through by g, equation 4.1 becomes:

$$V|V| = -\frac{d^{4/3}}{n^2}\Delta(h) \qquad \textbf{Equation 4.2}$$

Equation 4.2 can be rearranged to solve for the velocity magnitude |V| through:

$$|V| = \frac{d^{2/3}}{n}|\Delta(h)|^{1/2} \qquad \textbf{Equation 4.3}$$

Substitution of equation 4.3 into equation 4.2 and rearranging gives:

$$V = -\frac{d^{2/3}}{n}\frac{\Delta(h)}{|\Delta(h)|^{1/2}} \qquad \textbf{Equation 4.4}$$

Given that

$$Q = wdV \qquad \textbf{Equation 4.5}$$

where Q is vector discharge and w is the DEM grid spacing:

$$Q = -\frac{wd^{5/3}}{n}\frac{\Delta(h)}{|\Delta(h)|^{1/2}} \qquad \textbf{Equation 4.6}$$

Taking the absolute value of equation 4.6 and dividing through by w gives Q per unit width:

$$Q = \frac{d^{5/3}}{n}\frac{(S_x^2+S_y^2)^{1/2}}{(S_x^2+S_y^2)^{1/4}} = \frac{d^{5/3}S^{1/2}}{n} \qquad \textbf{Equation 4.7}$$

where S is the absolute value of the vector slope.

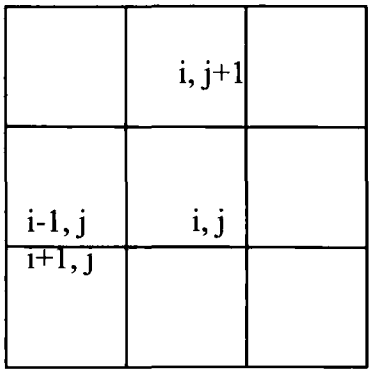

Figure 4.1 Regular grid cells

Fig. 4.1 shows the regular cell with (i, j) as termed name and its four adjacent cells in orthogonal directions with names of (i+1, j), (i, j-1), (i-1, j), and (i, j+1) distributed clockwise from the cell's right hand side.

The slope in each orthogonal direction is termed as the water level difference between two adjacent cells divided by the distance between their cell centres (Equation 4.8 and 4.9).

$$S_i = \frac{h_{i,j} - h_{i\pm1,j}}{w} \qquad \textbf{Equation 4.8}$$

$$S_j = \frac{h_{i,j} - h_{i,j\pm1}}{w} \qquad \textbf{Equation 4.9}$$

After the slope S is calculated, this is applied to equation 4.7. Hence the absolute flow Q in i and j directions of the grid can be described as

$$Q_i = \frac{d^{5/3}S_i}{nS^{1/2}} = \frac{d^{5/3}\left(\frac{h_{i,j} - h_{i\pm1,j}}{w}\right)}{n\left[\left(\frac{h_{i,j} - h_{i\pm1,j}}{w}\right)^2 + \left(\frac{h_{i,j} - h_{i,j\pm1}}{w}\right)^2\right]^{1/4}} \qquad \textbf{Equation 4.10}$$

$$Q_j = \frac{d^{5/3} S_j}{nS^{1/2}} = \frac{d^{5/3}\left(\frac{h_{i,j} - h_{i,j\pm1}}{w}\right)}{n\left[\left(\frac{h_{i,j} - h_{i\pm1,j}}{w}\right)^2 + \left(\frac{h_{i,j} - h_{i,j\pm1}}{w}\right)^2\right]^{1/4}} \qquad \textbf{Equation 4.11}$$

where Q_i and Q_j are the flow in i and j direction, Q is the vector sum of flow. Water flows into or out of a cell only once in each time step. Equations 4.10 and 4.11 calculate the fluxes into or out of each cell. The change of water depth in cell (i, j) in each time step is calculated by Equation 4.5 as

$$\Delta d = \frac{(\sum_{D=1}^{4} Q^D_{in(i,j)} - \sum_{D=1}^{4} Q^D_{out(i,j)} - Q_{\text{in}\,flow})\Delta t}{w} \qquad \textbf{Equation 4.12}$$

where Δ_d is the change in water depth, Q accumulates from D=1 to D=4 represents the flow from all four orthogonal directions, $Q_{in(i,\,j)}$ means the flow into the cell, $Q_{out(i,\,j)}$ means the flow out of the cell (i, j), Q_{inflow} means the flow already in the cell before any flow comes into or out of the cell, and Δ_t (s) represents the time step.

In this application, water depth in a cell is set to be the same value as the average water depth all over the cell. However, two issues should be noted here. First, when a dry cell receives water for the first time, only part of the cell may be wetted in a time step. Therefore, the flow will diffuse more quickly across the floodplain than it should do if the whole cell is set to be wetted as the average water depth. Second, in addition, if the outflow is larger than the sum of inflow and water already in the cell, Δ_d in Equation 4.12 becomes negative, and hence d in Equation 4.6 would be 0 or even a negative. Zero (0) means the cell turns totally dry while a negative value in water depth is not acceptable in reality. Furthermore, partly wetted cells should be processed carefully to prevent any isolated sink in the river. For these issues, Bradbrook et al. (2004) introduced a wetting parameter %wet (in percentage) and specified a minimum water depth and no outflow was allowed below this depth. This parameter leads to a situation that parts of the inundated floodplain could remain wet if the connectivity in river and floodplain is not maintained. The wetted parameter is calculated as

$$\%wet = \min(1, \frac{v\Delta t}{\Delta x}) \qquad \textbf{Equation 4.13}$$

where V (m/s) is the water velocity in equation 4.1. Δx is the distance in direction of V within the cell boundary. The wetting parameter %wet is updated to each time step Δ_t, and water is only allowed to flow out a cell when the wetting parameter is one, which means flow in the cell travels over the distance within the cell (Δ_x) in the time step Δ_t. In addition, a minimum water depth is set for both wetting and drying procedures (Bradbrook et al., 2004). The sum of the net inflow and outflow is recalculated at each time step. In this case, the outflow is scaled by a drying factor d_f, in case the water depth is reduced to the minimum water depth. This is to keep the mass conservation during drying procedure over the floodplain. d_f is defined as

$$d_f = \frac{w^2(d - d_{\min})}{\sum_{D=1}^{4} Q^D_{in(i,j)} - \sum_{D=1}^{4} Q^D_{out(i,j)} - Q_{\text{in flow}}} \qquad \textbf{Equation 4.14}$$

In this application, the minimum water depths for wetting and drying procedures were set to 0.05 m and 0.02 m respectively. Their impact on modelling is evaluated in the following section.

Courant et al. (1928) noted the time step should be less than the time flow travels through a cell. When the time step is longer than the travel time, the change of water depth, Δ_d may not able to adjust itself in time to represent reality fully. The time step should be determined by

$$\Delta t \leq = \frac{w}{v + \sqrt{gd}} \qquad \textbf{Equation 4.15}$$

Maximum values are used to determine the next time step as

$$\Delta t = \frac{w}{\max(v) + \sqrt{g \max(d)}} \qquad \textbf{Equation 4.16}$$

Yu and Lane (2006a) note that Equation 4.16 needs to be developed to ensure the Courant–Friedrichs–Lewy condition (CFL condition) is satisfied. Therefore a Courant number is calculated as

$$\textbf{Courant number} = \frac{(v+\sqrt{gd})\Delta t}{w} \qquad \textbf{Equation 4.17}$$

The Courant number is calculated each time step. After applying Equation 4.16 to equation 4.17 using the maximum Δt, two possible results could arise: 1) if the maximum Courant number is greater than one, scale the result by factor f; in this application, f was set to be 0.8; and 2) if the maximum Courant number is smaller than one, the time step is recalculated by

$$\textit{time step}^{t+1} = \textit{time step}^{t+1}\ \textbf{(from Equation 4.16)} \times \textbf{0.8/max (}\text{Courant }\textbf{number)} \qquad \textbf{Equation 4.18}$$

An additional procedure is required on the domain boundary. Yu and Lane (2006a) used an output from a one dimension (1D) hydraulic model to simulate the flow diffusion from river channel over the protection wall into the floodplain. This process would be assessed continuously along the river bank using

$$q = 1.704(H - \Delta z)^{3/2} \qquad \textbf{Equation 4.19}$$

where q is the flux from river channel over the embankment through the floodplain, H is the water surface elevation at the contact point beside the floodplain, and Δ_Z is the ground elevation at the contact point on the embankment.

Equation 4.19 was applied to all adjacent points along the river channel and inundation allowed to occur once river surface elevation was higher than ground elevations at the contact point on the embankment. Since the water surface elevation on both sides of the river should be the same, differences in ground elevation on embankments of both sides may exist. Brandbrook et al. (2004) chose to set the water depth on one side of the river to the value of the adjacent cells when the other side of the river met the condition to flow out. Therefore, the water surface slope on the boundary of the other side should be the same as the river bed slope across the

boundary. If this setting led to a reverse water slope, the other side of the river was set to the same function.

4.4. Model Operation

4.4.1. Model Set-up

4.4.1.1. Model Operation Environment

The model was operated on a Pentium IV Workstation with double Intel® 4 3.00 GHz CPUs and 2.00 GB RAM in the Microsoft Windows XP SP2 system environment in the GIS/Remote Sensing lab in the Department of Geography, University of Durham.

4.4.1.2. Data Requirements

Bates (2004) summarised four key data items in numerical flood inundation modelling.

First, topographic information is traditionally gathered from costly and time consuming ground survey with cross-sections perpendicular to the river channel. Recently, this information was been derived from digitising paper-based topographic maps such as a contour map but with low accuracy with poor spatial resolution in floodplains, e.g. 5 m spacing to ±1.25 m accuracy in height in the UK (Bates, 2004). Currently, various remote sensing techniques have become available for generating topographic information, such as from SAR imagery (Bates and De Roo, 2000; Horritt et al., 2004), aerial photographs (Lane et al., 2000), and LiDAR data (Marks and Bates, 2000; Yu and Lane, 2006a). Such high quality topographic data are used in this application and the datasets have been described in Chapter Two.

Second, bulk flow data are usually obtained from gauging stations measurement locally. The data for this study were provided by the Environment Agency.

Third, effective friction parameter values are required. This parameter is usually calibrated according to different topographic datasets. Cobby et al. (2003) used an image segmentation system to convert the LiDAR height image into surface topography and vegetation height separately and hence estimated the friction in channels and floodplains at each mesh node on physical base.

Finally, validation data are needed. According to Bates (2004), the overly-large spacing of gauge stations does not allow the validation of hydrological models. Lane et al. (2003) noted that water level recorders may not be able to record the highest inundation level during an extreme flood event automatically due to instrumentation problems. For this problem, two possible solutions were explored. The first method combines high-resolution elevation data, such as a DEM and planimetric data information e.g. visible wrack lines on aerial photographs. The second one employed a photogrammetric approach with aerial images flown after a flood event used to estimate the elevations of visible wrack lines on these images. Both results were assessed with check data from LiDAR and the latter method was more reliable in relation to the quality of LiDAR data and uncertainties in the photogrammetric approach. A numerical flood inundation model based on SAR imagery was operated by the Environment Agency to predict the maximum flood inundation extent for the flash flood in summer 2005.

4.4.1.3. Input Data

Assuming the vegetation impact on flood flow was constant as a function of slope in this small scale test area, floodplain roughness coefficient and initial implicit time step were set to 0.06 units and 4 seconds, respectively and model was operated to simulate the hydrological processes for the 5 hours from 16.15 to 21.15 GMT on 19th June 2005. Inundation area visualisation and model operation were set to predict every 300 seconds and 100 seconds, respectively. Boundary flow and flow back to river were allowed. Boundary slope and the minimum depth of wetness were set to 0.01 m/m and 0.001 m respectively. The unfiltered 5 m LiDAR DEM of the modelling area was set to be the background for visualisation. The river channel and floodplains were treated separately. The river channel shape was clipped out from

each DEM and then used to create a grid at the same resolution as the corresponding DEM for representation of the boundary of the channel. The elevation of the river channel in the original DEM was set to zero. Therefore, the floodplains and the river channel were created to be two grids as two layers. In this case for the area tested, water levels in the whole river channel had zero slope and were driven by stage data. The river bed elevation was added to the stage data to create a stage elevation above sea level. The zero slope is acceptable over the spatial extent of the modelled area, which was only c. 2 km.

To make full use of the dataset, higher, artificial river stage data were created to explore the relationships between inundation area and larger flood magnitudes. The original stage data from the gauging station only contained the stage before the station was damaged by flood flow, which was the stage data before 17.30 GMT (including) on 19th June 2005. To remain consistent with the original data, all stage value from 17.45 GMT to 21.15 GMT were set to the value at 17.30 GMT in each dataset. Artificial stage dataset 1, 2 and 3 are named as AS1, AS2 and AS3 for reference in later sections of this chapter. The AS1 was set to create a regular increasing stage from 92.000 m. The stage was set 1 m higher after each 15-minute period and created a maximum stage of 97.000 m at 17.30 GMT on 19th June 2005. The AS2 was set to create a slower increase in the early half of the stage increase period and faster increase in the latter half. This setting was done to create a stage increase pattern that reflected reality (the original stage data) but at a larger magnitude. The AS3 was set to be with a 0.5 m lower stage than the AS2 in each time period.

Table 4.1 Stage data in 15 min spacing from 16.15 to 17.30 GMT on 19th June 2005

Time (GMT on 19th June 2005)	16.15	16.30	16.45	17.00	17.15	17.30
Original stage data (m)	92.568	92.572	92.598	92.716	93.573	94.607
Artificial stage dataset 1 (m)	92.000	93.000	94.000	95.000	96.000	97.000
Artificial stage dataset 2 (m)	92.000	92.500	93.000	94.000	96.000	98.000
Artificial stage dataset 3 (m)	92.000	92.000	92.500	93.500	95.500	97.500

Table 4.1 summarises the original stage data from gauge station and three artificial stage datasets in 15-minute period from 16.15 GMT to 17.30 GMT on 19th June 2005.

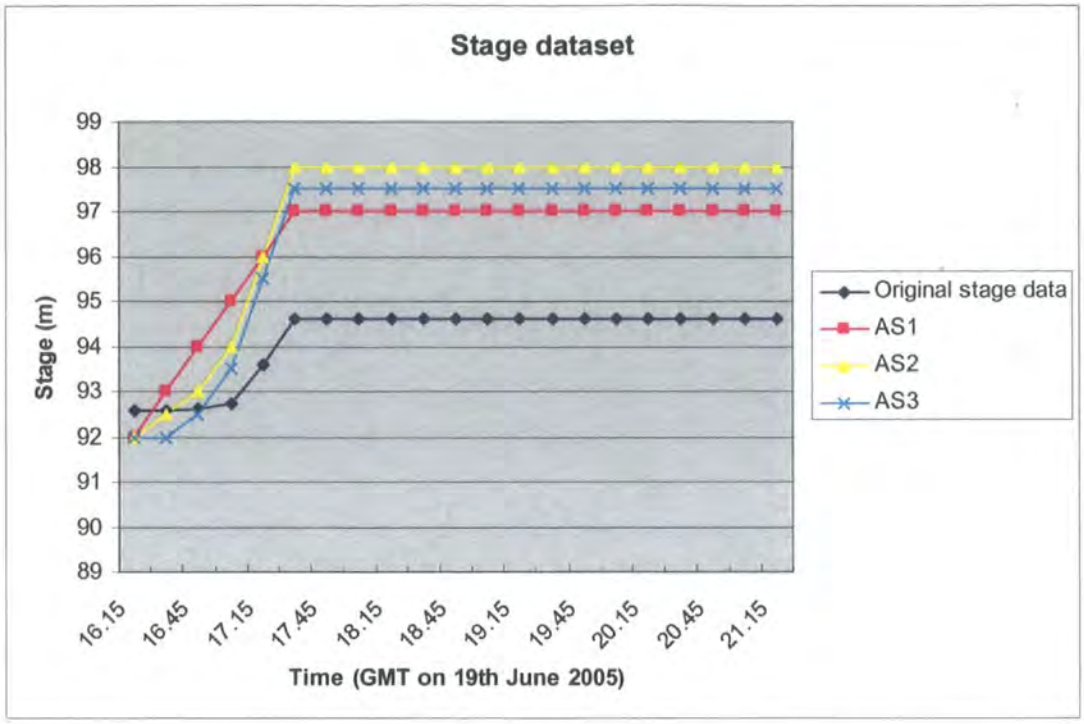

Figure 4.2 Stage data at the Broadway Foot gauging station on the River Rye through time

Fig. 4.2 shows the changes in stage value through time. The stage was kept the same as the value from 17.30 GMT in all the four datasets. During 17.30 GMT and 17.45 GMT on 19th June 2005 the Broadway Foot gauging station was destroyed by flood flow and was unable to record any stage afterwards. To simulate a larger inundation area than the prediction from the original stage data, all artificial datasets show a quicker increase in stage value. In addition, artificial dataset 2 and 3 kept a 0.5 m difference during the simulation.

Five DEMs, including the filtered and unfiltered LiDAR DEMs, the 5 m and 10 m SAR DEMs and the 10 m OS DEM, were utilised as input topographic data in this model test and their boundary is summarised in the Table 4.2.

Figure 4.3 Model test area DEMs and aerial photograph from left to right ((a) Filtered 5 m LiDAR DEM; (b) Unfiltered 5 m LiDAR DEM; (c) 10 m OS DEM; (d) 5 m SAR DEM; (e) 10 m SAR DEM; (f) Aerial photograph)

Fig. 4.3 shows five DEMs of the model test area ranging from 80 m to 150 m in elevation and the 1:15 000 aerial photograph of the test area. The DEM include (a) filtered 5 m LiDAR DEM, (b) unfiltered 5 m LiDAR DEM, (c) 10 m OS DEM, (d) 5 m SAR DEM and (e) 10 m SAR DEM.

Both SAR DEMs are shown to have higher values of elevation generally. The original 5 m LiDAR DEM was filtered with an algorithm in the MicroStation package to remove the measurements of vegetations. The algorithm was described in Chapter Two, so that it is not explained more here. The filtered LiDAR DEM greatly decreased the effects of trees on floodplains. Depression of water, inundation extent can be recognised from the aerial photograph. River channels can be noticed on all DEMs excluding the 10 m OS DEM. The dark parts along the river channel are assumed to be the floodplain.

Table 4.2 Model test area statistics in British National Grid

	Min. X	Max. X	Min. Y	Max. Y
Aerial photograph	455853.989	456143.989	488086.570	488516.570
Filtered 5 m LiDAR DEM	455851.500	456146.500	488083.800	488518.800
Unfiltered 5 m LiDAR DEM	455851.548	456146.548	488083.797	488518.797
10 m OS DEM	455846.546	456156.546	488073.755	488523.755
5 m SAR DEM	455851.545	456146.545	488083.888	488518.888
10 m SAR DEM	455854.046	456144.046	488086.430	488516.430

Table 4.2 summarises the boundary statistics of the DEMs and aerial photograph. Small bias exists in different DEMs due to the impact of grid size and DEM location.

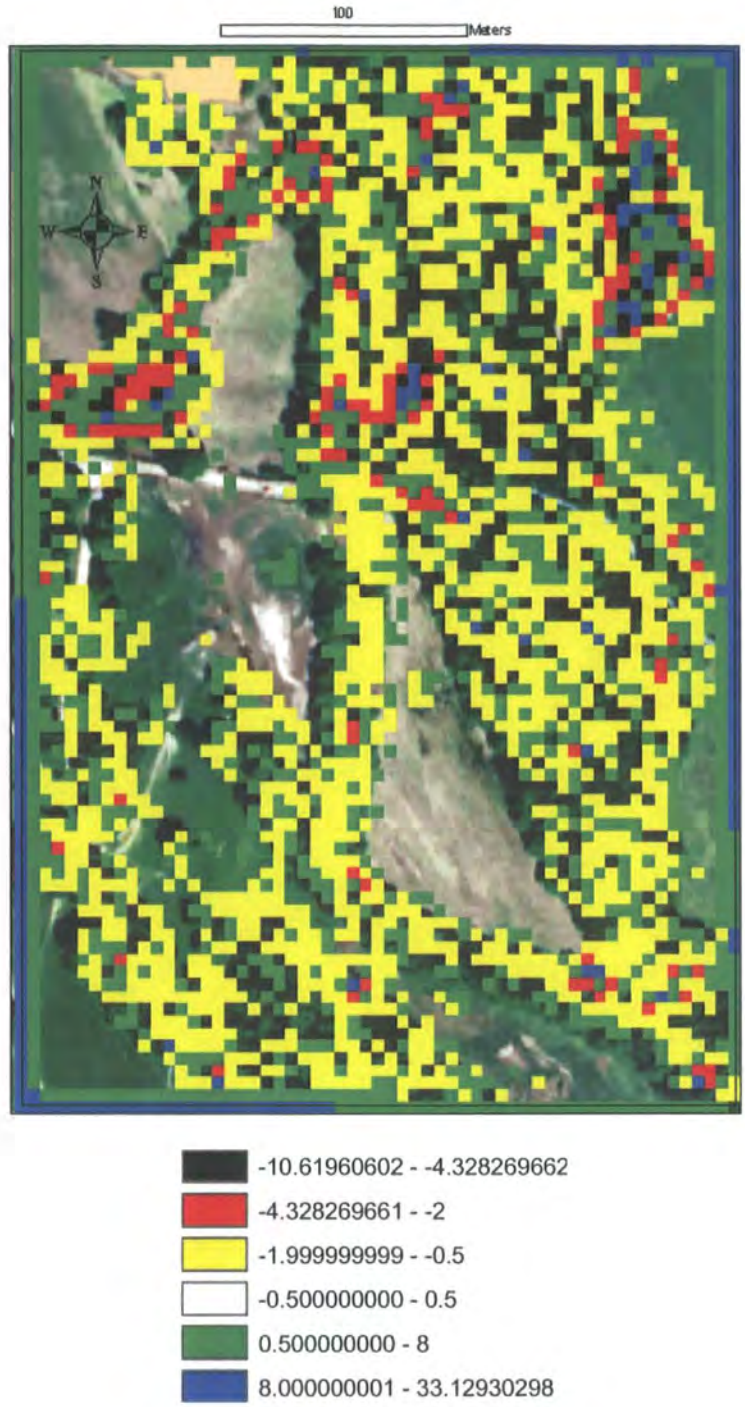

Figure 4.4 Elevation difference between the unfiltered LiDAR DEM and the filtered LiDAR DEM of the model test area

Fig. 4.4 shows the elevation difference between the unfiltered 5 m LiDAR DEM and the filtered 5 m LiDAR DEM of the model test area (areas within the black square) and the difference was categorised to six types where the areas with differences fewer than 1 m set to be transparent. The red and yellow show the areas where the unfiltered LiDAR DEM has larger elevation values than the filtered LiDAR DEM.

These areas mainly represent the trees in the model test area, which indicates that the filter algorithm successfully removed the measurements on trees from the raw data. Limited areas with a lower elevation from the unfiltered LiDAR DEM are assumed to be the interpolation errors from the LiDAR DEM after being filtered. Large differences on edge of the test area also show significant interpolation errors on the image edges.

Figure 4.5 Filtered LiDAR measurements distribution in the model test area

Fig. 4.5 shows the filtered LiDAR measurements distribution in the model test area. Each brown point is a measurement assumed to be from the ground surface and these measurements were interpolated to create the filtered 5 m LiDAR DEM.

(a) filtered DEM **(b) unfiltered DEM**

Figure 4.6 5 m interval contour map derived from the filtered 5 m LiDAR DEM (a) and the unfiltered 5 m LiDAR DEM (b) in the flood model test area

Fig. 4.6 shows the filter effects on removing trees on the floodplains through contrast the 5 m interval contour lines derived from the filtered and the unfiltered 5 m LiDAR DEMs. The filter removed major trees which are shown in plot (b) as circles. The bridge was shown in both contour maps and has a blockage effect on flood inundation. Fig. 4.5 and Fig. 4.6 confirm that few measurements were counted in the areas with trees and that the majority of the floodplain was measured intensively to create a high-precision DEM with a high confidence.

4.4.2. Model Results

Both unfiltered and filtered 5 m resolution LiDAR DEMs, both InSAR DEMs and the 10 m OS DEM were input as topography to the model for prediction of flood inundation area stimulating for an flood event of five hours. All results are categorised by flooding extent. The first part of this section demonstrates the comparison for DEM source/resolution impact on model response in terms of flood

inundation area. The second part of this section investigates the effect of filter algorithm and Manning's n on model response.

4.4.2.1. Data Source/Resolution Impact

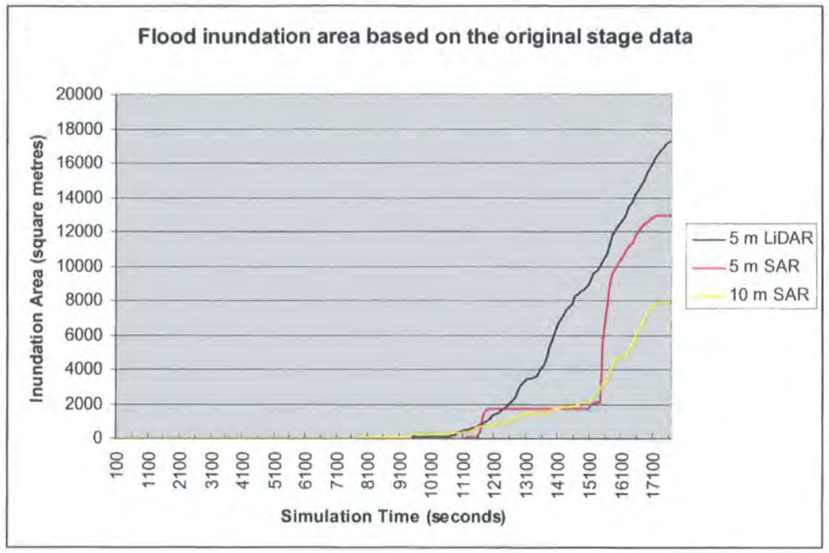

(a) Original stage data

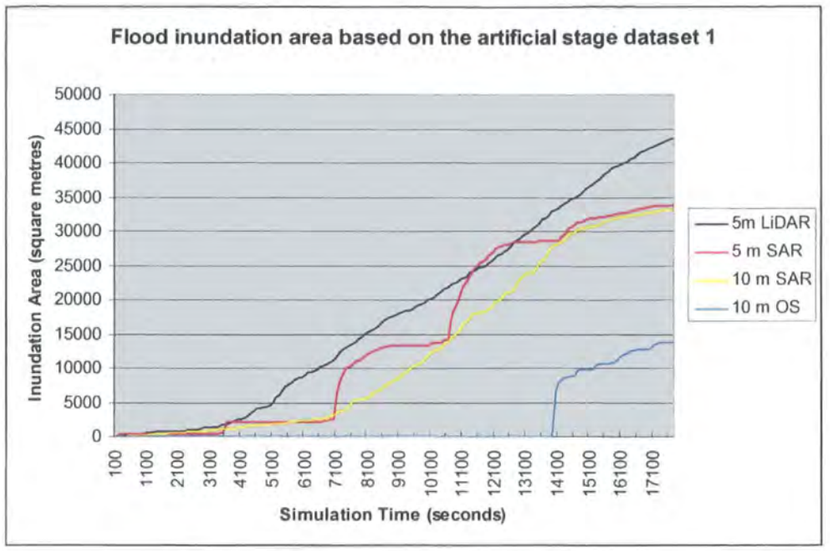

(b) Artificial stage dataset 1

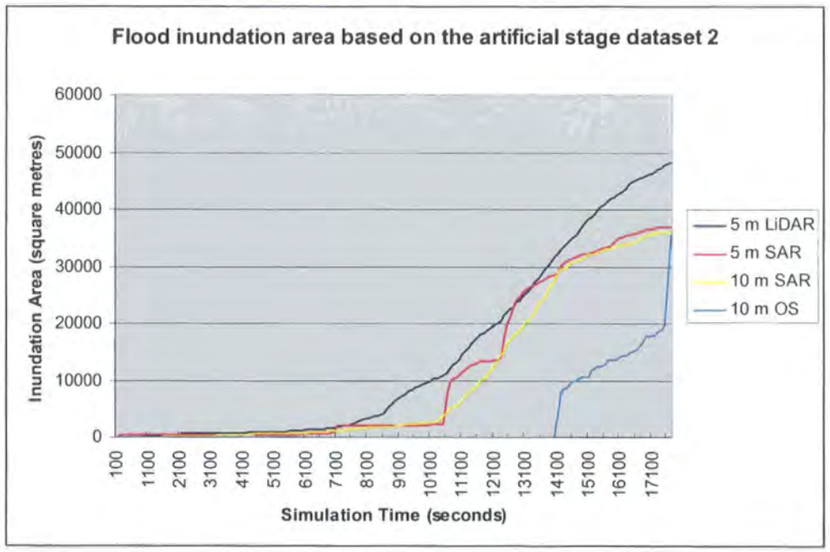

(c) Artificial stage dataset 2

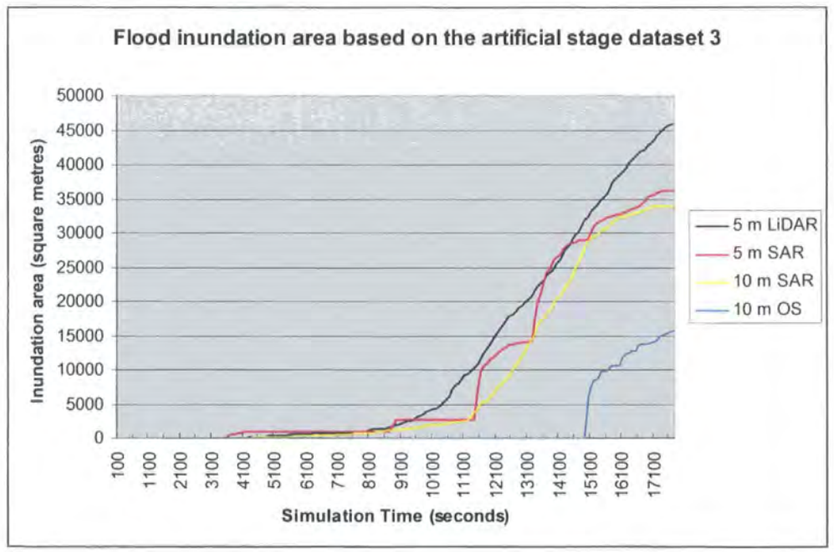

(d) Artificial stage dataset 3

Figure 4.7 Model results of flood inundation area from (a) the original stage data, (b) the artificial stage dataset 1, (c) the artificial stage dataset 2 and (d) the artificial stage dataset 3

Fig. 4.7 shows the model results for inundation area change through model simulation time. X-axis represents the simulation time in seconds and y-axis represents the inundation area in square metres. The plots (a), (b), (c) and (d) compare the results from the unfiltered 5 m LiDAR DEM, both SAR DEMs and the 10 m OS DEM in four different flooding events separately.

For each DEM, simulated inundation increases are similar for all flood events. The unfiltered 5 m LiDAR DEM simulated the largest flood inundation area in all cases. The 5 m SAR DEM simulated slightly larger inundation area than the 10 m SAR DEM with the smallest inundation area predicted by the 10 m OS DEM. For the event simulated based on the gauging data, the OS DEM was unable to predict any inundation during the five-hour simulation.

For the results from the 5 m SAR DEM, a number of characteristics are summarised.

First, sudden increases in area are predicted by the 5 m SAR DEM. Inundation experienced three sudden increases in the results in all flood events while this kind of increase happens only twice in the result based on the original stage data which simulated a much smaller inundated extent.

Second, the sudden increase occurred at about 11 500 s and 15 500 s after in the 'real' flooding event while they happened at 3 500 s, 7 000 s and 10 500 s in artificial flood event 1, 7 100 s, 10 500 s and 12 100 s in artificial flood event 2 and 8 150 s, 11 500 s and 13 200 s in artificial flood event 3.

Third, the increase in area was the same at c. 3 000 m^2, 11 000 m^2 and 30 000 m^2, for the three increases respectively. The 5 m SAR DEM was unable to simulate a third sudden increase in the 'real' flooding event. In all cases, the sudden inundation increases started when the results from both SAR DEMs met. This finding suggests that the 5 m SAR DEM has a quicker response than the 10 m SAR DEM in each stage of inundation area increases.

The 10 m OS DEM started to predict inundation area after 14 000 s in all artificial flooding events which is much later compared to results from other DEMs. Similar

to the 5 m SAR DEM, the 10 m OS DEM saw an increased peak at a very early stage in its inundation simulation in all cases.

Both the unfiltered 5 m LiDAR DEM and the 10 m SAR DEM had a more stable increase style during the whole 5 hour period in all flooding events. Compared to the 5 m LiDAR DEM, the 10 m SAR DEM predicted a larger inundation area increase in early stages of the simulation and a smaller inundation increase in later stages of the simulation.

Table 4.3 Maximum inundation area in square metres from four DEMs based in all flooding events

DEM / Stage datasets	5 m LiDAR DEM	5 m SAR DEM	10 m SAR DEM	10 m OS DEM
Original stage data	17275	12950	7900	0
Artificial stage dataset 1	43475	33775	33100	13800
Artificial stage dataset 2	48150	36850	36100	35500
Artificial stage dataset 3	45800	36350	34000	15600

Table 4.3 summarises the maximum inundation area in square metres based on four stage datasets. The 10 m OS DEM failed to derive any inundated area for the original stage data but simulated flooding in all three artificial events. The 5 m LiDAR DEM calculated the largest area of inundation in total during the simulation period based on all stage datasets followed by the 5 m SAR DEM, the 10 m SAR DEM and the 10 m OS DEM. Both SAR DEMs showed little difference compared to the differences from other DEMs. For example, the difference between SAR DEMs showed in the first flooding event with only 665 m^2 larger inundation area from the 5 m SAR DEM while the 5 m LiDAR DEM predicted almost 10 000 m^2 more inundation than the 5 m SAR DEM in the same flood event.

Flood inundation area statistics were calculated in Microsoft® Excel from the summary files generated in each simulation. The results of unfiltered LiDAR DEM, both SAR DEMs and the 10 m OS DEM are compared below. The 95% percentile and 5% percentile of the inundation area represent the inundation area value which is larger than 95% and 5% of all the values during the 5 hour simulation, respectively.

Table 4.4 Flood inundation area statistics from the original stage data and three artificial datasets (scenarios)

Datasets	DEM	5 m LiDAR DEM	5 m SAR DEM	10 m SAR DEM	10 m OS DEM
Original stage data	Mean flood inundation area (m^2)	2874.29	1792.898	1121.023	0
	95% percentile of flood inundation area (m^2)	0	0	0	0
	5% percentile of flood inundation area (m^2)	14725	12318.75	6625	0
Artificial stage dataset 1	Mean flood inundation area (m^2)	18333.38	14875.99	12819.32	2400
	95% percentile of flood inundation area (m^2)	606.25	350	200	0
	5% percentile of flood inundation area (m^2)	41787.5	33456.25	32625	12800
Artificial stage dataset 2	Mean flood inundation area (m^2)	14309.04	11404.66	10476.27	2970.06
	95% percentile of flood inundation area (m^2)	180	425	80	0
	5% percentile of flood inundation area (m^2)	45800	36195	35100	16960
Artificial stage dataset 3	Mean flood inundation area (m^2)	11451.69	9734.60	8447.46	1909.04
	95% percentile of flood inundation area (m^2)	0	0	0	0
	5% percentile of flood inundation area (m^2)	42345	34760	33440	13700

Table 4.4 summarises the statistics of flood inundation model results from four stage datasets separately using the unfiltered 5 m LiDAR DEM, both SAR DEMs and the 10 m OS DEM as input topography.

Unless the statistics are zero, the unfiltered 5 m LiDAR DEM predicted largest values in mean flood inundation area, the 95% percentile of flood inundation area and the 5% percentile flood inundation area followed by the 5 m SAR DEM, the 10 m SAR DEM and the 10 m OS DEM in all flooding events. The only exception was that the 5 m SAR DEM predicted a 265 m^2 larger 95% percentile of inundation area based on the artificial stage dataset 2. From the original stage data and the artificial stage dataset 3, all DEMs responded slowly and were unable to simulate any inundation at early stages, as all values of the 95% percentile of inundation area are zero for these two flood events. Artificial stage datasets 1 and 2, as with higher stage values, encouraged flooding to occur much sooner and all DEMs, excluding the 10 m OS DEM, predicted hundreds of square metres of the 95% percentile of inundation area.

Great differences exist among difference sources of DEMs and these differences were much greater than those due to the resolution effects. For example, the 5 m LiDAR DEM had a c. 2874 m^2 mean flood inundation area for the whole 5 hour simulation period, which is almost doubled compared to the c. 1793 m^2 and 1121 m^2 from the 5 m SAR DEM and the 10 m SAR DEM, not mentioning the non-inundation from the 10 m OS DEM. This is also found in the artificial stage datasets.

4.4.2.2. Filter Algorithm and Manning's n Effect

The filtered and unfiltered 5 m LiDAR DEMs were used as input topographic data in the model. The effect of Manning's n was tested and the value was set to be 0.12 (twice the default value), 0.6 (ten times the default value) and 6 (a hundred times the default value). Their results based on all stage datasets were compared with the results from the unfiltered DEM and filtered DEM both using the default Manning's n as 0.06. The comparison aims to assess the impact of filtering algorithm using in the TerraScan module in the MicroStation® package and the Manning's n in the flood inundation area.

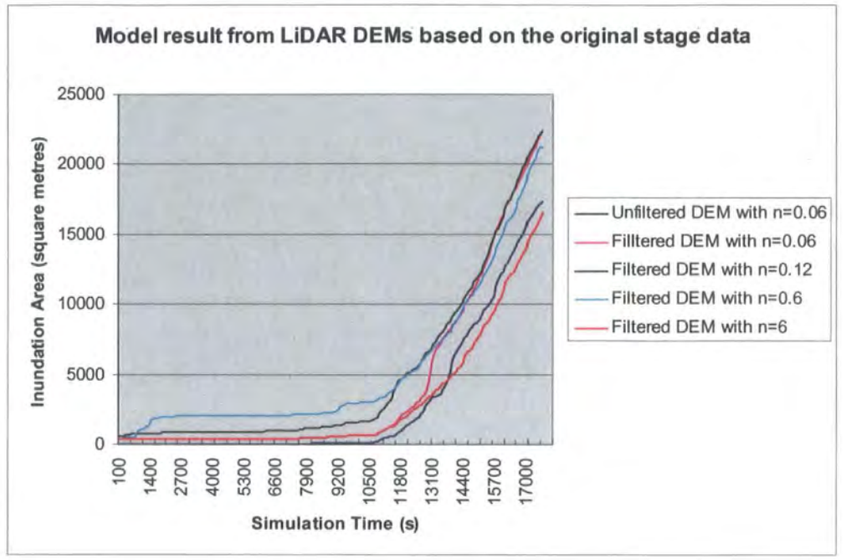

(a) Result from the original stage data

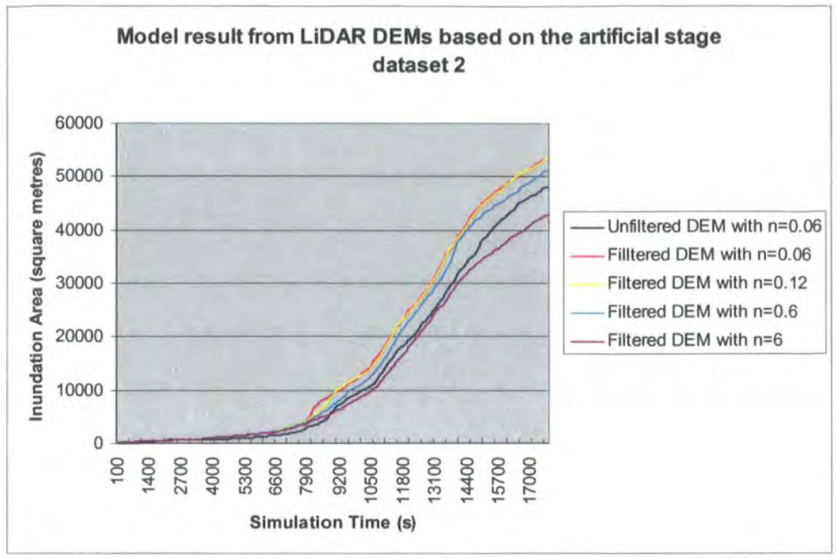

(c) Result from the artificial stage dataset 2

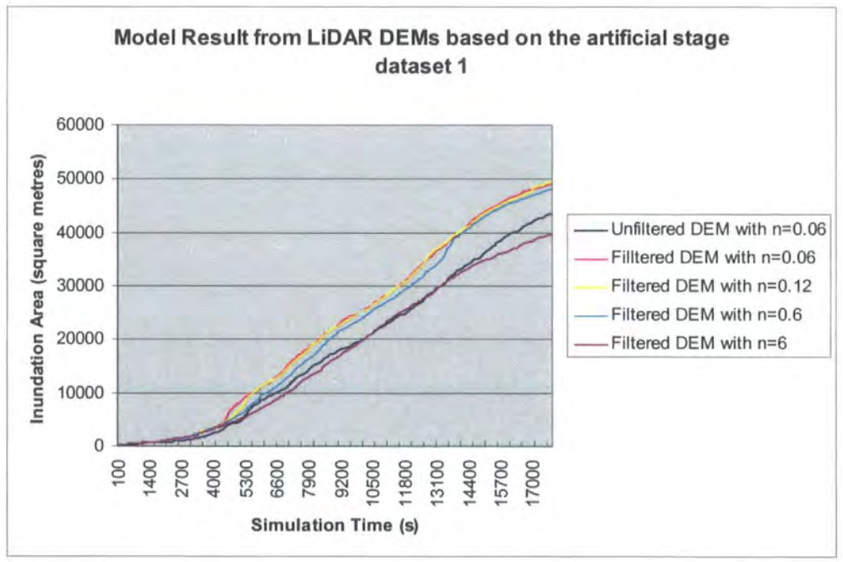

(b) Result from the artificial stage dataset 1

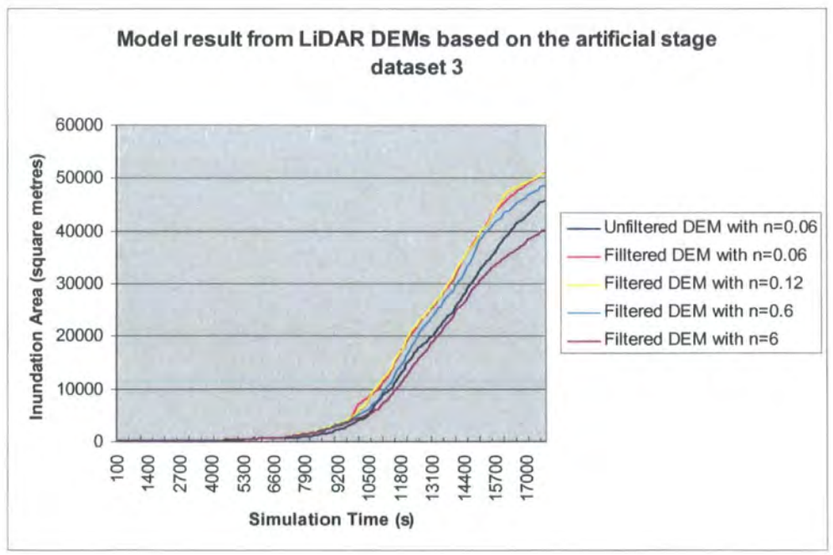

(d) Result from the artificial stage dataset 3

Figure 4.8 Differences in flood inundation area simulation from both LiDAR DEMs

Fig. 4.8 shows the differences in model response in terms of flood inundation area prediction from both unfiltered and filtered LiDAR DEMs based on all stage datasets. Four sets of Manning's n were used for the filtered 5 m LiDAR DEM (n = 0.06, n = 0.12, n = 0.6 and n = 6). The simulation of the unfiltered DEM used n = 0.06 only.

In all cases, the results show similar patterns of increase in inundation area accumulation. When using the default Manning's n of 0.06, the unfiltered LiDAR DEM predicted smaller inundation areas and this difference accumulated through simulation time. With increase in Manning's n, this difference decreased until using an n of 6. That is to say, the unfiltered LiDAR DEM with a Manning's n of 0.06 simulated an equivalent magnitude flooding to the filtered LiDAR DEM with Manning's n of 6. In addition, the increase in Manning's n from 0.06 to 0.12 and then to 0.6 made little difference in inundation area in all flood events.

4.4.2.3. Inundation Visualisation

Figure 4.9 Inundation visualisation from the unfiltered 5 m LiDAR DEM based on the artificial stage dataset 1

Figure 4.10 Inundation visualisation from the filtered 5 m LiDAR DEM based on the artificial stage dataset 1

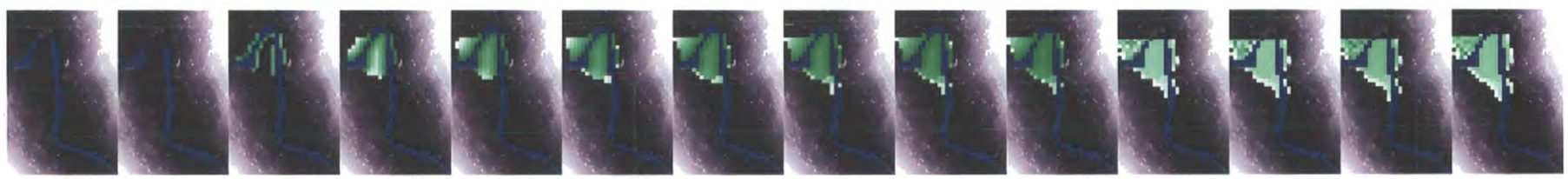

Figure 4.11 Inundation visualisation from the 10 m OS DEM based on the artificial stage dataset 1

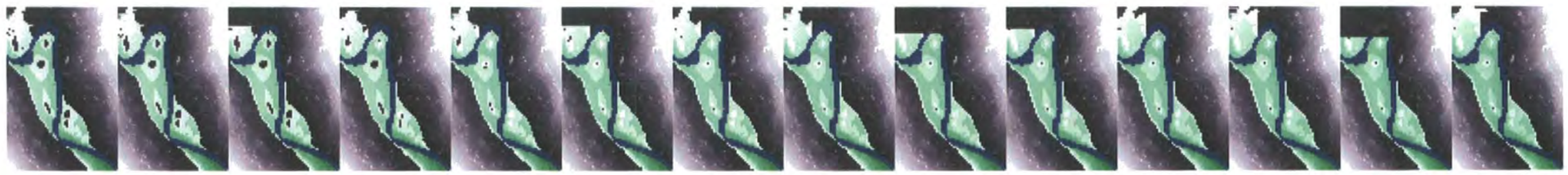

Figure 4.12 Inundation visualisation from the 5 m SAR DEM based on the artificial stage dataset 1

Figure 4.13 Inundation visualisation from the 10 m SAR DEM based on the artificial stage dataset 1

Fig. 4.9, 4.10, 4.11, 4.12 and 4.13 show inundation visualisation images from the unfiltered 5 m LiDAR DEM, filtered LiDAR DEM, 10 m OS DEM, 5 m SAR DEM and the 10 m SAR DEM respectively in artificial flood event 1 using the model (Yu and Lane, 2006a) every 5 minutes during the last 70 minutes of the simulation. The unfiltered 5 m LiDAR DEM was transform to a JPEG file and set as the background of each image. The blue polygon represents the normal river channel area. The green area represents the inundation area with the darker green as the deeper inundation depth.

The visualisations from both LiDAR DEMs show similar pattern of inundation. The unfiltered LiDAR DEM simulated a number of squares, which were not inundated through the whole simulation. This is not surprising as a number of trees were not removed in the unfiltered LiDAR DEM and their heights were added to the DEM. The simulated flooding, based on the artificial stage dataset 1, was unable to inundate areas above these elevations. In addition, both SAR DEMs show similar patterns of inundation and very little difference could be noticed from their visualisations in the artificial flooding event 1. In contrast, the 10 m OS DEM simulated very different patterns of inundation area. Inundation started on the upper reach and no inundation could be found on the relatively lower reach in this model test area. While all other DEMs predicted inundation areas from the lower part of the reach.

4.4.3. Model Validation

The maximum flood inundation area was identified on the NERC 1:15 000 digital aerial photographs taken 4 days after flooding on 23rd June 2005 as the validation data. Since only the original gauging stage represented the reality, the maximum inundation areas in the 'real' flooding event were compared with the validation data. To simulate a larger inundation area, model was operated to simulate a 10 hour flooding from all DEMs. Since the result showed that the model was unable to simulate the flooding event at the real magnitude as it was shown on the aerial photographs with the available stage data, no further accuracy assessment were conducted.

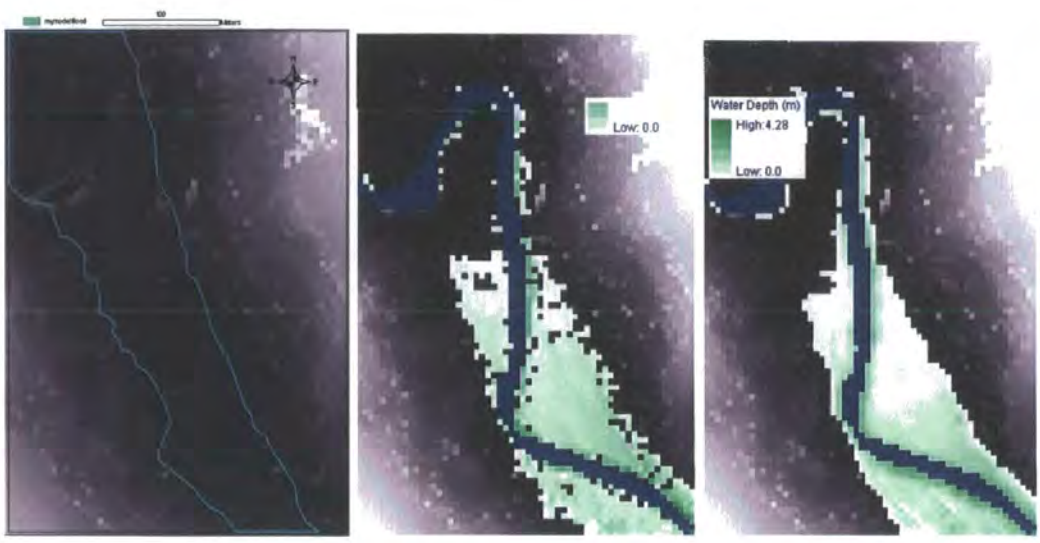

(a) Validation inundation area (b) Unfiltered 5 m LiDAR DEM (c) Filtered 5 m LiDAR DEM

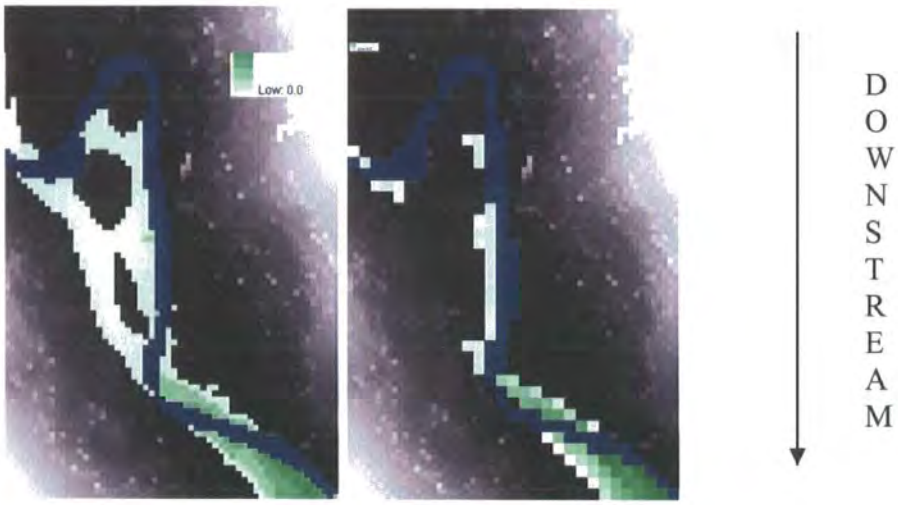

(d) 5 m SAR DEM **(e) 10 m SAR DEM**

Figure 4.14 Maximum inundation area derived from the NERC digital photographs and visualisations of model simulation for 10 hours using the original gauging station stage data with the unfiltered 5 m LiDAR DEM as the background

Fig. 4.14 compares the visualisations of maximum inundation area predicted by the model using the gauging station data in a 10-hour simulation with the manually derived inundation area from the post-event digital photographs. In this 'real' flooding event, the 10 m OS DEM was unable to predict any inundation area in five hours and hence its visualisation was not shown above. Visualisations from both LiDAR DEMs are more similar to the manually identified results shown in plot (a)

and both SAR DEMs predicted much smaller inundation areas than in the LiDAR DEMs. The result suggests that the stage still increased to cause a larger inundation area after the station was destroyed.

Table 4.5 Maximum inundation area summary from the NERC aerial photographs and the model simulations

Inundation area source	NERC APs	Unfiltered 5 m LiDAR DEM	Filtered 5 m LiDAR DEM	5 m SAR DEM	10 m SAR DEM
Maximum inundation area (m^2)	41650	18800	23550	13075	10000
Agreement with the validation data	N/A	45.1%	56.5%	31.4%	24.0%

Table 4.5 summarises the maximum inundation area identified from the NERC aerial photographs and the model results from both LiDAR DEMs and both SAR DEMs based on the original stage data.

4.5. Summary and Conclusions

A raster-based 2D diffusion-wave flood inundation model (Yu and Lane, 2006a) was used to investigate the impact of different DEM data sources of DEMs through a simulation for 5 hours in a c. 3.5 km^2 floodplain area around the gauge station of Broadway Foot. This was based on the original station stage data and three artificial stage datasets. Three kinds of DEM source were employed in this study as LiDAR data, SAR imagery and OS contour maps. A filter algorithm was also used to deal with trees in the raw LiDAR DEM. DEMs and stage data were set to be two parameters for this model separately and therefore this study was able to investigate more efficiently the topography and stage impact on flood inundation prediction through this particular model. For validation of the numerical models, comparisons were conducted. A 2D diffusion-wave inundation model based on InSAR imagery

was compared with a manual identification of maximum flood inundation extent on NERC digital aerial photographs of the River Rye taken four days after flooding.

Comparing both results from SAR DEMs in the artificial flooding events 2 and 3, the differences shrink when magnitude increased from the event 3 to event 2 and this indicates that the impact from DEM resolution may reduce in a larger magnitude flooding. This indication is not surprising. With the increase in stage, the whole water mass in the model test area increased. Therefore, inertia affected a larger proportion and hence reduced the effects from friction and gravity. The latter is directly determined by the DEMs representation of topographic at different resolutions in this case. Inertial effects are not represented in the model which is a weak part of the study.

Yu and Lane (2006a) noted that, it is only possible to simulate the peak inundation extent correctly through the precise timing of inundation if the floodplain is not laterally defined. Therefore, it is important to choose a suitable Manning's n for calibration of timing. In this study, since the impact of terrain model filtering on flood inundation prediction through topography is overwhelmingly larger than the effect of changing the value of Manning's n, the filtered 5 m LiDAR DEM was more likely to correspond to reality in terms of flood inundation. Note that the maximum flood inundation is highly sensitive to mesh resolution (Yu and Lane, 2006a).

It is important to be aware that the location of the river was extracted from the vector format Ordnance. Survey MasterMap™ and then transformed to 5 m or 10 m size grid raster. Uncertainty lies in river size and location and hence boundary conditions changed in each DEM. The effect of the uncertainty on the model response needs to be investigated in further research.

Amongst the unfiltered 5 m LiDAR DEM, both InSAR DEMs and the 10 m OS DEM, each DEM showed a single pattern of increase in inundation area and this pattern kept similar in all flooding events. Higher stage data was associated with a larger amount of inundation in a shorter time. The 5 m LiDAR DEM and the 10 m OS DEM simulated the largest and the smallest inundation area respectively in all cases with little difference seen between the results of from the InSAR DEMs.

The comparison of the filtered LiDAR DEM and unfiltered LiDAR DEM showed that the flood inundation model predicted larger and more rapid increase in inundation area using the filtered DEM since the filtered LiDAR DEM greatly removed the vegetation e.g. trees in the model test area and hence smoothed the floodplain and lowered the elevation values on the floodplain. Compared to the algorithm effect, the model was less sensitive to uniform increase of Manning's n, which indicates that a better representation of floodplain topography is more helpful to a model simulation than the calibration of uniform Manning's n on floodplains.

In relation to the validation of the models, the validation of the 2D diffusion-wave model showed that the filtered 5 m LiDAR DEM has the most potential to reconstruct a flash flood in rural areas, in terms of both inundation area amount and pattern. The agreement in pattern indicated that the filtered 5 m LiDAR DEM was able to set a more real boundary condition than other DEMs. On the other hand, the limited gauging stage data also emerged: development of a better inundation model or understanding of the inundation processes is required to limit the negative effect from the lack of gauging stage data.

5. Discussion, Summary and Conclusion

5.1. Discussion

DEMs available from various data sources and at a range of resolutions have been evaluated in this research. This research aimed to explore the quality of these DEMs, in relation to resolution and type in order to provide optimum representation of local topography for geomorphological and hydrological research. This has included evaluation of the algorithms used to derive topographic parameters and for interpretation purposes. Last but not least, the relationship between topographic representation and hydrological response was explored using flood inundation modelling.

5.1.1. DEM Quality Assessment

DEM quality, in terms of topographic representation, is of importance as more and more better-resolution DEMs become available for geomorphological and hydrological studies. DEM quality was assessed through derivation of topographic parameters, such as slope, aspect, curvatures, upslope contributing area and the Topographic Wetness Index (e.g. Quinn et al., 1991 and Jenson and Domingue, 1988). The need to do this for DEMs from different sources reflects the fact that most DEMs users ignore errors in DEMs or estimate their impacts using only information from the DEM provider (Wechsler and Kroll, 2006). Wechsler and Kroll (2006) utilised a Monte Carlo methodology and summary statistics to help evaluate DEM error on topographic attribute estimation using only one DEM. They found DEM errors have a large impact on slope especially, and seven uncertainty estimators showed that uncertainties cumulated in streams, upper streams in particular, where slope changes along a river channel. This finding is important for both geomorphological and hydrological applications where key processes take place. In this case, DEM errors can have different influences on different environmental applications, since different applications focus on different surface attributes. DEM errors should be routinely estimated and taken into account in relation to specific environmental applications. The sources and locations of errors need to be explored

in DEMs and can be used as a reference for applications which use DEMs as data input. In addition to the exploration, DEMs from different sources and at different resolutions can be selected for specific study purposes. Wechsler and Kroll (2006) considered only one DEM in their analysis while eight DEMs were assessed in this study and the results showed that different DEMs have different topographic attributes, particularly in the river channels. The finding suggests uncertainty varies between DEMs from different sources and with different resolutions. Coarser resolution DEMs tend to have larger errors in areas where slope changes rapidly.

5.1.2. Algorithms for Topographic Attribute Calculation

Little consistency regarding the most appropriate algorithm for topographic analysis is found in literature (Wechsler and Kroll, 2006). Zhou and Liu (2002) developed a quantitative methodology for objective and data-independent assessment of errors from five algorithms, including DEMON, D∞, FMFD, D8 and Rho8, in topographic parameters extraction from gridded DEMs. All these grid-based algorithms introduced errors in surface parameter calculations which were mainly due to the nature of the grid data structure and over-simplified assumptions in relation to flow routing. DEMON showed the best performance in error assessment of the five algorithms. Both D∞ and FMFD showed good results on saddle surfaces and poor results on convex and plane surfaces. The errors in the results from the other two algorithms were unacceptably large and it was suggested that hydrological modelling was highly affected by DEM error. In this study, the algorithm in Zeverbergen and Thorne (1987) provided the smallest standard deviations of all derivatives. The D8 method calculated similar maximum slopes from DEMs from the same data source but produced results sensitive to the data source. There were large differences in relation to the photogrammetrically-derived DEMs. In addition, the quadratic surface in Evans (1979), used by the ENVI package, calculated lower minimum, larger maximum values and larger standard deviations in profile curvature than the multi-flow algorithm in Zeverbergen and Thorne (1987) used by the SAGA package. These two algorithms calculated similar mean profile curvature values.

5.1.3. DEM Data Source

With the development of remote sensing techniques, DEMs have become available from a large range of sources. Overall, DEMs can be generated from conventional contour maps (the OS DEMs in this study), photogrammetrically derived from aerial photographs (the InfoTerra and NERC DEMs in this study), generated from InSAR imagery (the InSAR DEMs in this study) and produced from airborne LiDAR data.

5.1.3.1. Ordnance Survey DEMs

In this study, the 10 m and 50 m resolution Ordnance Survey DEMs were derived from 1:10 000 and 1:50 000 scale topographic contour maps and hence were greatly limited in quality by their scale as well as the artefacts that follow from digitising contours (McCullagh, 1998 in Lane et al., 1998). Large amounts of noise on the surface were introduced into the DEMs. Furthermore, contour lines caused large amounts of aliasing in DEMs especially at the coarser resolution and led to a discontinuous surface representation. Therefore, the contour map derived DEMs were inaccurate in terms of topographic representation particularly for geomorphological and hydrological studies.

5.1.3.2. Photogrammetrically Derived DEMs

Two DEMs generated from high resolution aerial photographs captured before and after the flash flood, respectively, provided DEMs at 3.0 m and 0.5 m. The difference in statistics indicated their potential capability for representing geomorphological changes due to flooding and landslides. However, both DEMs were generated photogrammetrically as TINs and became over sensitive to the topography in the whole study area due to the nature of the TIN and their high spatial resolution. Triangular irregular networks are constructed to represent detailed change in elevations on a surface and so a TIN would be over-sensitive to the elevation change in areas where only coarser details are needed. In addition, this issue could be due to the large amount of noise derived from stereo matching errors in photogrammetrically-derived DEMs. Therefore, both DEMs from aerial photographs

were not suitable for this study though they needed less storage space than InSAR DEMs and OS DEMs.

5.1.3.3. InSAR DEMs

The airborne InSAR (or IFSAR) DEM is collected rapidly and is available for much of the UK (e.g. Bates and De Roo, 2000; Cobby et al., 2003; Mason et al., 2003; Horritt et al., 2003; Bradbrook et al., 2004). InSAR DEMs tended to have the smallest variation in elevation compared to DEMs at the same resolution from the other sources.

NEXTMap is the only commercial producer of InSAR DEMs in the UK. Therefore, geomorphologists and hydrologists would not normally be able to generate InSAR DEMs by themselves. After the DEMs are published, it is difficult to investigate the DEM generation processes and methods and hence their impact on DEM quality. Phase wrapping has been taken as the most important part in InSAR DEM generation and no single algorithm is thought to be sufficient (Singh et al., 2005). Compared to the hybrid approach used in Singh et al. (2005), the InSAR DEMs derived from NEXTMap, UK were based on only a single algorithm (Mercer, 2004). DEM quality may be improved when a more robust algorithm is developed and utilised. The focus of this thesis was to compare the accuracy of both InSAR DEM and LiDAR DEM at various resolutions in areas with large slope variations, such as ridges and in valleys for geomorphological research, e.g. landslide assessments.

5.1.3.4. LiDAR DEMs

LiDAR has become increasingly available for hydrological modelling research in the UK (i.e. Marks and Bates, 2000; Bates et al., 2003; Cobby et al., 2003; Mason et al., 2003; Yu and Lane, 2006a and 2006b). LiDAR data have the advantages: (1), the LiDAR data consist of digital format of measurements which are easy to process; and (2) direct measurements are more independent of horizontal errors (Marks and Bates, 2000). The 5 m LiDAR DEM in this study was able to provide more detailed topographic information than DEMs from other sources in terms of detection of fine

features and shows different topographic attributes and statistics (frequency distribution and cumulative probability).

In this study, the comparison of the 5 m InSAR DEM and the LiDAR data showed a range of 2 m to 5 m differences in valleys (Fig. 3.39). This finding indicates that topographic representations are more likely to be different in areas with large slope changes for DEMs from these two sources.

The NEXTMap InSAR DEM was provided at 5 metre and ±0.5-1.0 m RMSE vertically. The LiDAR technique provided DEMs at 0.5-2 m resolution with ±0.15-0.30 m RMSE in elevation. Therefore, increasingly LiDAR data provide for much finer resolution DEMs with better accuracy and precision than the InSAR DEMs. However, regarding the high cost of LiDAR, Mercer (2004) stated that compared to the 30-100 metre spacing and ±5-50 m RMSE vertically from space-borne coverage, airborne LiDAR technique and airborne photogrammetry with high accuracy but low sample spacing, the airborne InSAR can be seen as an intermediate product. However, it also has issues.

First, a fully-designed over-flight is needed for different environmental applications. Lim et al. (2003) listed more detailed characteristics of scanning systems than Table 2.3 including wavelength, pulse repetition rate, pulse energy, pulse width, beam divergence, scan angle, scan rate, scan pattern, GPS frequency, INS frequency, operation altitude, footprint, multiple elevation capture, post spacing, horizontal and vertical accuracies, post-processing software etc. They noted that footprint size and post spacing will be more adaptable by adjusting other scan parameters such as pulse rate and pulse resolution for forest research. Similarly, it is also important to design an over-flight for LiDAR operation, in terms of measurements density, footprint size etc., for specific types of surface topography for hydrological modelling and geomorphological studies. For example, in this study, the available LiDAR raw data did not cover the whole study area and contained three large data gaps in the Head House study area. While altitude of operation is directly related to the number of flight lines required. More flight lines will increase data collection cost. Goodwin et al. (2006) compared three platform altitudes for a forest application and found that an increase from 1000 m to 3000 m had few impacts on accuracy. Whether such data

remain suitable for geomorphological or hydrological research is therefore needs to be considered as whilst the accuracy may be retained, the resolution may not and resolution is crucial topographic representation. Overall, LiDAR data collection should be more focused on and its design should be oriented to specific application, if possible for the budget, to utilise the high potential of LiDAR data at its best.

Second, LiDAR data post processing needs more attention. LiDAR data are assumed to be the optimum DEM in this study due to its specific collection principals. In this case, 4 to 6 million measurements were taken over an area of c. 9 km^2. For both geomorphological and hydrological research in this study, not all of the information is useful, such as where there are trees. Different features on the surface should be treated in different ways. For example, vegetation heights and artificial elements such as buildings need to be removed from the DEM for investigation of surface elevation change for landslide assessment and this has led to a need for measurement categorisation. Shan and Sampath (2005) developed and tested a labelling algorithm for separation of ground points and none-ground points in raw LiDAR data in four suburban areas of the USA, Japan and Canada. The results were assessed that and showed that 2.7% ground points and 2.6% building points were wrongly labelled in all study areas overall. While large mounts of points may be involved, this case may not necessary indicate a fine categorising algorithm for the LiDAR data in small study area. Treatments are different in hydrological applications, inundation propagation on floodplains in particular. Structural elements such as buildings on floodplains cannot be removed due to their effect on momentum and mass conservation (Yu and Lane, 2006b). In addition, the vegetation heights need to be treated more efficiently for flood inundation modelling. Mason et al. (2003) used vegetation heights derived from airborne laser scanning altimetry to set different flow resistance equations for different model areas such as channel sediment, short vegetation, and tall and intermediate vegetation, for a 2-D hydraulic model simulating a flood event on the River Severn, UK in October 1998. The simulation result was tested with an InSAR image captured during the flooding and extremely high agreements were found between the flood inundation extent prediction and the validation data. Therefore, LiDAR raw data need to be treated carefully with respect to purpose of the study, such as by using a more sophisticated algorithm for categorising ground and none-ground measurements even in rural areas.

5.1.4. DEM Resolution

Due to the increasing availability of high-resolution DEMs, DEM resolution has been a focus in recent decades in geomorphological and hydrological studies (e.g. Zhang and Montgomery, 1994; Wolock and Price, 1994; Butler et al., 1998; Walker and Willgoose, 1999; Westaway et al., 2000; Lane et al., 2003; Yu and Lane, 2006a.).

Recent studies have shown that InSAR DEMs were not suitable for landslide studies. Singh et al. (2005) compared a space-borne InSAR DEM with the conventional Swisstopo DEM for the accuracy assessment of InSAR derived input maps for landslide susceptibility in the Swiss Alps and found that the InSAR DEM introduced significant errors in absolute height and slope angles especially along ridges and in valleys. In addition, their visual comparison of stereo images and the DEM showed many topographic details were lost during InSAR DEM generation. This result is consistent with the comparison in Mercer (2004), which showed that the InSAR data showed approximately 30% larger RMSE in urban-areas than in non-urban areas at validation. It is more likely that more areas with large slope changes exist in urban areas, e.g. buildings. However, only 25 m resolution InSAR DEMs were tested in Singh et al. (2005). The highest resolution InSAR DEM in the UK is 5 m, which is much finer than the 25 m one derived from space-borne imagery. In this study, Fig. 3.17 shows that large differences in topographic attributes exist in valleys from the comparison of the 5 m InSAR DEM and the 10 m InSAR DEM. Meanwhile, no significant difference can be found in comparisons with other DEMs. This finding may suggest that the 5 m InSAR DEM in this study greatly improves the representation in areas where slopes change rapidly. Thus, much of Singh et al. (2005) conclusions may be due to the fact that their DEM was of coarse resolution rather than poor precision and accuracy.

5.1.5. Flood Modelling

Apart from data quality aspects, hydrological studies using numerical modelling (flood inundation modelling in this case) have seen major improvements resulting from increasing availability of high-quality topographic data, computational

efficiency and validation approaches. Due to the simplifying assumptions of flow in the river channel and on the floodplain, 2D models have become available for solving the shallow-water equations using available field data instead of the traditional 1D models (Marks and Bates, 2000). In addition to this development, several methodological concerns have arisen. For example, Bradbrook et al. (2004) used a percentage of wetness for each cell on floodplains to decide the dry-wet conditions and processes on floodplains. Yu and Lane (2006b) emphasised the importance of structural elements on floodplains and concluded explicit topographic representation gave better results than adjusting Manning's n on the floodplain. Yu and Lane (2006a) tested the effects of mesh resolution of the input topographic data and confirmed that coarser resolution led a poorer ability in controlling inundation processes. Horritt et al. (2006) examined the effects of mesh resolution and topographic data quality using a 2D finite volume model of channel flow. A better representation of small elements as hydraulic features and an accurate representation of the test zone boundary caused sensitivity due to mesh resolution in all flood events simulated at a similar magnitude. In addition to that finding, a large magnitude flood event would increase all errors regarding the sensitivities to mesh resolution and topographic representation. In terms of validation data, Bates et al. (2006) for the first time validated the dynamic performance of a simple 2D flood inundation model, LISFLOOD-FP and found better description of floodplain hydrological processes for a more accurate representation of dewatering of the floodplain. In this study, a 2D diffusion-wave inundation model with a depth-averaged treatment in the river channel was used and the model represented more efficiently the effects of floodplain topography and wetting-drying processes. High-quality topographic data, varying in resolution and data source, were compared in different magnitude flooding events. The largest agreement in terms of flood inundation area and pattern was shown in the simulated flood event using the filtered 5 m LiDAR for floodplain topographic representation. Higher magnitude flood events predicted larger inundation area and larger agreements among results from different DEMs in terms of inundation area. However, due to the incompleteness of gauging station data, the model was unable to simulate the actual flood events in a short reach (c. 2 km). The only available validation data came from the aerial photographs taken after the flood event. This suggested that a better boundary condition modelling methodology is needed in such poorly gauged areas.

5.1.6. Other Issues

The whole study contained over 40 GB data in thousands of files including all the raw data and production of processes and analysis. In addition to this large volume of data, most manipulations have to be started manually. Therefore, a good data management approach is needed to reduce processing time and to ensure the accuracy of procedure during the whole study. In terms of software used in this study, SAGA, developed by University of Goettingen, Germany was found to be a powerful software package in this study. The features of open source; small demands in terms of occupation space; and in customarised development make it competitive for small budget and relatively simple projects.

5.2. Summary and Conclusions

5.2.1. Summary

This study aimed to verify high-quality topographic data varying in both source and resolution for flood impact assessment in relation to: 1) DEM analysis and 2) numerical flood inundation modelling. The work showed that when choosing an optimum DEM for topographic information interpretation, it is helpful to have a good understanding of local topography and the nature of the environmental application. The optimum DEM in this study means the one that has the most detailed and useful topographic information with respect to the needs of the hydrological model. Data source, DEM resolution and topographic parameters derivation algorithms were all thought to control topographic representation and hence these three factors were compared and contrasted.

Chapter Two summarised the datasets available for this study. The Head House and a flood model test areas were clipped out from the whole study area. The Head House area and the whole study area were chosen for DEM assessment. The flood model test area was used with the flood inundation models. The datasets used included topographic data, imagery and field data. The topographic data varied in source and resolution. It included the Ordnance Survey topographic maps at three different scales (1: 10 000, 1:25 000 and 1:50 000), the Ordnance Survey

MasterMap™ in shape file format, the Ordnance Survey DEMs at 10 m and 50 m spatial resolution and derived from 1:10 000 and 1:50 000 contour maps of the whole study area, 5 m, 10 m and 50 m resolution SAR DEMs of the whole study area, two photogrammetrically-derived DEMs at 0.5 m and 3 m resolution from post-event and pre-event aerial photographs of the Head House area and one 5 m resolution DEM generated from LiDAR data of part of the River Rye catchment. The imagery included the ATM image from NERC on 26th August 2005, digital aerial photographs and metric 1:6 000 and 1:15 000 aerial photographs taken by NERC on 23rd June 2005 and 26th August 2005, respectively and pre-event aerial photographs taken on 31st July 2001 and supplied by InfoTerra. The field data included GCPs, transects, GPS rover and ground-based Laser scanning etc. Other data included stage data at the Broadway Foot Station on River Rye and the flood extent prediction from the model of the Environment Agency.

Large amounts of topographic data were implemented in the DEM assessment as presented in Chapter Three. Eight DEMs from four different sources (the OS data, InSAR imagery, aerial photographs and LiDAR data) and at five different resolutions (0.5 m, 3 m, 5 m, 10 m and 50 m) were acquired/generated and processed by three algorithms (the D8 method and those described in Zeverbergen and Thorne (1987) and Evans (1979)) using three available commercial or scientific software packages (the ENVI, Arc/GIS and SAGA) for calculation and statistical analysis for four key surface parameters (slope, aspect, profile curvature and the Topographic Wetness Index).

In relation to numerical flood inundation modelling as represented in Chapter Four, two objectives were achieved by 1) assessment of the relationship between model response of a flood in terms of inundation area and Manning's n in different flooding events simulated and 2) comparison of a numerical flood inundation model from the Environment Agency with a manual approach of identification of maximum inundation extent on high resolution post-event aerial photographs.

5.2.2. Core Conclusions

The research showed that topographic parameters/attributes are sensitive to the resolution and source of the input topographic data (DEMs in this case) and kernel size in processing. Predicted hydrological response in terms of flood inundation area was highly sensitive to the resolution and the source of topographic data as inputs. The core conclusion are summarised as follows:

1) Coarser resolution DEMs generalised surface topographic characteristics especially when moving from a 10 m grid to a 50 m grid DEM, but with less degradation in topographic information representation when moving from a 5 m grid InSAR DEM to a 10 m resolution InSAR DEM. Finer resolution and smaller filter size have the same type of impact on slope and aspect calculations. For example, finer-resolution DEMs contain smaller minimum, mean and standard deviation values in elevation. They calculated smaller minimum and maximum slope and aspect values and larger mean and standard deviations in slope and aspect. However, aspect differences were smaller than those in slopes due to the resolution and filter size effects. In addition, DEMs at finer resolutions have smaller minimum profile curvatures and larger maximum values and standard deviations in profile curvature. One exception should be noticed is that grid size changes from 5 m to 10 m did not match the trend. As a statistic of a second order topographic parameter, the mean profile curvature is less sensitive to the resolution and filter size than the slope and aspect statistics. The Topographic Wetness Index is more sensitive to the resolution and finer DEMs calculate smaller minimum and mean TWI and larger maximum TWI and standard deviations. For different scales of study area, cumulative frequency trends of surface attributes may change and the trend tended to shift to the DEM at a larger scale.

2) In terms of data sources, the LiDAR DEM has the best representation of the topography in this study. The 5 m and 10 m InSAR DEMs and the 5 m LiDAR DEM show more details in local topography and its change. The LiDAR DEM takes advantage of the principle of LiDAR measurements and provides better terrain representation in areas with trees when using an

appropriate filtering algorithm, which is important for the flood inundation modelling in rural areas. The fact that the 5 m LiDAR DEM provided better results than the 5 m InSAR DEM confirms that data sources are important and not just resolution.

3) Different DEMs represent topography differently and lead to different pattern in flood inundation propagation on the floodplain. The 5 m LiDAR DEM simulated the largest flood and with the best agreement with the validation data on aerial photographs. A larger magnitude flood led to a quicker hydrological response and a larger inundation area prediction. Compared to the uniform Manning's n calibration, a better representation of floodplain topography gives more efficient for a better simulation of flooding. In addition, the EA numerical flood inundation model based on InSAR imagery has the potential to provide highly accurate (a larger than 95% in confidence) flood inundation area prediction in this scale of floodplain.

References

1. Barling, R. D. (1992). *Saturation Zones and Ephemeral Gullies on Arable Land in Southeastern Australia*. Ph.D. Thesis, University of Melbourne.
2. Bates, P. D. (2004). Remote sensing and flood inundation modelling. *Hydrological Processes*, **18**:2593-2597.
3. Bates, P. D. and De Roo, A. P. J. (2000). A simple raster-based model for flood inundation simulation. *Journal of Hydrology*, **236**:54-57.
4. Bates, P. D. and Lane, S. (1998). Preface: High resolution flow modelling in hydrology and geomorphology. *Hydrological Processes*, **12**:1129-1130.
5. Bates, P. D., Anderson, M. G., and Hervouet, J. M. (1995). Initial comparison of two two-dimensional finite element codes for river flood simulation. Proceedings of the Institution of Civil Engineers, *Water Maritime and Energy* **112**, 238–248.
6. Bates, P. D., Anderson, M. G., Baird, L., Walling, D. E., and Simm, D. (1992). Modelling floodplain flow with a two-dimensional finite element scheme. *Earth Surface Processes and Landforms* **17**, 575–588.
7. Bates, P. D., Marks, K. J. and Horritt, M. S. (2003). Optimal use of high-resolution topographic data in flood inundation models. *Hydrological Processes* **17**, 537-557.
8. Bates, P. D., Wilson, M. D., Horritt, M. S., Mason, D. C., Holden, N., and Currie, A. (2006). Reach scale floodplain inundation dynamics observed using airborne synthetic aperture radar imagery: Data analysis and modelling. *Journal of Hydrology* **328**: 306-318.
9. Beven K. J. (2000). Rainfall-Runoff Modelling: The Primer, John Wiley & Sons.
10. Beven K. J. and Kirkby M. J. (1979). A physically based, variable contributing area model of basin hydrology. *Hydrological Science Bulletin* **24**(1): 43-69.
11. Bradbrook, K. F., Lane, S. N., Waller, S. G., and Bates, P. D. (2004). Two dimensional diffusion wave modelling of flood inundation using a simplified

channel representation. *International Journal of River Basin Management* **3**:1-13.

12. Burt, T. P. and Butcher, T. P. (1986). Development of topographic indices for use in semi-distributed hillslope runoff models. *Z. Geomorphological Supp.*, **NF 58**, 1-19.
13. Butler J. B., Lane S. N., Chandler J. H. and Porfiri E. (2002). Through-water Close Range Digital Photogrammetry in Flume and Field Environments. *Photogrammetric Record* **17**(99).
14. Butler, J. B., Lane, S. N., and Chandler, J. H. (1998). Assessment of DEM Quality for Characterizing Surface Roughness Using Close Range Digital Photogrammetry. *Photogrammetric Record* **16** (92).
15. Cobby, D. M, Mason, D. C., Horritt, M. S. and Bates, P. D. (2003). Two-dimensional hydraulic flood modelling using a finite-element mesh decomposed according to vegetation and topographic features derived from airborne scanning laser altimetry. *Hydrological Processes* **17**, 1979-2000.
16. Courant, R., Friedrichs, K., and Lewy, H. (1928). Über die partiellen Differenzengleichungen der mathematischen Physik. *Mathematische Annalen*, vol. 100, No. 1, pages 32–74.
17. Ervine, D.A., Willets, B.B., Sellin, R.H.J., and Lorena, M. (1993). Factors affecting conveyance in meandering compound flows. *Journal of Hydraulic Engineering American Society of Civil Engineers* **119**, 1383–1399.
18. Evans, I. S. (1979). An integrated system of terrain analysis and slope mapping. Final report on grant DA-ERO-591-73-G0040, University of Durham, England.
19. Evans, I. S. (1981). General Geomorphometry, In *Geomorphological Techniques*, edited by A. Goudie (New York: Allen & Unwin), pp 31-37.
20. Fread, D. L. (1984). In: Anderson, M. G., Burt, T. P. (Eds.). Hydrological Forecasting, Wiley, Chichester (chap. 14).
21. Fread, D. L. (1993). In: Maidment, D. R. (Ed.). Handbook of Applied Hydrology, McGraw-Hill, New York (Chapter 10).
22. Goodwin, N. R., Coops, N. C. and Culvenor, D. S. (2006). Assessment of forest structure with airborne LiDAR and the effects of platform altitude. *Remote Sensing of Environment* **103**, 140-152.

23. Hardy, R. J., Bates, P. D., and Anderson, M. G. (1999). The importance of spatial resolution in hydraulic models for floodplain environments. *Journal of Hydrology* **216**:124-136.

24. Heerdegen, R. G. and Beran, M. A. (1982) Quantifying source areas through land surface curvature and shape. *Journal of Hydrology* **57**,359-373.

25. Hicks D. M., Duncan M. J., Walsh J. M., Westway R. M. and Lane S. N. (2001). The Braided Waimakariri River: New Views of Form and Process from High-density Topographic Surveys and Time-lapse Imagery, In Gravel Bed Rivers 2000 CD ROM, edited by T. Nolan and C. Throne, Special Publication (Christchurch: New Zealand Hydrological Society).

26. Horritt, M. S. and Bates, P. D. (2001). Predicting floodplain inundation: raster-based modelling versus the finite-element approach. *Hydrological Processes* **15** (5): 825-842.

27. Horritt, M. S., Bates, P. D. and Mattinson, M. J. (2006). Effects of mesh resolution and topographic representation in 2D finite volume models of shallow water fluvial flow. *Journal of Hydrology* **329**, 306-314.

28. Horritt, M. S., Mason, D. C., Cobby, D. M., Davenport, I. J., and Bates, P. D. (2003). Waterline mapping in flooded vegetation from airborne SAR imagery. *Remote Sensing of Environment* **85**: 271-281.

29. Jenson, S. K. (1991). Applications of hydrologic information automatically extracted from digital elevation models, *Hydrological Processes* **5**, 31-44.

30. Jenson, S. K. and Domingue, J. O., (1988). Extracting Topographic Structure from Digital Elevation Data for Geographic Information System Analysis. *Photogrammetric Engineering and Remote Sensing* Vol.54, No.11, pp.1593-1600.

31. Johnson, R. M. and Warburton, J. (2002). Flooding and geomorphic impacts in a mountain torrent: Raise Beck, central lake district, England. *Earth Surface Processes and Landforms* **27** (9): 945-969.

32. Kimerling, A. J., and Moellering, H. (1989). The development of digital slope-aspect displays. In Proceedings of AutoCarto 9, Bartimore, MD, April 2-7, 1989. Little Falls, VA: American Society for Photogrammetry and Remote Sensing and American Congress on Surveying and Mapping, 241-244.

33. Kirkby, M. J., Imeson, A. C., Bergkamp, G., and Cammeraat, L. H. (1996). Scaling up processes and models from the field plot to the watershed and regional scales. *Journal of Soil and Water Conservation* **51**:391-396.

34. Lane, S. N. (1998). Hydraulic modelling in hydrology and geomorphology: A review of high resolution approaches. *Hydrological Processes*, **12**:1131-1150.

35. Lane, S. N. (2000). The Measurement of River Channel Morphology Using Digital Photogrammetry. *Photogrammetric Record* **16** (96).

36. Lane, S. N., C. J. Brooks, M. J. Kirkby and Holden, A. (2004). Network-index-based Version of TOPMODEL for Use with High-resolution Digital Topographic Data, Hydrological Processes 18, 191-201.

37. Lane, S. N., James, T. D., and Crowell, M. D. (2000). Application of Digital Photogrammetry to Complex Topography for Geomorphological Research. *Photogrammetric Record* **16** (95).

38. Lane, S. N., James. T. D., Pritchard, H., and Saunders, M. (2003). Photogrammetric and Laser Altimetric Reconstruction of Water Levels for Extreme Flood Event Analysis. *Photogrammetric Record* **18** (104).

39. Lane, S. N., Richards, K., and Chandler, J. (eds.) (1998). *Landform Monitoring, Modelling and Analysis*, Wiely.

40. Lim, K., Treitz, P., Wulder, M. St-Onge, B and Flood, M. (2003). *LiDAR remote sensing of forest structure. Progress in Physical Geography* **27**, 88-106.

41. Mark, D.M. (1984). Automated detection of drainage networks from digital elevation models. *Cartographica*, **21**, 168-178.

42. Marks, K. and Bates, P. (2000). Integration of high-resolution topographic data with floodplain flow models. *Hydrological Processes* **14**, 2109-2122.

43. Mason, D. C., Cobby, D. M., Horritt, M. S. and Bates, P. D. (2003. Floodplain friction parameterisation in two-dimensional river flood models using vegetation heights derived from airborne scanning laser altimetry. *Hydrological Processes* **17**: 1711-1732.

44. Mendicino G. and Sole A. (1997). The information content theory for the estimation of the topographic index distribution used in TOPMODEL. *Hydrological Processes* Vol.11, 1099-1114.

45. Mercer, B. (2004). DEMs created from airborne IFSAR-An update. Proceeding of the ISPRS XXth Congress, Istanbul, Turkey, July.

46. Moore, I. D., Burch, G. J., and MacKenzie, D. H. (1988). Topographic effects on the distribution of surface soil water and the location of ephemeral gullies. *Transactions of the American Society of Agricultural Engineers* **31**:1098-1107.

47. Moore, I. D., Grayson, R. B. and Ladson, A. R. (1991). Digital terrain modelling: a review of hydrological, geomorphological, and biological applications. *Hydrological Processes* **5**:3-30.

48. Moore, I. D., Lewis, A., and Gallant, J. C. (1993). Terrain attributes: estimation methods and scale effects. In A. J. Jakeman, M. B. Beck, and M. J. McAleer (eds.), *Modelling Change in Environmental Systems*. New York: Wiley, 189-214.

49. NCGIA ed. (1996). Proceedings of the Third International Conference on Integrating GIS and Environmental Modelling, Santa Fe, New Mexico, USA, 21-25 January.

50. O'Callaghan, J. F. and Mark, D. M. (1984). The extraction of drainage networks from digital elevation data. *Computer Vision, Graphics and Image Processing* **28**:323-344.

51. Ordnance Survey (2003) TerraScan user's guide.

52. Penning-Rowsell, E.C., Tunstall, S.M. (1996). *Risks and resources: defining and managing the floodplain*. In: Anderson, M.G., Walling, D.E., Bates, P.D. (Eds.). Floodplain Processes, Wiley, Chichester, pp. 493–533.

53. Planchon, O. and Darboux, F. (2002). A fast, simple and versatile algorithm to fill the depressions of digital elevation models, *Catena* **46**:159-176.

54. Quinn, P. F., Beven, K. J., and Lamb, R. (1995). The ln(a/tanβ) index: how to calculate it and how to use it within the TOPMODEL framework. *Hydrological Processes* **9**:161-182.

55. Quinn, P. F., Beven, K. J., Chevallier, P., and Planchon, O. (1991). The prediction of hillslope flowpaths for distributed modelling using digital terrain models. *Hydrological Processes* **5**:59-80..

56. Shan, J. and Sampath, A. (2005). Urban DEM generation from raw LiDAR data: A labelling algorithm and its performance. *Photogrammetric Engineering and Remote Sensing* **71**(2): 217-226.

57. Singh, L. P., van Westen, C. J., Ray, P. K. C., and Pasquali, P. (2005). Accuracy assessment of InSAR derived input maps for landslide susceptibility analysis: a case study from the Swiss Alps. *Landslides* **2**(3): 221-228.

58. Stein, A., Van Der Meer, F., and Gorte, B. (1999). Kluwer Academic Publishers, *Spatial Statistics for Remote Sensing.*

59. Stephenson, G. (1973) Mathematical Methods for Science Students, London: Longman.

60. United Nations, Department of Humanitarian Affairs (1997). Floods: people at risk, strategies for prevention, Geneva: United Nations.

61. Walker, J. P. and Willgoose, G. R. (1999). On the effect of digital elevation model accuracy on hydrology and geomorphology. *Water Resources Research* **35**: 2259-2268.

62. Walker, J. P. and Willgoose, G. R. (2006). A comparative study of Australian cartometric and photogrammetric Digital Elevation Model accuracy. *Photogrammetry Engineering and Remote Sensing* 72(7): 771-779.

63. Wang, Y. (1994). Strukturzuordnung zur automatischen Oberflächenrekonstruktion. Ph.D. dissertation, wissenschaftliche Arbeiten der Fachrichtung Vermessungswesen der Universität Hannover, No. 207.

64. Wechsler, S. P. and Kroll, C. N. (2006). Quantifying DEM uncertainty and its effect on topographic parameters. *Photogrammetric Engineering and Remote Sensing* **72**(9): 1081-1090.

65. Westway R. M., Lane S. N. and Hicks D. M. (2000). The Development of An Automated Correction Procedure for Digital Photogrammetry for the Study of Wide, Shallow Gravel-bed Rivers. *Earth Surface and Landforms* **25**: 209-226.

66. Westway R. M., Lane S. N. and Hicks D. M. (2003). Remote Survey of Large-scale Braided, Gravel-bed Rivers Using Digital Photogrammetry and Image Analysis. *International Journal of Remote Sensing* Vol. 24, No. 4, 795-815.

67. Wilson, J. P. and Gallant, J. C. ed. (2000). Terrain Analysis-principles and applications. John Wiley & Sons.

68. Wood, J. (1996). The Geomorphological Characterization of Digital Elevation Models, Ph. D. Thesis, University of Leicester, Department of Geography, Leicester, UK.

69. Yu, D. and Lane, S. N. (2006a). Urban fluvial flood modelling using a two-dimensional diffusion-wave treatment, part 1: mesh resolution effects, *Hydrological Processes* **20**, 1541-1565.

70. Yu, D. and Lane, S. N. (2006b). Urban fluvial flood modelling using a two-dimensional diffusion-wave treatment, part 2: development of a sub-grid-scale treatment. *Hydrological Processes* **20**, 1567-1583.

71. Zevenbergen, L. W. and Thorne, C. R. (1987). Quantitative analysis of land surface topography. *Earth Surface Processes and Landforms*, **12**, 47- 56.

72. Zhang W. and Montgomery D. R. (1994). Digital Elevation Model Grid Size, Landscape Representation and Hydrologic Simulation. *Water Resources Research* **30**: 1019-1028.